universität wien

MASTERARBEIT / MASTER'S THESIS

Titel der Masterarbeit / Title of the Master's Thesis

„Simulation of Supercoiled Ring Polymers under Shear Flow“

verfasst von / submitted by

Christoph Schneck, B.S.

angestrebter akademischer Grad / in partial fulfilment of the requirements for the degree of

Master of Science (MSc)

Wien, 2023 / Vienna, 2023

Studienkennzahl lt. Studienblatt / degree programme code as it appears on the student record sheet:	UA 066 876
Studienrichtung lt. Studienblatt / degree programme as it appears on the student record sheet:	Masterstudium Physics
Betreut von / Supervisor:	Univ.-Prof. Dipl.-Ing. Dr. Christos Likos
Mitbetreut von / Co-Supervisor:	Jan Smrek, PhD

Contents

1 Introduction **2**

2 Multi-Particle Collision Dynamics **6**
- 2.1 Coarse-Grained Hydrodynamic Interactions . . . 6
- 2.2 Dynamical Properties of the Solvent . . . 11
- 2.3 Non-Equilibrium MPCD Systems . . . 17
- 2.4 Coupling Embedded Objects to the MPCD Fluid . . . 19
- 2.5 Random MPCD without Hydrodynamic Interactions . . . 21

3 Fully Flexible Ring Polymers **22**
- 3.1 Bead Model of Polymer Chains . . . 22
- 3.2 Velocity Verlet Algorithm . . . 24
- 3.3 Ring Polymers in Dilute Solutions . . . 24
- 3.4 Ring Inflation under Shear Flow . . . 28

4 Supercoiled Ring Polymers **32**
- 4.1 Torsional and Bending Constraints . . . 32
- 4.2 Patches with and without Mass . . . 35
- 4.3 Rigid Body Dynamics . . . 36
- 4.4 Quaternion Formalism of 3D Rotations . . . 37
- 4.5 Stationary State Properties of Supercoiled Rings . . . 40

5 Supercoiled Ring Polymers under Shear Flow **47**

6 Conclusion **53**

Appendix **54**
- A Software and Hardware Details . . . 54
- B Calculation of Bending, Torsional, and Alignment Forces . . . 54
- C Abstract (English) . . . 56
- D Abstract (German) . . . 56

References **58**

1 Introduction

DNA is a polymer that carries the genetic information about the structure, function and reproduction of all living organisms. Naturally, it arises scientific curiosity and from the physical point of view, it is of particular interest to study which conformations DNA molecules take on and how they are affected by external stress, i.e., its mechanical properties. DNA is composed of two polymer chains that coil around each other and form the famous double-helix. The two strands twist around each other every 10.4 - 10.5 base pairs, a quantity that defines the equilibrium twist of DNA. This structure is not entirely rigid and can be deformed by mechanical strain, such as stretching, bending or twisting around the helical backbone. By tying the two ends of a DNA chain together the polymer's conformations are constrained to correspond to a certain equivalence class of knots, e.g., the unknot or the trefoil knot. Adding or subtracting twist to an open chain before closing the ring alters the shape of the resulting DNA string. The polymer will tend to increase its writhe and take on less open conformations which is referred to as supercoiling. This behaviour results from the combination of the confining ring topology and the competition of torsional and bending stiffness of the double-helix structure. [1, 2, 3]. The question arises what influence supercoiling exactly has on the conformations of circular polymers and and how these are impacts by external forces, e.g., their response to shear flow. Recent experiments have been able to directly study the effects of supercoiling on the shape of circular DNA molecules [2, 3] as well as their behaviour under shear flow [4].

The non-equilibrium properties of dilute complex fluids at room temperature, like single polymers suspended in a molecular solvent, result from an interplay of both the short-time thermal Brownian motion of the polymer and the long-time hydrodynamic behaviour of the solvent [5]. Typically, the solute is much larger than the particles of the surrounding fluid particles, e.g., a string of DNA compared to water molecules. The smaller solvent particles move much faster and are more numerous than the suspended objects. For instance, a colloid of diameter 1 μm displaces around 10^{10} water molecules [5]. The large length- and time-scale gaps in complex fluids complicate the theoretical calculation of the dynamics which requires the elaboration and merging of physics on completely different length- and time-scales. Another essential challenge is the large amount of fluid particles whose precise dynamics is governed by a microscopic description of the molecule and their mutual interaction. Clearly, a theoretical approach to complex fluids demands a coarse-graining over the fluid's degrees of freedom and reducing the system size accompanied by an effective description of the solvent-solvent as well as the solvent-monomer interaction. The challenge of creating a coarse-grained model is that it should facilitate the numerical effort while still governing the essential physics accounting for the dynamics of the complex fluid. The dynamics include thermal fluctuations causing Brownian motion, long-range hydrodynamic forces transmitted by the interaction of the solvent with the polymer's components and with itself but

also the obedience of basic laws of physics, e.g., conservation of energy, momentum, and mass. The complexity of the problem can be reduced via coarse-graining, but it typically remains unfeasible for any calculation of non-equilibrium properties by hand. The dramatic reduction of the fluid's degrees of freedom makes an implementation of the system in computer simulations possible. The most important contributions to the system dynamics are thereby displayed on a mesoscale approach that tries to bridge the large gaps in length- and time scales occurring.

Within the scope of molecular dynamics simulations (MD) this thesis studies the conformations of single unknotted ring polymers when they are exposed to a combination of long-range hydrodynamic interactions (HI) and shear flow. The polymers are modelled both as fully flexible rings with excluded volume for their monomers and as supercoiled polymers, which are more rigid and whose constituents bare a more complex structure. HI are expected to play a major role in the dynamics of a dilute suspension of ring polymers in contrast to polymer melts of high density where the HI are diminished by screening effects [6, 7, 8]. Supercoiling is implemented by considering bending and torsional stiffness in the dynamics of the polymers. HI and shear flow are added by using a coarse-grained model to mimic the effects of a solvent interacting with the polymer. The combination of bending and torsional stiffness together with HI and shear flow allows for new insights into the dynamics of supercoiled ring polymers under non-equilibrium conditions and under the influence of an interactive solvent.

The algorithm used for the motion of the fluid transmitting the HI is called Multi-Particle Collision Dynamics (MPCD) and has been proposed by Malevanets and Kapral [9]. MPCD is a particle-based simulation technique that reproduces the flow of a Newtonian fluid in accordance with the Navier-Stokes equations. Depending on the choice of parameters the motion of the particles is either fluid- or gaslike [10]. They are described by continuous variables for their location and velocity and undergo alternating steps of ballistic streaming and a coarse-grained collision procedure. The latter uses random rotation matrices to calculate the solvent-solvent interaction with reduced numerical effort which is why it is also referred to as Stochastic Rotation Dynamics in literature. The random nature of the collision dynamics adds the effect of thermal fluctuations by construction. Because of its simplicity, the MPCD algorithm allows for a theoretical calculation of the fluid's transport coefficients and a direct measurement during simulation runs. Malevanets and Yeomans [11] proposed a simple method of coupling embedded objects, e.g., polymers or colloids, to the flow of the MPCD fluid. The solvent correctly reproduces HI between suspended particles and transfers Brownian fluctuations [12] to them. Typically, the colloidal dynamics is calculated separately by means of molecular dynamics and the MPCD flow is joined to the molecular system. The explicit effect of HI on molecular systems can only be determined, if there is way of switching it off. Ripoll et al. [13] presented an alternative algorithm that replaces the solvent point particles by a heat bath. It has all the features of MPCD except for the presence of

HI and allows for a direct comparison with the actual MPCD algorithm. MPCD is an ideal method to investigate the non-equilibrium properties of complex fluids at Reynolds numbers of order 0.1 to 10, especially in situations where the effects of thermal fluctuations and hydrodynamics are important [14]. Because it is inexpensive compared to molecular dynamics simulations with explicit fluid particles, MPCD bridges the typical time scales linked to the solvent and the solute. Padding and Louis [5] have discussed the question of how to match the parameters of the fluid simulation so that the length- and time scales appearing can be mapped consistently to the ones of real colloidal systems.

MPCD has been used to investigate the properties of systems in solution, e.g., sedimentation of claylike colloids [15], vesicles [16], nematic liquid crystals [17, 18], and soft active matter [19]. Lees-Edwards boundary conditions [20] establish a shear flow profile within the solvent which has been used to study the response of polymers of various topologies in dilute [21, 22, 23, 24, 25, 26], semidilute [7], and concentrated suspensions [8, 27, 28]. In this context, ring polymers have attracted special interest since their behaviour to shear flow sets them apart from polymers of other topologies and depends on the presence or absence of HI. With the help of MD simulations, Liebetreu and Likos [29, 30] have found an inflation phase of ring polymers in a certain range of shear flow strengths. In the inflation regime the rings remain in an open rigid conformation without the typical dynamical behaviour of such systems, e.g., tumbling or tank treading. The inflation can only happen with the presence of HI which provide for an effective solvent backflow which is reflected from the polymer's ends along flow direction back to the molecule's center, thereby blowing up the ring's 'belly'. Recently, this theoretical prediction has been confirmed in microfluidic experiments [4]. The swelling of the ring reflects the mutual interplay between polymer and solvent where the former is influenced in its conformations and the latter in its flow profile. Consequently, the behaviour is not replicated with a solvent that does not convey HI under otherwise the same conditions. In cluster glasses of ring polymers, shear thinning and stack orientation have been observed as the response to shear flow [6].

Smrek et al. [31] have studied entangled solutions of supercoiled circular DNA of different degrees of polymerization and supercoiling by means of computer simulations. They applied a model containing constraints to the bending and torsional angles between chain neighbours whereby the latter was realized by using patchy polymers. In this thesis, this model is adopted to perform molecular dynamics simulations of dilute solutions of supercoiled polymers. Coupling to the MPCD solvent adds hydrodynamic interactions to their dynamics. The ability to switch off HI while not affecting the remaining solvent characteristics allows one to study possible effects of HI on their dynamics and conformations while the exposure to shear flow simulates the polymer in a non-equilibrium system.

The thesis is organised as follows: The details of the MPCD algorithm, the properties of

the fluid that it describes, and its use in MD simulations are discussed thoroughly in section 2. The MD simulation of a ring polymer with excluded volume is presented in section 3. An implementation of the model used in [29, 30], which is coupled to the MPCD fluid, demonstrates the effects of HI on ring polymers and replicates the rigid inflated behaviour under shear flow which has been observed previously. In section 4, the model is supplemented with terms for torsional and bending stiffness and two different approaches to the implementation of the monomers as rigid bodies are discussed. The details of their rotational dynamics are analyzed and subsequently, their properties in the MPCD solvent are presented and discussed. Finally, the supercoiled rings are subject to shear flow and the resulting behaviour is investigated in section 5 and this thesis is closed by a conclusion in section 6. Some technical details to the coding of the simulations and their evaluations as data, plots, and images are mentioned shortly in Appendix A.

2 Multi-Particle Collision Dynamics

In this section the basics of the MPCD algorithm are explained and discussed including its physical properties, the generation of shear flow, thermostating in non-equilibrium systems, coupling to suspended objects, and switching off HI. Expressions for the transport coefficients and dimensionless numbers characterising the fluid dynamics are presented and compared to values measured in simulation runs.

2.1 Coarse-Grained Hydrodynamic Interactions

MPCD models the solvent fluid as N_s individual point particles with mass m_s within a rectangular simulation box with side lengths L_x, L_y, L_z. Positions and velocities are described by continuous variables $\vec{r}_i, \vec{v}_i$. The algorithm consists of two alternating steps. During the streaming step the particles are allowed to move ballistically with their current velocities for a time period h [9]:

$$\vec{r}_i(t+h) = \vec{r}_i(t) + h\vec{v}_i(t). \tag{1}$$

Periodic boundary conditions are applied for particles crossing the dimensions of the simulation box, i.e., if $r_{i\alpha}(t+h) > L_\alpha$, then $r_{i\alpha}(t+h) \mapsto r_{i\alpha}(t+h) - L_\alpha$, respectively, if $r_{i\alpha}(t+h) < L_\alpha$, then $r_{i\alpha}(t+h) \mapsto r_{i\alpha}(t+h) + L_\alpha$. The idea is that periodic images of a central simulation box are placed regularly in a lattice and make up an infinitely extended fluid which is periodic in space. The particles´ position variables are confined within the dimensions of the central box where the entire simulation takes place.

The subsequent collision step implements the internal forces exchanged among solvent particles with a coarse-graining method. This is accomplished without the presence of energy potentials and hence there are no systematic forces acting. Instead, after free propagation for a time length h momentum and energy are redistributed among particles within a restricted range during the collision step. Particles are sorted into cells according to their current positions and they only interact with members of their own cell. For this purpose, the entire simulation box is coarse-grained to cells of a grid, typically chosen to be cubic with lattice constant a_c, although other geometries are possible. The velocities of all N_c particles in one particular cell are summed up to a center-of-mass velocity,

$$\vec{v}_{\mathrm{c.m.}}(t) = \frac{1}{N_c} \sum_{i \in \mathrm{cell}} \vec{v}_i(t). \tag{2}$$

Next, an orthogonal matrix $\mathbf{R}[\alpha]$ is generated for the cell. The rotation angle has a fixed value α,

but the orientation of the rotation axis is picked randomly at each time step and varies from cell to cell. This randomness is the ingredient that endows MPCD with thermal fluctuations. The velocities of all particles within the cell are rotated relative to the cell´s center-of-mass velocity,

$$\vec{v}_i(t+h) = \vec{v}_{\text{c.m.}}(t) + \mathbf{R}[\alpha](\vec{v}_i(t) - \vec{v}_{\text{c.m.}}(t)), \tag{3}$$

which mimics the collision of the particles. The procedure is conducted for all $L_x L_y L_z a_c^{-3}$ cells contained in the simulation box. This collision step allows for local momentum exchange among particles within a cell without changing $\vec{v}_{\text{c.m.}}$. Notice that the internal interaction of the simulated fluid is coarse-grained both in space (the division into cells) and time (collision at discrete time steps nh) [9]. Because of the lack of systematic forces, MPCD solvent particles obey an ideal gas equation of state [14].

The rotation matrix $\mathbf{R}[\alpha]$ is derived independently in every collision cell by picking two random numbers from uniform distributions, $\theta \in [0, 2\pi]$ and $\phi \in [-1, 1]$ which define the components $\mathbf{R}_i[\alpha]$:

$$\mathbf{R}_x[\alpha] = \sqrt{1-\theta^2}\cos(\phi),\ \mathbf{R}_y[\alpha] = \sqrt{1-\theta^2}\sin(\phi),\ \mathbf{R}_z[\alpha] = \theta. \tag{4}$$

The rotation itself can be simplified to the expression

$$\begin{aligned}\vec{v}_i(t+h) =& \vec{v}_{\text{c.m.}}(t) + \cos(\alpha)[\Delta\vec{v}_i(t) - (\Delta\vec{v}_i(t)\mathbf{R})\mathbf{R}] \\ &+ \sin(\alpha)\mathbf{R}\times[\Delta\vec{v}_i(t) - (\Delta\vec{v}_i(t)\mathbf{R})\mathbf{R}] + (\Delta\vec{v}_i(t)\mathbf{R})\mathbf{R},\end{aligned} \tag{5}$$

where $\Delta\vec{v}_i(t) = \vec{v}_i(t) - \vec{v}_{\text{c.m.}}(t)$ is the velocity relative to the respective center-of-mass velocity. Local conservation of mass, momentum, and energy have to hold true for the MPCD-procedure to be a valid fluid simulation technique that conveys hydrodynamic interactions. It can be shown that the collision step (3) conserves all three quantities at cell-level. It does not change the number of particles in a cell so that local conservation of mass is given trivially. By calculating the total momentum of a collision cell and its total energy after performing (3):

$$\begin{aligned}\vec{P}_{\text{cell}}(t+h) &= \sum_{i\in\text{cell}} m_s\vec{v}_i(t+h) = m_s\sum_{i\in\text{cell}}[\vec{v}_{\text{c.m.}} + \mathbf{R}[\alpha](\vec{v}_i(t) - \vec{v}_{\text{c.m.}})] \\ &= N_c m_s\vec{v}_{\text{c.m.}} + m_s\mathbf{R}[\alpha]\sum_{i\in\text{cell}}[\vec{v}_i(t) - \vec{v}_{\text{c.m.}}] \\ &= N_c m_s\vec{v}_{\text{c.m.}} + N_c m_s\mathbf{R}[\alpha][(\frac{1}{N_c}\sum_{i\in\text{cell}}\vec{v}_i(t)) - \vec{v}_{\text{c.m.}}] \\ &= N_c m_s\vec{v}_{\text{c.m.}} = \sum_{i\in\text{cell}} m_s\vec{v}_i(t) = \vec{P}_{\text{cell}}(t),\end{aligned} \tag{6}$$

$$
\begin{aligned}
E_{\text{cell}}(t+h) &= \frac{m_s}{2}\sum_{i\in\text{cell}}\vec{v}_i^{\,2}(t+h) = \frac{m_s}{2}\sum_{i\in\text{cell}}[\vec{v}_{\text{c.m.}} + \mathbf{R}[\alpha](\vec{v}_i(t)-\vec{v}_{\text{c.m.}})]^2 \\
&= \frac{m_s}{2}\left(N_c\vec{v}_{\text{c.m.}}^{\,2} + 2\vec{v}_{\text{c.m.}}\mathbf{R}[\alpha]\sum_{i\in\text{cell}}(\vec{v}_i(t)-\vec{v}_{\text{c.m.}}) + \sum_{i\in\text{cell}}|\mathbf{R}[\alpha](\vec{v}_i(t)-\vec{v}_{\text{c.m.}})|^2\right) \\
&= N_c\frac{m_s}{2}\vec{v}_{\text{c.m.}}^{\,2} + \frac{m_s}{2}\sum_{i\in\text{cell}}(\vec{v}_i(t)-\vec{v}_{\text{c.m.}})^2 \\
&= \frac{m_s}{2}\sum_{i\in\text{cell}}\vec{v}_i^{\,2}(t) + N_c m_s\vec{v}_{\text{c.m.}}^{\,2} - m_s\vec{v}_{\text{c.m.}}\sum_{i\in\text{cell}}\vec{v}_i(t) \\
&= \frac{m_s}{2}\sum_{i\in\text{cell}}\vec{v}_i^{\,2}(t) - m_s\vec{v}_{\text{c.m.}}\sum_{i\in\text{cell}}(\vec{v}_i(t)-\vec{v}_{\text{c.m.}}) \\
&= \frac{m_s}{2}\sum_{i\in\text{cell}}\vec{v}_i^{\,2}(t) = E_{\text{cell}}(t),
\end{aligned}
\tag{7}
$$

one can see that momentum and energy conservation hold true at cell-level. Mass, momentum, and energy of the entire system are made up of all cell contributions and therefore, also remain constant. The conservation of momentum is equivalent to the center-of-mass velocity being unaffected by the collision step. The calculations above use the fact that $\sum_{i\in\text{cell}}(\vec{v}_i(t)-\vec{v}_{\text{c.m.}}) = N_c(\vec{v}_{\text{c.m.}}-\vec{v}_{\text{c.m.}}) = 0$ and $|\mathbf{R}[\alpha](\vec{v}_i(t)-\vec{v}_{\text{c.m.}})| = |\vec{v}_i(t)-\vec{v}_{\text{c.m.}}|$, since $\mathbf{R}[\alpha]$ is orthogonal. Given that the number of particles and the volume are also conserved the MPCD solvent represents a microcanonical ensemble. Frisch et al. [32] demonstrated that a fluid algorithm recovers the dynamics of the Navier-Stokes equations in the continuum limit as long as the procedure conserves energy, momentum, and mass and discretises space in a sufficiently symmetric manner. Therefore, Therefore, MPCD is an effective way of solving the Navier-Stokes equations and reproducing hydrodynamic interactions and thermal fluctuations down to the size of a collision cell.

The procedure described above can be modified to related algorithms with similar properties but some distinct features. They form a class of algorithms that is often referred to as multi-particle collision (MPC) [14]. In this more general context the original version used in this thesis is often called stochastic rotation dynamics (SRD) instead of MPCD to distinguish it from other similar algorithms. To name a few examples of MPC variants: (i) External forces can be included the streaming by introducing the (total) external force $\vec{f}_i$ on fluid particles i and considering it in the streaming step (1) [33]:

$$
\begin{aligned}
\vec{v}_i(t+h) &= \vec{v}_i(t) + h\frac{\vec{f}_i(t)}{m_s}, \\
\vec{r}_i(t+h) &= \vec{r}_i(t) + h\vec{v}_i(t) + \frac{h^2}{2}\frac{\vec{f}_i(t)}{m_s}.
\end{aligned}
\tag{8}
$$

The external force in the alternative streaming step (8) has been used for instance to generate a parabolic flow profile in a slit channel [23, 8] or to account for backflow effects in sedimentation processes with periodic boundary conditions [33]. Shear flow will be introduced in a similar fashion. Instead of an external force term, a modification of the periodic boundary conditions will generate a one-dimensional, linear velocity gradient. (ii) MPCD/SRD does not conserve angular momentum [34] which is not crucial for many applications. Götze et al. have found systems where the missing conservation law does indeed lead to deviations from a Newtonian fluid [35]. The algorithm above can be modified to restore conservation of angular momentum [36] by adapting the collision angle in every cell instead of keeping it constant. The conservation of angular momentum comes at the cost of higher computational effort. (iii) Stochastic rotations are not the only tool to perform the collision step (3). Allahyarov and Gompper [37] have presented an alternative collision rule based on the idea that the updated velocities can also be generated as new random Gaussian numbers. The collision is performed in a way that the center-of-mass velocity of a cell is still conserved and conservation laws apply for energy and momentum. It couples the solvent momenta to an Andersen thermostat which is why it is often referred to as MPC-AT and why the algorithm models the fluid in a canonical ensemble rather than a microcanonical one. The original MPC-AT [37] again does not conserve angular momentum. Noguchi et al. have presented a variation of MPC-AT [38] that fulfills the additional conservation law. The numerical effort of MPC-AT is higher compared to SRD/MPCD because of the large amount of random numbers that have to be generated. Its advantage is that it comprises a thermostat so that none has to be added when simulating non-equilibrium systems where the total energy has to be held at a constant value artificially.

In the MPCD simulations three basic units are set to unity, namely the fluid particle's mass m_s, the length of the (cubic) collision cells a_c, and the energy k_BT specifying the average kinetic energy of a solvent particle by $3k_BT = m_s\langle\vec{v}_i^2\rangle$. This corresponds to expressing length, energy, and mass in units of a_c, k_BT, and m_s. A reference unit for time can then be derived by $t_{\mathrm{MPCD}} = a_c\sqrt{\frac{m_s}{k_BT}} = 1$. Four independent simulation parameters have to be defined: the box dimensions L_x, L_y, L_z, the time length between collisions h, the particle density $\rho = \frac{N_s}{L_xL_yL_z}$, and the collision angle α. The choice of independent parameters affects the overall dynamics of the solvent and Padding and Louis [5] discussed how the units emerging from the coarse-graining method can be mapped to real values in nature, e.g., the according to the properties of water.

For short time steps h the mean free path $\Lambda = h\sqrt{\frac{k_BT}{m_s}} = h$ between consecutive collisions is small compared to the cell size. The discrete nature of the grid causes particles to stay in the same cell for several collisions before particle exchange with neighbouring cells can happen. This causes correlations between particle velocities within collision cells and breaks the translational symmetry of the system. Albeit particles are paired into cells, Galilei invariance can still be recovered by

performing a random shift of all particle positions relative to the sorting grid before the particles are grouped into cells [39]. The components of the shift vector $\delta\vec{r}$ are sampled uniformly from $[-\frac{a_c}{2}, \frac{a_c}{2}]$. After performing (2) and (3) all particles are shifted back by $-\delta\vec{r}$, such that none of the conservation laws are violated. The uniform shift by a random vector counteracts the tendency of particles to interact with the same group of neighbours and therefore prohibits the formation of correlations within cells. Additionally, the shifting procedure accelerates momentum transfer between particles [39].

In their original paper [9] Malevanets and Kapral derived an H-Theorem for the MPCD model. Therefore, the solvent particles' velocities follow a Maxwell-Boltzmann distribution in the system´s stationary state. Further, they showed that the MPCD algorithm leads to a Poisson distributed particle density, i.e., the probability to find N particles in a randomly chosen cell is given by:

$$P_\rho(N) = \frac{\rho^N}{N!} e^{-\rho}. \tag{9}$$

The MPCD solvent used in this thesis is initialised by filling each cubic cell of a rectangular simulation box with exactly $\rho = 10$ point particles in random locations within cells. Their initial velocities $\vec{v}_{i,0}$ are picked independently from a Maxwell-Boltzmann distribution preferably such that it is already in the stationary state. Alternatively, in order to demonstrate if the MPCD algorithm indeed produces a Maxwell-Boltzmann distribution and if energy is conserved, $\vec{v}_{i,0}$ can also be picked from a uniform distribution. In either case, the distributions $f_{|\vec{v}_0|}$ in question must be normalised, $\int_0^\infty f_{|\vec{v}_0|} dv_0 = 1$ and in accordance with a given energy $k_B T$, $\int_0^\infty f_{|\vec{v}_0|} \vec{v}_0^2 dv_0 = 3\frac{k_B T}{m_s}$. Fig. 1 depicts the transition from an initial state, where both the particle velocity and density are initially uniformly distributed (1a and 1c), to a stationary state after equilibration (1b and 1d). The system is allowed to evolve in time for a duration long enough that both quantities under investigation reach their stationary distributions. Typically, it takes only a few hundred time steps starting from uniform initial conditions. The energy is conserved for all three values of $k_B T = 1, \frac{1}{4}, 4$, and the velocity distribution is indeed found to be Maxwellian, which corresponds to the behaviour of an ideal gas. The stationary state of the particle number is found to be Poisson distributed. This holds true even when shear flow is imposed. Before moving on to sheared systems some properties of the solvent´s flow dynamics will be investigated for the case that no external forces are applied.

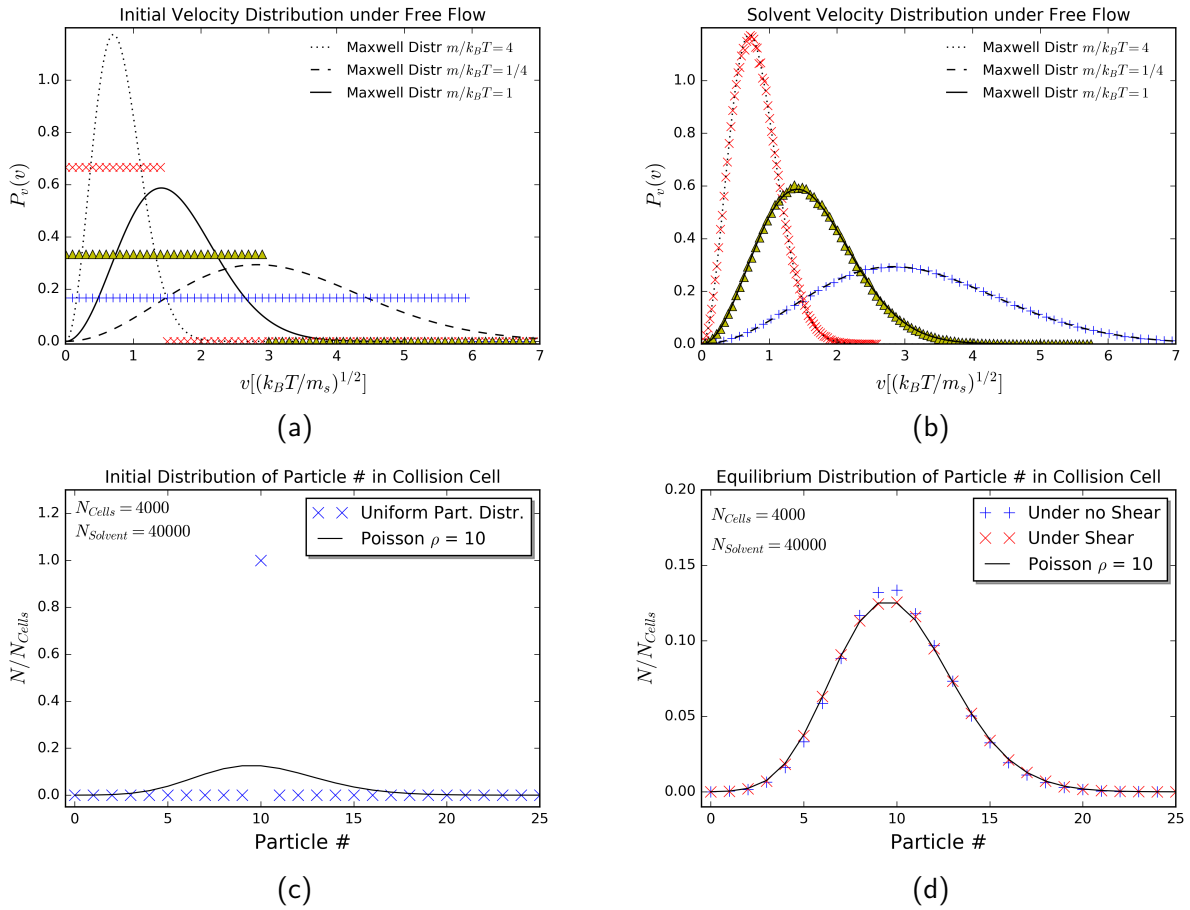

Figure 1: (a) Initial and (b) stationary velocity distributions for different initial energies $4, 1$, and $\frac{1}{4}$, (c) initial and (d) stationary particle number distribution of MPCD fluid (both with and without shear flow). Markers show simulation data, lines show theoretical curves.

2.2 Dynamical Properties of the Solvent

A nice feature of the MPCD algorithm is that it allows for an easy analytical calculation of transport coefficients due to its simplicity. There are two alternative ways of deriving them [14]. In the first approach Ihle and Kroll [39, 40] derived Green-Kubo relations for the kinematic viscosity ν_{GK} and the self-diffusion coefficient D for the MPCD fluid. By resumming the Green-Kubo relations Ihle and al. [41] derived the analytical expression ν_{GK} which is composed of a kinetic and a collisional contribution:

$$\nu_{\mathrm{GK}} = \nu_{\mathrm{GK}}^{\mathrm{kin}} + \nu_{\mathrm{GK}}^{\mathrm{col}}, \tag{10}$$

$$\nu_{\mathrm{GK}}^{\mathrm{kin}} = \frac{k_B T}{m_s}\frac{h}{2}\left(\frac{5\rho}{(\rho - 1 + e^{-\rho})(2 - \cos(\alpha) - \cos(2\alpha))} - 1\right), \tag{11}$$

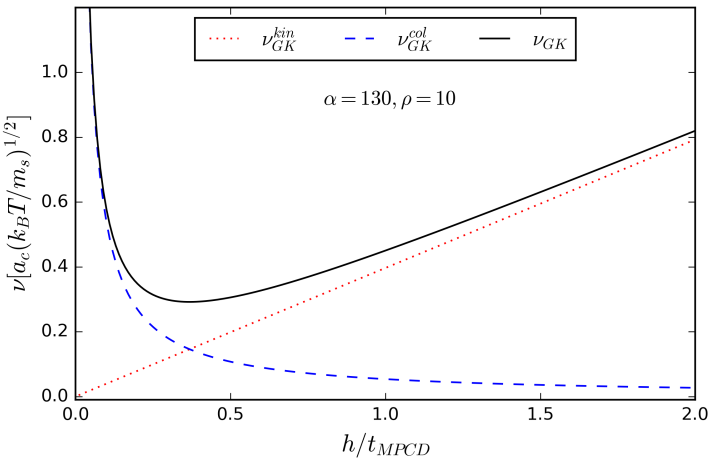

Figure 2: Kinematic viscosity calculated with Green-Kubo relations and assuming molecular chaos as a function of h. $\alpha = 130°$ and $\rho = 10$.

$$\nu_{\mathrm{GK}}^{\mathrm{col}} = \frac{a_c^2}{18h}\left(\frac{\rho - 1 + e^{-\rho}}{\rho}\right)(1 - \cos(\alpha)). \tag{12}$$

Kikuchi et al. [42] introduced an alternative non-equilibrium approach to derive analytical expressions for the fluid's shear viscosity. They evaluate the linear response to an imposed shear gradient. Both methods lead to the same expressions for the transport coefficients [41] and both make the assumption of molecular chaos while deriving the kinetic part of the kinematic viscosity (11) which means that the velocities of different particles are uncorrelated, i.e., $\langle \vec{v}_i(t)\vec{v}_j(t')\rangle = \delta_{ij}\langle \vec{v}_i(t)\vec{v}_i(t')\rangle$ [33]. The MPCD solvent is a Newtonian fluid, i.e., the viscosity is independent of the shear rate applied. In Fig. 2 the theoretical curves (10)-(12) are plotted as functions of the collision time step. The magnitude of the two contributions varies significantly with the choice of h such that the total viscosity is dominated by either one of them. Kinetic transport of any quantity is due to the movement of the particles themselves carrying mass, momentum, and energy through space. In the context of MPCD, $\nu_{\mathrm{GK}}^{\mathrm{kin}}$ dominates for large collision time steps where particles are able to cover large distances during the streaming step. Collisional transport on the other hand refers to the exchange of momentum and energy due to the interaction during the collision step. It is dominant for small h, where the mean free path between consecutive hits is short. The dynamics of gases is usually dominated by kinetic transport, while in fluids the transport of momentum and energy is mainly due to collisions [10].

The theoretical prediction of the self-diffusion coefficient D_{GK} of the MPCD solvent has only a kinetic contribution since mass is not transferred during collisions [40]:

$$D_{\mathrm{GK}} = \frac{k_BT}{m_s}h\left(\frac{3\rho}{2(\rho - 1 + e^{-\rho})(1 - \cos(\alpha))} - \frac{1}{2}\right) = \frac{k_BT}{m_s}h\left(\frac{1}{\gamma} - \frac{1}{2}\right), \tag{13}$$

with the decorrelation factor $\gamma = 2(\rho - 1 + e^{-\rho})(1 - \cos(\alpha))(3\rho)^{-1}$. There are two ways of measuring the self-diffusion coefficient of the simulated fluid experimentally. The first one uses the mean square displacement (MSD),

$$D_{\mathrm{MSD}} = \lim_{t\to\infty} \frac{1}{6t} \langle [\vec{r}_i(t) - \vec{r}_i(0)]^2 \rangle, \tag{14}$$

where the brackets indicate an average over all particles. Alternatively, one can apply the Green-Kubo relations for discrete systems to expression (14) and derive:

$$\begin{aligned} D_{\mathrm{VACF}} &= \frac{h}{3}\left(\frac{1}{2}\langle \vec{v}_i(0)^2 \rangle + \sum_{n=1}^{\infty} \langle \vec{v}_i(nh) \cdot \vec{v}_i(0) \rangle\right) \\ &= \frac{h}{3}\langle \vec{v}_i(0)^2 \rangle \left(\frac{1}{2} + \sum_{n=1}^{\infty} C_V(nh)\right) = \frac{k_B T}{m_s} h \left(\frac{1}{2} + \sum_{n=1}^{\infty} C_V(nh)\right), \end{aligned} \tag{15}$$

where $C_V(nh)$ represents the velocity auto-correlation function (VACF) at discrete time steps nh:

$$C_V(nh) = \frac{\langle \vec{v}_i(nh) \cdot \vec{v}_i(0) \rangle}{\langle \vec{v}_i(0)^2 \rangle}. \tag{16}$$

The analytical formula for D_{GK} in (13) can be recovered from (15) with the assumption of molecular chaos which implies an exponential decay of the VACF, i.e., $C_V(nh) = (1-\gamma)^n$. Ripoll et al. [10] demonstrated that spatial correlations build up between particles in a cell for $\Lambda/a_c \ll 1$ which creates deviations from the transport dynamics predicted by molecular chaos.

The self-diffusion coefficient of the MPCD fluid algorithm used in this thesis was measured by means of both the MSD and the VACF for different collision time steps. The experimental data points were calculated as averages taken over the coordinates of all N_s particles of multiple ensembles. The results are plotted in Fig. 3a as functions of h next to the theoretical linear from (13). Both approaches lead to curves that follow the linear trend in general. However, D_{VACF} shows a greater statistical deviation from D_{GK} compared to D_{MSD}, the self-diffusion coefficient measured via MSD. Taking the average over even more ensembles would definitely narrow down the error $\frac{D_{\mathrm{VACF}} - D_{\mathrm{GK}}}{D_{\mathrm{GK}}}$.

$D_{\mathrm{MSD}}(h)$ agrees well with the predicted linear growth. An interesting phenomenon occurs for $h \to \infty$, which becomes more apparent by examining the relative error $(D_{\mathrm{MSD}} - D_{\mathrm{GK}})/D_{\mathrm{GK}}$. It is plotted as function of the MPCD collision time h, see Fig. 3b. For $h/t_{\mathrm{MPCD}} \cong 1$ the self-diffusion coefficient measured agrees with D_{GK}, whereas for $h/t_{\mathrm{MPCD}} \lesssim 0.5$ D_{MSD} starts to

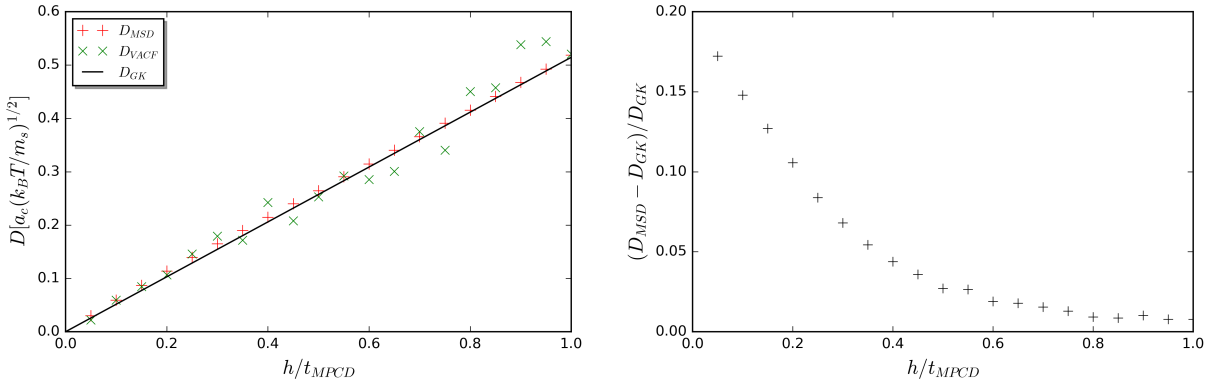

(a) (b)

Figure 3: Self-diffusion coefficient measured vs. analytical. (a) Simulation results for the self-diffusion coefficient as a function of the MPCD time step length. Values were measured by means of both the MSD (red) and the VACF (green). The linear curve marks the analytical expression (13). (b) Ratio of self-diffusion coefficient measured via MSD to analytical expression as a function of the MPCD time step length.

increase with decreasing h. The deviation from (13) indicates that the assumption of molecular chaos is no longer valid for small mean free paths, because particles are more likely to remain in the same vicinity for multiple time steps, such that the particle velocities build up correlations.

The kinematic viscosity was computed experimentally for the MPCD algorithm by Ripoll et al. [10]. Although the derivation of the kinetic contribution makes the assumption of molecular chaos, it was shown to fit the theoretical function (10), even for $\Lambda < 0.5$. In contrast to D_{GK}, ν_{GK} has a collisional contribution. For small h it is much larger than the kinetic part so that any effects beyond molecular chaos do not affect the viscosity as much.

The violation of molecular chaos can be testified by looking at the VACF of MPCD solvents in two different regimes. In the first one the mean free path equals the collision cell size whereas in the other one the mean free path measures only 10% of the cell. Fig. 4 shows the VACF of the simulated systems computed as a function of time. The plots are compared to the curves of exponential decay illustrated by the dotted lines for intermediate times $t \leq 10\, t_{\mathrm{MPCD}}$. For $\Lambda = 1.0$ the VACF follows the exponential curve for the first two time steps before long-time tail behaviour occurs. The deviation sets in after a much shorter time for the fluid with $\Lambda = 0.1$ since the time passed nh after n collisions is shorter for smaller h. The VACF decays slower than the exponential curve $C_V(nh) = (1-\gamma)^n$ which is characteristic for molecular chaos.

The analytic expressions for the transport coefficients (10) - (13) can be used to derive some dimensionless numbers that characterises the flow regime of the MPCD solvent. They are valid within the assumption of molecular chaos, which should be a good approximation up to a small deviation of the experimentally measured self-diffusion coefficient for $\Lambda \lesssim 0.5$.

The Schmidt number $\mathrm{Sc} = \nu/D$ is defined as the ratio between momentum transport and

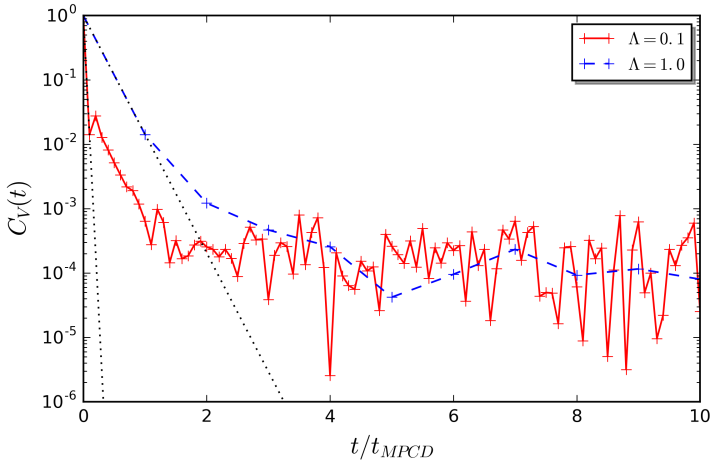

Figure 4: Experimentally measured velocity auto-correlation function as a function of time for mean free paths $\Lambda = 0.1$ and $\Lambda = 1.0$. The particle density is $\rho = 10$, the collision angle is $\alpha = 130°$, and the simulation box is cubic with size $L = 20$. The VACF stops following the exponential decay after only a few collision steps. The dotted lines indicate the theoretical exponential curves.

mass transport. For gases Sc typically ranges around or below unity, while in fluids, where momentum transport dominates, it is much larger than unity. In real liquids like water it usually has a value between 10^2 and 10^3 [10]. The theoretical approximation Sc$= \nu_{\mathrm{GK}}/D_{\mathrm{GK}}$ is plotted in Fig. 5a on the left as a function of h and for different choices of the collision angles and the particle densities. The curves scale like $\mathrm{Sc} \sim \mathrm{const.} + \Lambda^{-2}$ and predict two different regimes. For large mean free paths the Schmidt number is constant and does not depend on h. In this regime the kinetic contribution to the viscosity prevails the collisional one and Sc is of order 1 to a maximum of $\lesssim 10$ for a collision angle of almost 180°. On the other end, for $\Lambda \lesssim 1$, the collisional contribution becomes relevant and increases the Schmidt number. For a given value of $h \lesssim 1$ Sc increases significantly with α, whereas raising ρ has only little effect. The plot shows why the collision time step h should be picked from $\{0.01, ..., 0.1\}$ and the collision angle ought to be fairly high. For $h \gg 0.1$ or small α MPCD can not provide the correct hydrodynamic regime of a fluid. The choice of parameters for this thesis results in $\mathrm{Sc} \approx 2 \times 10^1$ which can be seen to fulfill the condition $\mathrm{Sc} \gg 1$, i.e., it should simulate a fluid well enough. In theory a higher Schmidt number could be obtained by lowering h but only at the cost of reducing computational efficiency.

The Reynolds number is defined as $\mathrm{Re} = \frac{u_s L}{\nu}$ which is given by $\sqrt{\frac{k_B T}{m_s}} \frac{a_c}{\nu} \sim \nu^{-1}$ for the pure solvent, where $u_s = \sqrt{\frac{k_B T}{m_s}}$ is the speed of the solvent particles and the characteristic length L is set to be the size of a collision cell a_c. The diameter of particles in real colloidal suspensions are on the order of a few nm up to a few $\mu\mathrm{m}$ since viscous forces dominate the dynamics. In such systems the Reynolds number is barely higher than 10^{-3} [5]. The simulation of the complex fluid is

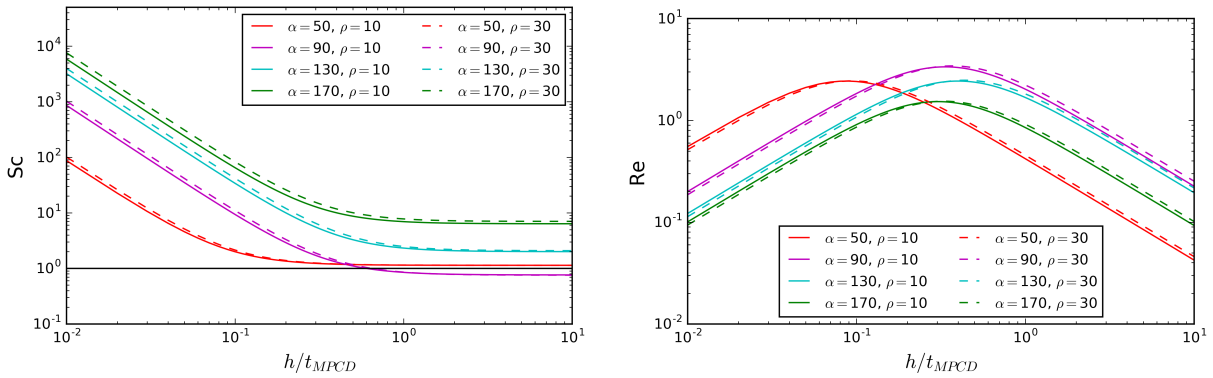

(a) (b)

Figure 5: Dimensionless Schmidt number (a) and Reynolds number (b) of MPCD fluid calculated analytically with Green-Kubo relations under the assumption of molecular chaos as a function of h for different choices of collision angles α and particle densities ρ.

supposed to create comparable conditions as in nature and therefore, should also have a small Re. The pure solvent is expected to have a higher Reynolds number compared to the situation when a polymer is suspended since its addition is expected to raise the viscosity of the fluid. Therefore, calculating Re for the pure solvent gives an upper limit for the value when an object is embedded. The theoretical curve $\mathrm{Re} = \nu_{\mathrm{GK}}^{-1}$ is plotted in Fig. 5b. Throughout all choices of parameters Re is of the order $\sim 10^{-1}$ to ~ 1, if you keep h in the range $\{0.01, ..., 0.1\}$. The Re curves have a local maximum at $h/t_{\mathrm{MPCD}} \sim 10^{-1} - 1$ and decrease for higher values of h. In general, the Reynolds number should neither be too high nor too low in mesoscale simulations: $\mathrm{Re} \gg 1$ demands for a small time step and high spatial resolution to capture turbulent behaviour. For $\mathrm{Re} \ll 1$ the flow velocities are very slow and longer simulation times are necessary until particles have travelled a significant distance.

It is possible for the complex fluid simulated to have large Schmidt numbers and Reynolds numbers neither too low nor too high by picking a small time step length $h < 0.1$. It is still convenient to keep it above a certain value $h > 0.01$ in order to reduce computational effort and violation of Galilei-invariance. Padding and Louis [5] evaluated further dimensionless numbers of the MPCD fluid and how to tune the model parameters so that MPCD fluid has the desired properties that match a real solvent. They noticed that the Mach number is high in comparison to real water so that the MPCD solvent models a compressible medium. As a consequence of the coarse-graining, which defines MPCD particles as representatives of the fluid flow, the particle mass m_s is way larger than the mass of a fluid particle in nature which results in lower velocities. The density is also lower which causes less frequent collisions. Both effects bring about a low speed of sound and hence, a high Mach number.

2.3 Non-Equilibrium MPCD Systems

The periodic boundary conditions that MPCD fluid particles are subject to can be interpreted as follows: The simulation box is the central piece in a grid of periodic images. The central box borders with its copies so that whenever a particle leaves the box, its periodic image enters the box from the respective opposite side. To generate shear flow these periodic boundaries are modified to Lees-Edwards boundary conditions [20]. The general idea is depicted in Fig. 6. One Cartesian axis is selected to be the gradient direction (here: the y-direction), a second one to be the flow direction (here: the x-direction), and the remaining axis is termed the vorticity direction (here: the z-direction). The periodic images of the box lying in the flow-vorticity plane containing the central box remain stationary and periodic boundary conditions are still applied to particles leaving the simulation box in x or z directions. Shear flow is conceptually introduced by imagining the upper and lower layer of copies in gradient direction to move along flow direction with the speed $\vec{v}_{\text{boost}}$ (upper layer) and $-\vec{v}_{\text{boost}}$ (lower layer). When a particle crosses over the boundary in positive gradient direction, a copy enters the box from the opposite layer which moves with a relative speed $-\vec{v}_{\text{boost}}$ and at time t it has been shifted by $-\Delta x(t) = -\text{mod}(\vec{v}_{\text{boost}}t, L_x)$. So the particle's entering position must be shifted in flow direction by $\Delta x(t)$ and its velocity is boosted by $-\vec{v}_{\text{boost}}$. Conversely, the upper layer is shifted by $\Delta x(t) = \text{mod}(\vec{v}_{\text{boost}}t, L_x)$ relative to the central box. A particle crossing over the boundary in negative gradient direction is replaced by another one from the upper layer. Therefore, its position is shifted by $\Delta x(t)$ and its velocity is lifted by $\vec{v}_{\text{boost}}$. This procedure generates a shear flow profile of the velocity distribution, which is

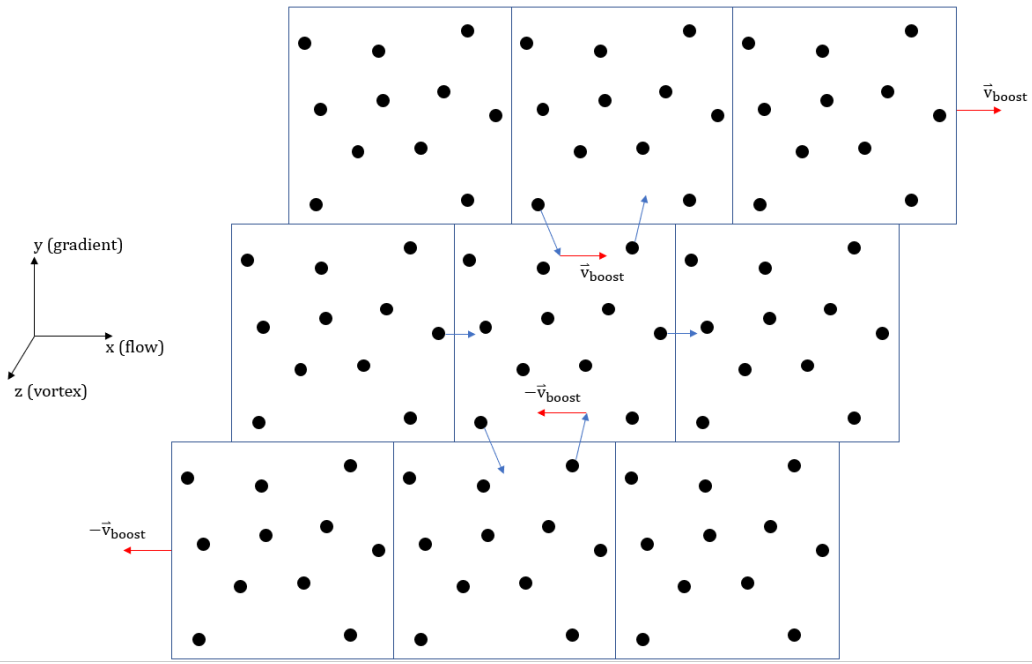

Figure 6: Illustration of Lees-Edwards boundary conditions where $\vec{v}_{\text{boost}} = L_y\dot{\gamma}\hat{e}_x$.

shown in Fig. 7a. For the calculation of the flow profile the central simulation box is divided into thin slices of thickness $\frac{a_c}{2}$ normal to the gradient direction. The velocity components are averaged over all particles within a slice and plotted as $\langle v_\alpha \rangle(y)$, $\alpha = x, y, z$, for discrete $y = \left(m + \frac{1}{2}\right)\frac{a_c}{2}$, $m = 0, 1, 2, ..., L_y - 1$. The application of Lees-Edwards boundary causes the mean velocity in flow direction to increase with a constant slope of $\dot{\gamma} = \vec{v}_{\text{boost}}/L_y$. The mean velocities in the gradient-vorticity plane remain zero like in the unsheared system.

By adding a boost to the velocity of particles crossing the gradient boundary energy is pumped into the system such that energy conservation is violated over time. In such a non-equilibrium system a thermostat algorithm has to keep the total energy at a constant value. In this project a cell-level thermostat is used, which was proposed by Gompper et al. [14], that holds the system's energy around a predefined energy $k_B T_0$. The following rescaling procedure is incorporated into (3) and performed independently in every collision cell:

1. Randomly select a real number $\Psi \in [1, 1 + c]$, where c is a small number and determines the strength of the thermostat.

2. Take this number as a scaling factor $S = \Psi$ with probability $1/2$; choose $S = 1/\Psi$ otherwise.

3. Create a random number $\xi \in [0, 1]$. If ξ is smaller than the acceptance probability $p_A = \min(1, A)$, where

$$A = S^{3(N_c - 1))} \exp\left(-\frac{m_s}{2 k_B T_0} \sum_{i \in \text{cell}} \left(\vec{v}_i - \vec{v}_{\text{c.m.}}\right)^2 \left(S^2 - 1\right) \right), \tag{17}$$

   the attempt will be accepted. N_c is the number of particles located in the cell.

4. If the attempt is accepted, perform the stochastic rotation (3) with the scaled rotation matrix $S\mathbf{R}[\alpha]$. If it is not accepted, rotate with the matrix $\mathbf{R}[\alpha]$. [14]

The thermostat regulates the particle velocities to a Maxwell-Boltzmann distribution and the deviation of the system's total energy from desired value $k_B T_0$ does not exceed 0.1%. In the simulations of this thesis the parameter of the thermostat strength is set to $c = 0.3$, which results in an acceptance rate of about 65%. At this value relaxation to the desired distribution is reached in only a few time steps. The cell-level thermostat was tested by letting it act on the three velocity distributions of Fig. 1b corresponding to solvents with different energies. After only a few collision steps all three systems collapse to the Maxwell-Boltzmann distribution corresponding to the energy $k_B T_0$, see Fig. 7b. This thermostat has been used successfully in MPCD simulations of claylike colloids [15].

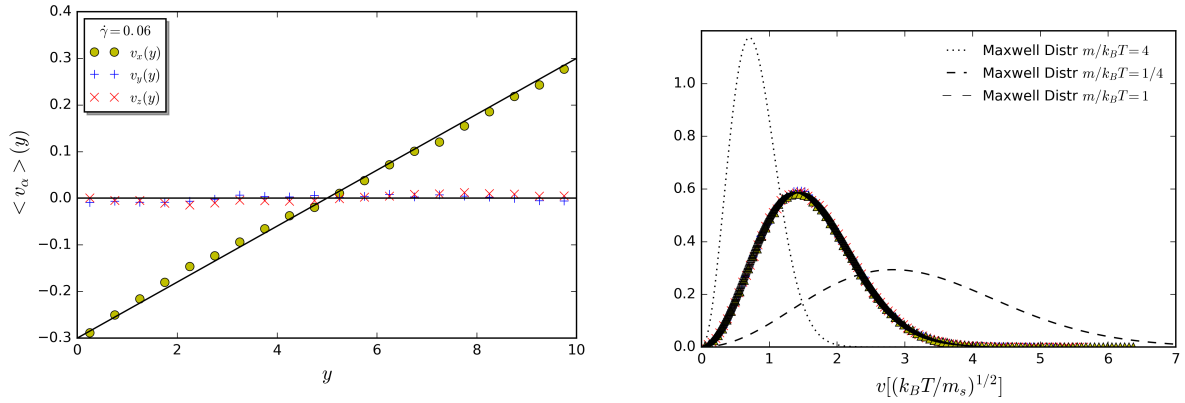

(a) (b)

Figure 7: (a) Shear gradient in MPCD fluid generated by Lees-Edwards boundary conditions with shear rate $\dot{\gamma} = 0.06$ and $L_y = 10$. (b) Equilibrium particle velocity distributions for different initial energies under shear flow and thermostat acting. Markers show simulation data.

It is important to note that the Lees-Edwards boundary conditions also have to be applied during the random shift restoring Galilean invariance. Particles close to the edge of the simulation box can cross over it during the shift; after the collision they are shifted back to their original location. Particles next to the boundary in gradient direction have large average drift velocities in flow direction due to shearing. If the initial shift makes them cross the edge, the velocity boost has to be added before the center-of-mass velocities are calculated. Otherwise the flow profile is annihilated by mixing particles of opposite drift velocities.

2.4 Coupling Embedded Objects to the MPCD Fluid

There is a straight-forward method of coupling embedded objects such as polymers to the flow of the MPCD solvent which was introduced by Malevanets and Yeomans [11]. The monomers composing the polymer chain are taken to be point particles with continuous momenta and positions. Their dynamics is governed by Newton´s equations implemented by means of a molecular dynamics simulation. The equations are integrated using the velocity Verlet algorithm with a time step δt which is usually a fraction of the collision time h. To create coupling with the fluid and thereby enable HI, the monomers participate in the MPCD collision step. A monomer i with mass m_m and velocity $\vec{v}_{m,i}$ contributes to the center-of-mass velocity of the collision cell that it is located in. If N_m is the number of monomers in a particular cell, the center-of-mass velocity (2) will be replaced by

$$\vec{v}_{\mathrm{c.m.}} = \frac{m_s \sum_{i \in \mathrm{cell}} \vec{v}_{s,i} + m_m \sum_{i \in \mathrm{cell}} \vec{v}_{m,i}}{N_s m_s + N_m m_m}, \tag{18}$$

which is a weighted sum with the respective N_s solvent particles with velocities $\vec{v}_{s,i}$ in the cell. A stochastic rotation just like in (3) is then performed on the relative velocities of both the solvent particles and the embedded monomers. This results in an exchange of momentum and energy between all particles within a collision cell. The updated monomer velocities are then used as initial conditions for the subsequent Verlet time step. Since $\delta t < h$ the molecular dynamics time step is performed $\frac{h}{\delta t}$ times between consecutive MPCD collision. This can be seen as the free flow of the MPCD fluid during a streaming step. The combined collision step conserves both energy and momentum locally, i.e., cell-wise for the complex fluid. The proof for the pure solvent in (6) can be generalised by replacing the total momentum and energy of a cell $\vec{P}_{\text{cell}}(t) = N_s^c m_s \vec{v}_{\text{c.m.}}$ and $E_{\text{cell}}(t) = \frac{1}{2}\sum_{i\in\text{cell}} m_s \vec{v}_{s,i}^2(t)$ by $\vec{P}_{\text{cell}}(t) = (N_s^c m_s + N_m^c m_m)\vec{v}_{\text{c.m.}}$ and $E_{\text{cell}}(t) = \frac{1}{2}\sum_{i\in\text{cell}} m_s \vec{v}_{s,i}^2(t) + \frac{1}{2}\sum_{j\in\text{cell}} m_m \vec{v}_{m,j}^2(t)$ and applying the analogue calculations to the polymer contributions. The transport of momentum by fluid particles and its local conservation yield effective long-range HI between embedded objects.

Gompper et al. [14] noted that the average number of monomers per collision cell should be smaller than unity in order to properly resolve HI between them. The bond length of polymer chains should be of order of the cell size a_c such that monomers are close enough to display effects due to HI but far enough apart to avoid multiple monomers within a cell. Furthermore, Ripoll et al. [10] demonstrated that the mass ratio $\frac{m_m}{m_s}$ should equal the average number of solvent particles per cell ρ (assuming there is only one monomer per cell). Under this condition the monomer collides with a piece of solvent with equal mass so that the mutual momentum exchange is balanced. For $m_m \gg \rho m_s$ the polymer is barely affected by the solvent, whereas for $m_m \ll \rho m_s$ the monomers are kicked around violently. With this method of coupling there is no repulsion between fluid particles and embedded objects, both taken to be point particles. The latter have no excluded volume when coupled to the solvent, i.e., fluid particles can come arbitrarily close to their positions.

It is important to note that in non-equilibrium systems, e.g., under shear flow, the thermostat necessary for regulating the system's temperature does not act on the momenta of the monomers. The thermostat described in the previous section only rescales the fluid particles' velocities, but it fixes the average kinetic energy of the monomers, too. Solvent and polymer equilibrate to the same collective temperature via energy exchange during collisions. In the simulations the solvent has a much higher total energy compared to the embedded polymer, it acts as a heat reservoir and adjusts the monomers' temperature.

2.5 Random MPCD without Hydrodynamic Interactions

The coupling of the monomer momenta to the MPCD fluid establishes hydrodynamic interactions. In order to study their specific effects on the system's dynamics the same simulations have to be performed with and without HI. An alternative concept of simulating the solvent and/or the interaction with the monomer has to be found, that differs as little as possible from the original conditions except for the presence of HI. Ripoll et al. introduced a method to switch off HI in a MPCD algorithm [13]. They suggest that the positions of the solvent particles do not feature in the collision step (3) and therefore, no explicit particles have to be considered at all. Instead, every monomer is coupled with an effective solvent momentum $\vec{P}$ that is chosen directly from a Maxwell-Boltzmann distribution of variance $m_s\rho k_B T$ and zero mean. A center-of-mass velocity is assigned to every monomer velocity $\vec{v}_{m,i}$ given by:

$$\vec{v}_{c.m.,i} = \frac{m_m \vec{v}_{m,i} + \vec{P}}{m_m + m_s\rho}, \tag{19}$$

with which the collision step is performed. The rotation angle stays the same and like before, the interaction is executed after every collision time h. The algorithm has similar properties to MPCD, but it does not feature HI because there are no particles carrying momentum from one monomer to another. In the following this heat bath will be referred to as random MPCD solvent. Compared to the original algorithm its numerical effort is much smaller since it spares the calculation of trajectories and rotations of $\rho L_x L_y L_z$ particles. With this definition the variance $m_s\rho k_B T$ of the random solvent's momentum corresponds to a collision partner with a mass $m_s\rho$ or equivalently ρ colliding fluid particles. In contrast, the number of particles in a collision cell is Poisson distributed for the MPCD solvent. That is why in this thesis a random particle number $N_{c,P}$ is picked from a Poisson distribution which then determines the variance $m_s N_{c,P} k_B T$ of the Maxwell-Boltzmann distribution that yields random solvent momenta. This corresponds to a Poisson distributed number of colliding fluid particles and minimizes differences to particle-based MPCD. Shear flow is added to the random solvent by setting the mean of $\vec{P}$ from zero to $\left(m_s N_{c,P}\dot{\gamma} r_y^i, 0, 0\right)$, where the monomer's position in gradient direction r_y^i determines the local shear velocity in flow direction.

3 Fully Flexible Ring Polymers

In the following the molecular dynamics techniques used to simulate polymers are presented with a main focus on the implementation of unknotted fully flexible rings suspended in a dilute solvent. A Verlet integration scheme is introduced which governs the translational dynamics of point particles. The gyration tensor and the relaxation time measured by means of end-to-end correlations are specified. The effects of the interplay of shear flow, hydrodynamic interactions and polymer architecture on the topological conformations of flexible ring polymers are discussed.

3.1 Bead Model of Polymer Chains

Polymer molecules are composed of a large number of repeating subunits called monomers. The detailed structure of the latter can be arbitrarily complex and is not necessary to account for generic features of the polymer [14], such as their conformations under shear flow. The polymers simulated in this thesis are modelled as N_m point particles with mass m_m and continuous variables $\vec{r}_{m,i}$, $\vec{v}_{m,i}$ for their positions and velocities respectively. From here on the index m is omitted for all variables except for N_m and m_m since the solvent variables will not occur in any further calculations so that no ambiguities are caused. The point particles are referred to as beads and are interpreted as either single monomers of the polymer or as effective particles representing multiple monomers. A phenomenological model with potential $U(\{\vec{r}_i(t)\})$ is necessary to cover all the physics important on the length scale of the bead size σ and determine the dynamics of the beads. $U(\{\vec{r}_i(t)\})$ has to be considered as an effective description of the microscopic interactions since the beads are a coarse-grained description of the polymer's structure. The beads act as classical particles and their time evolution is governed by Newton's equations of motion, i.e., there is a force $\vec{F}_i$ acting on each bead i resulting from the interaction with the others. $\vec{F}_i$ is the gradient of the effective potential U applied. The particles are subject to a pair-wise Weeks-Chandler-Andersen (WCA) potential [29, 31],

$$U_{\mathrm{WCA}}(r_{ij}) = 4\epsilon \left[\left(\frac{\sigma}{r_{ij}} \right)^{12} - \left(\frac{\sigma}{r_{ij}} \right)^{6} + \frac{1}{4} \right] \Theta\left(r_{\mathrm{cutoff}} - r_{ij} \right), \tag{20}$$

that adds a soft repulsion between two beads i and j at distance $r_{ij} = |\vec{r}_i - \vec{r}_j|$ and en excluded volume around the monomers. The potential has a cutoff distance at $r_{\mathrm{cutoff}} = \sqrt[6]{2}\sigma$, such that $U_{\mathrm{WCA}}(r_{\mathrm{cutoff}}) = 0$ and $U_{\mathrm{WCA}}(r) \geq 0 \ \forall r > 0$. The parameters ϵ and σ define energy and length scales of the polymer and throughout this thesis they are set to $\epsilon = k_B T = 1$ and $\sigma = a_c = 1$. The beads can be attached to others and form chains when adding a pair-wise attractive potential. A FENE (finitely extensible nonlinear elastic) term acts as a nonlinear spring and is given by

$$U_{\mathrm{FENE}}(r_{ij}) = -\frac{k_{\mathrm{FENE}}R_0^2}{2}\ln\left[1-\left(\frac{r_{ij}}{R_0}\right)^2\right], \tag{21}$$

where k_{FENE} determines the strength of attraction and R_0 sets the maximal extent of the spring [29, 31]. The combination of potentials (20) and (21) acting on a pair of beads results in an effective bonding potential, see Fig. 8a, where the curves have been plotted for $k_{\mathrm{FENE}} = 30k_BT$ and $R_0 = 1.5\sigma$. As before, lengths are given in terms of the cell size a_c, and energies as multiples of $\beta^{-1} = k_BT$. With the choice of parameters a pair of beads linked with the FENE potential minimizes their bonding energy at a distance $r = 0.96\sigma$, see Fig. 8b, which is actually smaller than the size of a particle $\sqrt[6]{2}\sigma$ defined by the WCA potential.

To construct a fully flexible polymer chain point particles i interact with their respective next neighbours $i-1$ and $i+1$ via FENE while the WCA potential acts on all pairs ij keeping two beads from collapsing into each other. In this manner different polymer architectures can be realised. The simplest geometry is a linear chain with open ends, i.e., beads $i = 1$ and $i = N_m$ are connected to only one neighbour instead of two and $U_{\mathrm{FENE}}(r_{ij}) = -\frac{k_{\mathrm{FENE}}R_0^2}{2}\ln\left[1-\left(\frac{r_{ij}}{R_0}\right)^2\right](\delta_{i,j-1}+\delta_{i,j+1})$. If the FENE additionally acts on the pair of beads $i = 1$ and $i = N_m$, the ends are glued together and a ring polymer is simulated. Another possible type of architecture are star polymers which are composed of multiple linear chains. A central bead is connected to one of two tails of the strings via FENE springs which results in a star like shape. Each linear chain joined with the central bead corresponds to a branch of the star polymer.

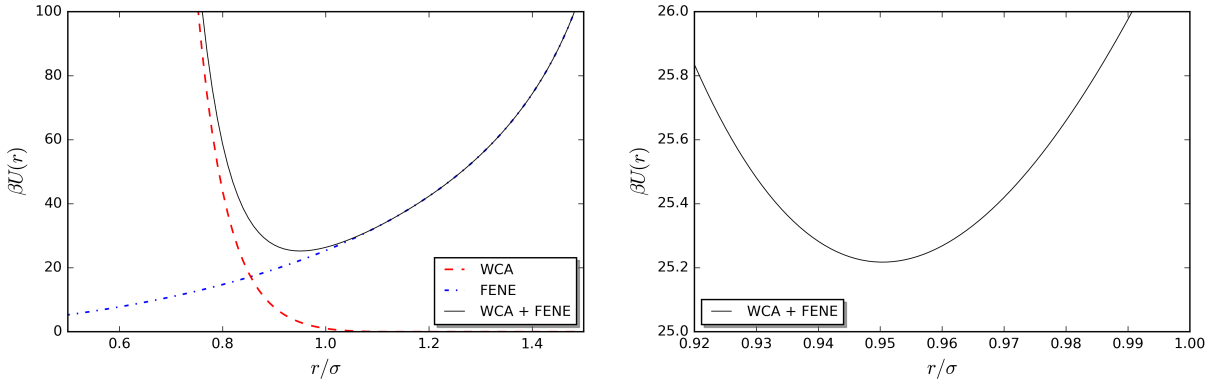

(a) (b)

Figure 8: (a) Repulsive WCA potential, attractive FENE potential and their sum as functions of bead-bead distance r. (b) Minimum of combined potential.

3.2 Velocity Verlet Algorithm

In the previous section the polymer system has been linked to a classical description of point particles whose time evolution is governed by a set of differential equations, $\vec{F}_i/m_m = \dot{\vec{v}}_i$ and $\vec{v}_i = \dot{\vec{r}}_i$ for $i = 1, ..., N_p$. A general exact solution is arbitrarily hard to find and might not even exist as an analytical expression. For the implementation in a computer simulation the equations of motion can be solved approximately by means of finite-difference methods. If the positions and velocities of all particles are known at a certain point of time t, all forces acting can be calculated as functions of $\vec{r}_i$ and $\vec{v}_i$. The idea is then to obtain positions and velocities at a later point in time $t+\delta t$ to a certain degree of accuracy. Time is thereby discretised into small intervals δt and Newton's equations are integrated stepwise. The procedure used for the molecular dynamics in this thesis is the velocity Verlet algorithm, following the description in [43, Ch. 3.2, p. 97-106]. The system evolves in time by alternately updating the velocities according to the forces acting on the beads, the positions according to the velocities, and the forces according to the positions:

$$\begin{aligned}
\vec{v}_i\left(t+\frac{\delta t}{2}\right) &= \vec{v}_i(t) + \frac{\delta t}{2}\frac{\vec{F}_i(t)}{m_m} \\
\vec{r}_i(t+\delta t) &= \vec{r}_i(t) + \delta t \vec{v}_i\left(t+\frac{\delta t}{2}\right) \\
\vec{F}_i(t+\delta t) &\equiv \vec{F}_i(\{\vec{r}_j(t+\delta t)\}) = -\vec{\nabla}_{\vec{r}_i} U_{\text{total}}(\{\vec{r}_j(t+\delta t)\}) \\
\vec{v}_i(t+\delta t) &= \vec{v}_i\left(t+\frac{\delta t}{2}\right) + \frac{\delta t}{2}\frac{\vec{F}_i(t+\delta t)}{m_m}.
\end{aligned} \tag{22}$$

The four calculations comprise one full Verlet / MD time step that is performed for all monomer particles. During the third one the force on particle i is evaluated as gradient with respect to position $\vec{r}_i$ of the total potential U_{total} which depends on the positions $\{\vec{r}_j(t+\delta t)\}$ at time $t+\delta t$. At the end of (22) quantities like the energy etc. can be calculated. The MD time step δt is picked to be $\delta t = \frac{1}{100}h$ in order to properly resolve the fast molecular dynamics between collisions with the solvent. This is equivalent to 100 Verlet steps being performed in between consecutive MPCD steps.

3.3 Ring Polymers in Dilute Solutions

The polymers simulated in this thesis are ring shaped. They are embedded as single objects in a dilute solution, i.e., there is only one polymer per simulation. In every Verlet step, a monomer i interacts with its two chain neighbours by means of the FENE potential as well as the WCA potential. The evaluation of the corresponding forces requires the calculation of their

relative distances $\vec{r}_{i,i+1}$ and $\vec{r}_{i,i-1}$. The numerical effort of the calculation of all chain neighbour interactions scales with the number of monomers N_m. In addition, i interacts via the WCA potential with all non chain neighbour monomers $j \neq i+1, i-1$ if i and j lie within the cutoff distance r_{cutoff}. The evaluation of all possible monomer pairs scales with N_m^2. For many of them $|\vec{r}_{ij}| = r_{ij} > r_{\mathrm{cutoff}}$, i.e. the resulting repulsive force is zero and hence, the computation of $\vec{r}_{ij}$ is in vain. In order to minimize the numerical effort, it is constructive to avoid unnecessary calculations of $\vec{r}_{ij}$ as much as possible by using Verlet neighbour lists as explained in [43, Ch. 5.3, p. 193-200]. If at a given time t two monomers are further apart than $r_{nl} > r_{\mathrm{cutoff}}$, they are very unlikely to be closer than the potential cutoff within the next few Verlet steps. r_{nl} is picked to be $1.5 r_{\mathrm{cutoff}}$ so that the particles' mean free path $\sim \delta t$ is small in comparison. It is then sufficient to check every f-th MD step ($f = 20$ here) whether non chain neighbours lie within a distance r_{nl} and store this information in a list. The decision whether $\vec{r}_{ij}$ is to be computed during step 3 of the velocity Verlet procedure is made according to this list.

The constituents of the ring polymer are jointed together by the combined potential in contrast to the MPCD solvent particles. Their position variables do not need to be confined within a simulation box with periodic boundary conditions per se. However, when the monomers' momenta are coupled to the MPCD collision, their positions must be held within the box's boundaries to be sorted into one of the collision cells. Applying periodic boundary conditions to monomers is fine as long as $\dot{\gamma} = 0$. On the contrary, applying Lees-Edwards boundary conditions to them is problematic. Lees-Edwards boundary conditions are supposed to generate a shear gradient of the solvent momenta which consequently has an effect on the polymer's dynamics during collision. A boost added to the velocity of a boundary crossing monomer is an artificial effect on its dynamics and should not be performed. To avoid any issues with the system's physics, the monomers' boundary conditions are replaced by shifts back to the direction of the simulation box's center. If an embedded particle leaves the box in direction i, all particles of both the solvent and the polymer are translated along i in such a way that all monomers lie within the simulation box again. The shifting procedure is guaranteed to be successful if it repositions the crossing monomer as close to the respective boundary as the polymer's furthest extent in the opposite direction, see Fig. 9, and additionally, if the simulation box's dimensions are big enough to encapsulate all monomers in all directions.

The conformations of polymers under shear are investigated and quantified by measuring the ring's gyration tensor

$$G_{\alpha\beta} = \frac{1}{N_m} \sum_{i=1}^{N_m} \langle \overline{r}_{i,\alpha} \overline{r}_{i,\beta} \rangle, \tag{23}$$

where $\overline{r}_{i,\alpha} = (\vec{r}_i - \vec{r}_{\mathrm{c.m.}})_\alpha$ is the α-coordinate of i-th monomer's position relative to the polymer's

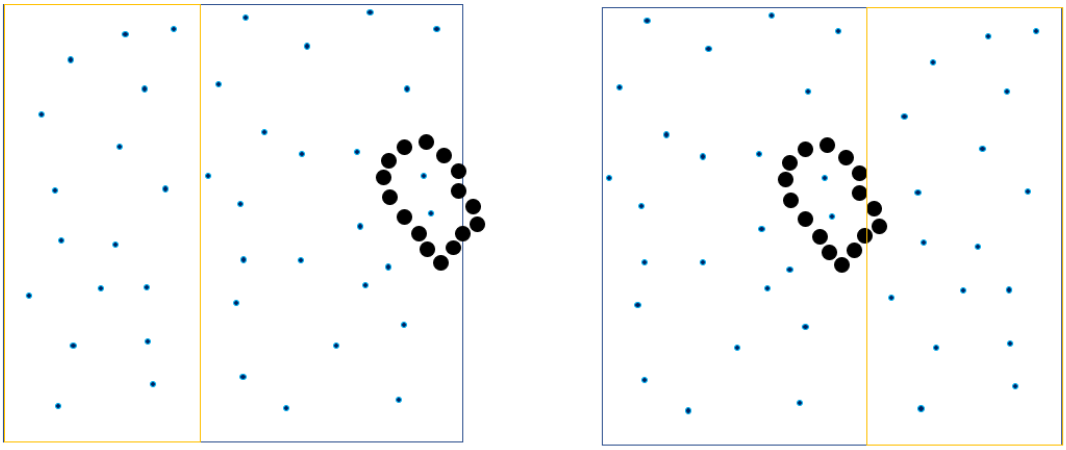

Figure 9: Monomers and solvent particles in simulation box before (left) and after (right) a system shift. The blue dots indicate the MPCD fluid and the black ones represent the ring polymer. The directions of the box are arbitrary. When monomers cross the boundary of the simulation box, the entire system is shifted so that afterwards, the polymer's geometric center coincides with the center of the simulation box in the direction of shifting. The solvent particles within the area outlined in yellow thereby leave the simulation box and become subject to Lees-Edwards boundary conditions if the shift is conducted in flow direction and to boundary conditions otherwise.

center-of-mass $\vec{r}_{\mathrm{c.m.}}$ and the brackets $\langle ... \rangle$ denote averaging over time. The diagonal elements $G_{\alpha\alpha}$ reflect the elongation of the polymer in the α-coordinate. The radius of gyration R_g is defined via the tensor's trace $R_g^2 = \mathrm{tr}[\mathrm{G}_{\alpha\beta}]$ and is a measure for the polymer's general extension. By definition it equals the sum over the three eigenvalues of $G_{\alpha\beta}$.

The ring polymers simulated are set up as an open circle plane in the flow-vorticity plane. This conformation is not stable and over time the ring becomes a self-avoiding coil if no shear is applied with $G_{xx}(0) = G_{yy}(0) = G_{zz}(0) = R_g^2(0)/3$. The time averaged extension of this stationary state is denoted as $R_g^2(0)$ and is used as reference value when investigating the ring conformations under shear as $R_g^2(\dot{\gamma})/R_g^2(0)$ for $\dot{\gamma} > 0$. $R_g^2(0)$ and other equilibrium properties of a polymer are not affected by HI [14]. For a ring of length $N_m = 100$ it is found to be $R_g^2(0)/\sigma^2 = 28.95(4.00)$ in simulations. When investigating quantities $f(\dot{\gamma})$, it is important to rescale the argument $\dot{\gamma}$ to the dimensionless Weissenberg number $\mathrm{Wi} = \tau_R \dot{\gamma}$, where τ_R is the solvent fluid's relaxation time. It differs for varying system parameters, e.g., the number of monomers N_m, the polymer's architecture, and whether there is HI (particle-based MPCD) or not (random MPCD). Motivated by [44], the relaxation time is computed by means of the end-to-end correlation function

$$C_{ee}(t) = \frac{\langle \vec{R}_{ee}(t) \vec{R}_{ee}(0) \rangle}{\langle \vec{R}_{ee}(0)^2 \rangle}, \tag{24}$$

where $\vec{R}_{ee}(t)$ defines a vector joining two monomers of the chain that are separated by $N_m/2$ monomers and $\langle ... \rangle$ represents an average over the $N_m/2$ end-to-end connections. Fig. 10 depicts the end-to-end correlation as a function of time for a ring polymer of length $N_p = 100$ with mass $m_m = 10m_s$, and parameters $R_0 = 1.6\sigma$, $k_{\mathrm{FENE}} = 30\frac{\epsilon}{\sigma^2}$. Fig. 10a shows plots of multiple simulation runs with HI active and 10b the analogue curves without HI. The curves fit an exponential decay and the relaxation times for separate runs are obtained by a best fit of $C_{ee}^{\mathrm{run}}(t) = \exp(-t/\tau_R)$. The values are used to calculate an average relaxation time that has a large statistical error of over 33%. To reduce the statistical blur, the correlation functions of time are first added together to an average $1/N_{\mathrm{runs}} \sum_{N_{\mathrm{runs}}} C_{ee}^{\mathrm{run}}(t)$, see Fig. 10c and 10d, and the statistical error is the deviation of the fit from the theoretical exponential curve $\exp(-t/\tau_R)$. The relaxation time obtained $\tau_R(+\mathrm{HI}) \approx 3413(6) \cdot \tau_{\mathrm{MPCD}}$ using the MPCD solvent with HI is, as expected, notably shorter than the respective value for the random MPCD

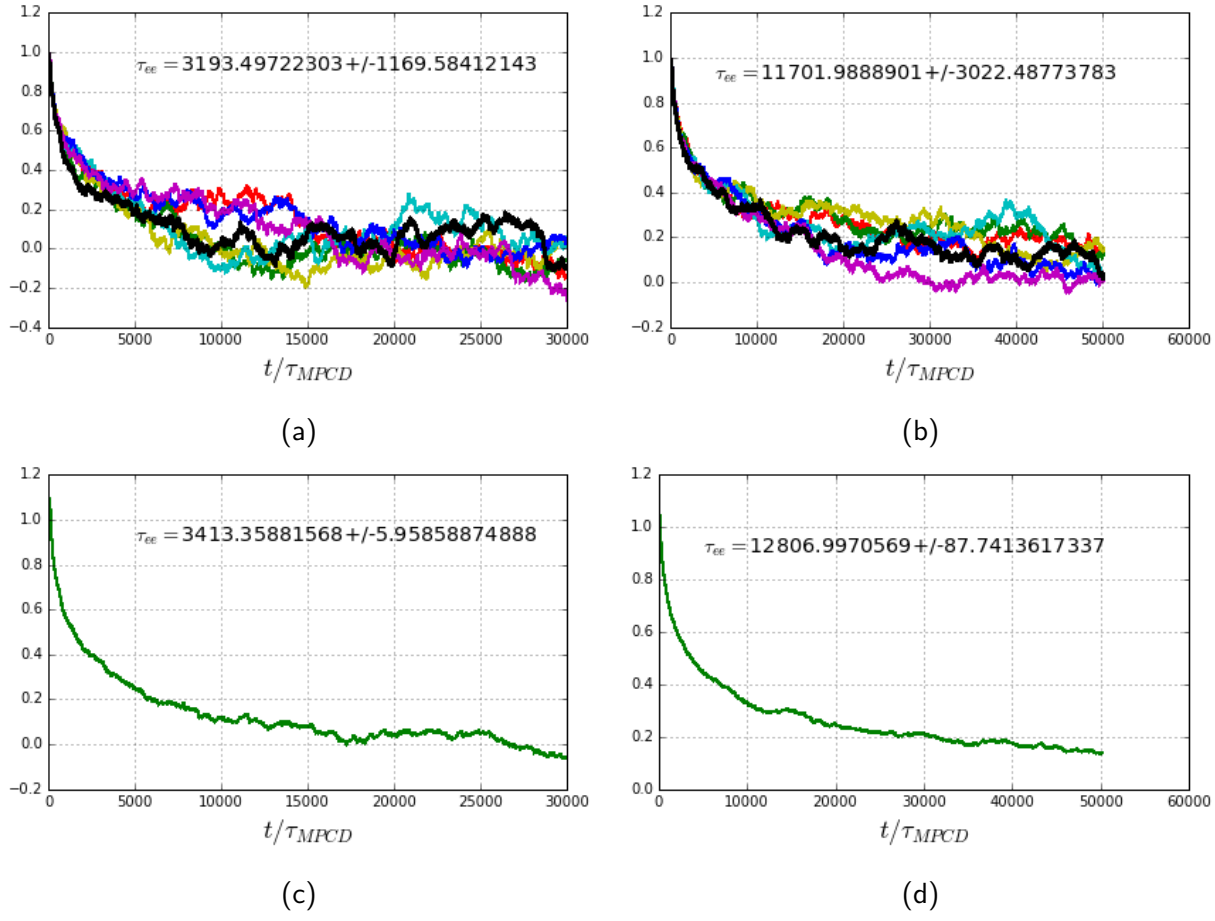

Figure 10: End-to-end correlation as a function of time for a ring polymer of length $N_p = 100$ with mass $m_m = 10m_s$, and parameters $R_0 = 1.6\sigma$, $k_{\mathrm{FENE}} = 30\frac{\epsilon}{\sigma^2}$ with HI active. The inserted values give the computed relaxation times with statistical error. Their accuracy is highly exaggerated by the calculation program. Curves of multiple relaxation runs with HI (a) and without HI (b) averaged to (c) and (d), respectively.

method without HI: $\tau_R(-\mathrm{HI}) \approx 12806(88) \cdot \tau_{\mathrm{MPCD}}$. For comparison, one can calculate theoretical values for the relaxation time of an ideal chain with the Rouse model for a solvent without HI, and with the Zimm model for a solvent with HI [45]. The former predicts a Rouse time of $\tau_R \approx \eta_S (k_B T)^{-1} N_m \sigma R_g^2(0) = 7.3 \cdot 10^5$ where the solvent's dynamic viscosity $\eta_S = \rho_S \nu_{\mathrm{GK}}$ is approximated by (10) and the latter calculates a Zimm time of $\tau_Z \approx \eta_S (k_B T)^{-1} R_g^3(0) = 2.1 \cdot 10^5$. Both approaches give much higher relaxation times than the ones measured for the fully flexible ring polymers which implies that the addition of excluded volume to an ideal chain dramatically reduces the value of τ_R.

3.4 Ring Inflation under Shear Flow

To check for the effects that shear flow and HI have on the ring conformations simulations of a single unknotted fully flexible polymer ring with length $N_m = 100$ are performed for Weissenberg numbers in the range $[10^0 ... 10^3]$. Both the MPCD solvent with HI and the random solvent without HI are used separately, where the former simulation method uses Lees-Edwards boundary conditions and a thermostat in a box of size $80a_c \times 40a_c \times 40a_c$. Fig. 11 shows the elongation of the ring as function of Wi. The diagonal components of the gyration tensor, see Fig. 11a-c, are normalised by $R_g^2(0)/3$ and the squared radius of gyration, see Fig. 11d, by $R_g^2(0)$. The values are obtained by averaging over the last $2 \cdot 10^7$ of $5 \cdot 10^7$ Verlet steps so that the system has enough time to reach thermal equilibrium after multiple relaxation times. Ten individual ensembles runs are performed with different sequences of random numbers generated and the ultimate value results as the mean of the ten time averages.

Without the presence of HI (red curves) the ring elongates in flow direction with growing shear rate while it is contracted in gradient and vorticity directions, see Fig. 11. Under shear flow the ring undergoes tumbling motions which means that the polymer experiences strong fluctuations on the monomer scale. On the macroscale it continuously switches between shrinking and stretching, from a self-avoiding coil to being elongated along flow direction [46]. Tumbling under shear flow is known to occur for other polymer architectures suspended in a MPCD solvent, i.e., linear [30, 29], star [25], dendritic [24], cross-linked [21]. Their gyration tensor have been shown to demonstrate the same monotonic behaviour under shear flow as the ring when HI is deactivated.

In contrast, the ring polymer shows a different behaviour under shear when HI is activated by using the particle based MPCD solvent. It grows in flow direction up to Weissenberg numbers of $\sim 4 \cdot 10^2$ and decreases then again for higher shear rates. At its peak G_{xx} has a higher value when HI is active compared to when it is absent, Fig. 11a. This is an indication that the presence of HI suppresses tumbling for shear rates in the vicinity of the maximum at $\mathrm{Wi} \sim 3 \cdot 10^2$ which leads to higher time and ensemble averages of the gyration tensor. Furthermore, in vorticity direction G_{zz} decreases slightly for shear rates up to $\mathrm{Wi} \sim 4 \cdot 10^1$ but increases then up to a maximum at

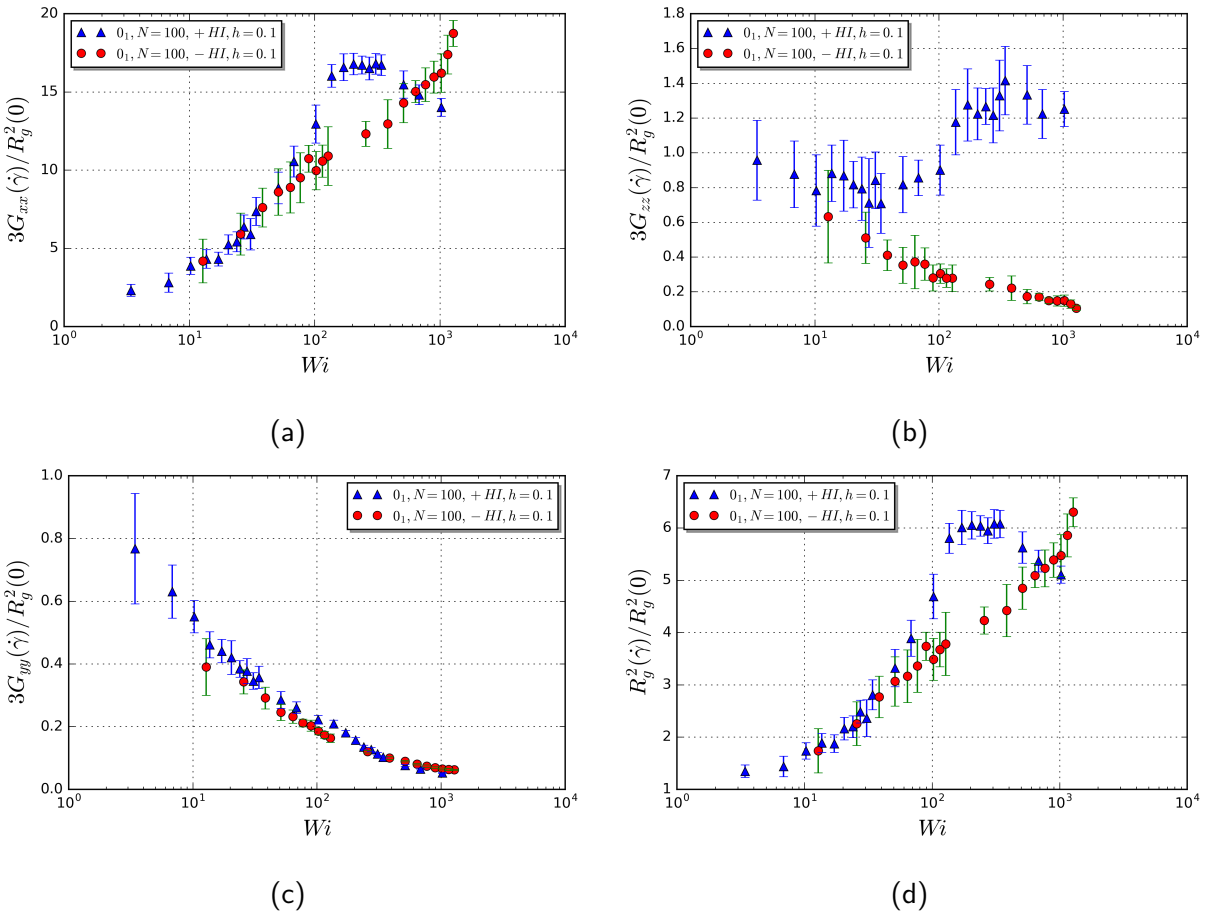

Figure 11: Components of the gyration tensor in (a) flow-, (b) vorticity-, and (c) gradient-direction of a ring of length $N_m = 100$ as functions of the Weissenberg number. The trace gives the squared radius of gyration (d). All plots are normalized to the equilibrium value $R_g^2(0)$.

$\mathrm{Wi} \sim 4 \cdot 10^2$ before decreasing again. What is more, the component G_{yy}^2 in gradient direction also shows a non-monotonic behaviour around the onset of the inflationary phase beginning at $\mathrm{Wi} \sim 10^2$ featuring a local minimum followed by a local maximum. For higher shear rates tumbling motion resumes and all components $G_{\alpha\alpha}$ decrease with Wi. These results agree with the findings of Liebetreu and Likos [30, 29] who described a transition to rigid non-Brownian particles and an inflationary phase of ring polymers under shear flow in a dilute MPCD solvent. According to them the non-monotonic behaviour of $G_{\alpha\alpha}$ demonstrates the swelling in vorticity direction and the self-stabilization of the ring due to the backflow transmitted by HI. In the inflated state the polymer is fully stretched and unfolded which suppresses tumbling motion. Under this condition the horseshoe regions of the swollen ring are locked in place relative to the center-of-mass. Fig. 12 presents snapshots of single ring polymers under free flow, i.e., $\dot{\gamma} = 0$ (left side) and under shear flow of $\mathrm{Wi} = 4 \cdot 10^2$ (right side), all of them on the flow-vorticity plane. The presence of HI has little effect on the equilibrium properties for $\dot{\gamma} = 0$ and it shrinks down to a steady extension $R_g^2(0)$. When shear flow is imposed on the system and HI is active

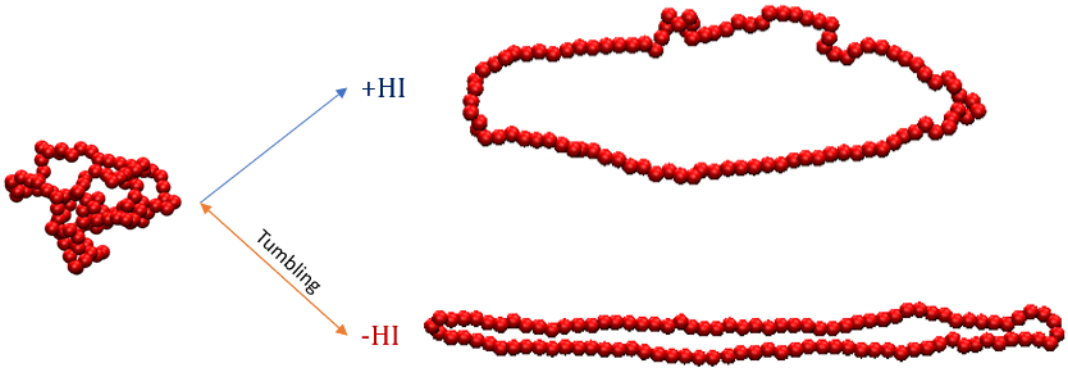

Figure 12: Snapshots of ring polymers with $N_m = 100$ under no shear in a steady conformation for $(\mathrm{Wi} = 0)$ (left) and under shear $(\mathrm{Wi} = 4 \cdot 10^2)$ in the rigid inflationary phase (top right) with HI active and in an elongated conformation (bottom right) with HI inactive. The latter is prone to tumbling motions between the stretched and the coiled conformations.

the ring is in a steady conformation and stretched in all directions. In contrast, if HI is absent the ring undergoes tumbling motions between being stretched out along flow direction and being coiled together.

Liebetreu and Likos [30, 29] conducted the same simulation for a range of polymers with different topologies and sizes. They demonstrated that the non-monotonic behaviour of $G_{\alpha\alpha}$ is even more pronounced for larger N_m, especially the cusp in G_{yy} which they interpreted as the ring beginning to swell to its stretched rigid conformation. The same notion of inflation under shear was observed for knotted rings with up to eight crossings. Knotted regions are pulled tight and stay localized during inflation. Therefore, under strong shear, knotted rings with a higher contour length behaved like unknotted ones. The inflation phase was found to be missing in the absence of HI and it was concluded that the inflation phase is a unique feature of ring polymers that results from interplay between the ring topology and HI. The MPCD solvent reproduces HI in a way that enables the occurrence of inflation at moderate Weissenberg numbers independently of the box dimensions. The hydrodynamic flow profile of the MPCD particles around fully inflated ring polymers has been plotted in [30, 29] for the respective shear rates where stretching is most pronounced. In the flow-vorticity plane it is characterized by backflow from the horseshoe regions in flow direction that makes the ring swell in vorticity direction. There is a slight gradient-directed drift around the horseshoe regions that gives the stretched ring a tilt into flow-gradient plane and causes the local maximum of G_{yy}. In this flow regime backflow causes enough tension along the ring so that thermal fluctuations are suppressed.

Similar results were found by Hsiao et al. [47] who used a different techniques to account for HI and shear flow, albeit at lower Weissenberg numbers of $\mathrm{Wi} \leq 10$. In their simulations of dilute ring polymers the monomer dynamics follow a Langevin equation that neglects inertial effects, i.e., $m_m \ddot{\vec{r}}_i = 0$:

$$\frac{\partial \vec{r}_i}{\partial t} = \Gamma \cdot (\vec{r}_i - \vec{r}_{\mathrm{com}}) - \sum_j \mu_{ij} \nabla_{\vec{r}_j} U + \vec{\xi}_i(t), \tag{25}$$

where Brownian motion is realised with a stochastic noise term $\vec{\xi}_i$. HI was added to the system by coupling the conservative forces to a Rotne-Prager-Yamakawa (RPY) mobility tensor μ_{ij} without the need of a particle-based solvent. HI was switched off by replacing the RPY tensor with a unitary matrix. The matrix Γ describes the applied planar elongational flow profile. Analogously to the MPCD solvent with and without HI, they found that the components $G_{\alpha\alpha}$ show monotonic behaviour if HI is switched off just like for the random MPCD solvent. When the RPY tensor was used the same non-monotonic behaviour occurred for G_{xx} and G_{zz}, but was not found in gradient direction. Young et al. [48] used the model (25) with the RPY tensor and imposed both a simple shear profile as well as mixed shear profiles with the gradient direction being rotated by an angle $\alpha > 0$. Inflation and suppression of tumbling only occurred for $\alpha > 0$ and they concluded that the gradient component of backflow is important for the emergence of an inflatory phase.

4 Supercoiled Ring Polymers

The model of ring polymers whose bonds are formed by the interplay of attractive FENE and repulsive WCA potentials is expanded by torsional and bending constraints which give rise to a description of supercoiled polymers. The monomers are endowed with set of patches which quantify its orientation and are a tool for defining the potentials added. Two different ways of modelling the rigid bodies (bead + patches) are presented and discussed. The emerging integration schemes for the rotational dynamics are explained for both rigid body models before going on to the mathematical representation of monomer orientations and their time evolution by means of quaternions. Writhe and twist are defined to further quantify and analyse the ring conformations. Finally, the initialization process of supercoiled rings is explained in detail and the equilibrium state for different parameters is discussed by analyzing the quantities measured during simulations.

4.1 Torsional and Bending Constraints

The ring polymer simulated as described in the previous section models the intramolecular forces so that they depend solely on the pairwise distance of two monomers. To obtain a simulation that depicts DNA more accurately this model is replaced by a twistable worm-like chain. Motivated by Smrek et al. [31] the bead potentials (20) and (21) are augmented by additional energy terms to define the DNA's bending stiffness over the scale of multiple chain bonds as well as torsional stiffness between chain neighbours. To quantify bending an energy penalty is introduced between consecutive triplets of chain neighbours $\vec{r}_{i-1}$, $\vec{r}_i$, and $\vec{r}_{i+1}$:

$$U_{\mathrm{bend}}(\theta_b) = k_{\mathrm{bend}}\left(1-\cos(\theta_b)\right),\ \cos(\theta_b) = \frac{\vec{r}_{i-1,i}\cdot\vec{r}_{i,i+1}}{|\vec{r}_{i-1,i}||\vec{r}_{i,i+1}|}, \tag{26}$$

where θ_b is the angle formed by two adjacent bonds $\vec{r}_{i-1,i}$ and $\vec{r}_{i,i+1}$, see Fig. 14a. The bending constant is picked to be $k_{\mathrm{bend}} = 20k_BT$ so that the ring has a persistence length $l_p = 20\sigma$. The scale of the monomer diameter should be mapped to DNA's thickness in real units of $\sigma = 2.5\mathrm{nm}$, i.e., $2.5/0.34 = 7.35$ bp per bead and $l_p = 150$ bp $= 50\mathrm{nm}$ [31].

To quantify twists of the DNA chain around its own axis along the polymer backbone the monomers need to possess more information about their orientation in space. Every bead point particle is therefore equipped with three patches which remain at a fixed distance $l_{\mathrm{pat}} = r_{\mathrm{cutoff}}/2 = \frac{\sqrt[6]{2}\sigma}{2}$. The vectors $\vec{r}_{\mathrm{pat},i,k}$ are defined as the vectors going from the position of bead i to its k-th patch where $k = 1,2,3$ so that each triplet $\{\vec{r}_{\mathrm{pat},i,k}\}_{k=1,2,3}$ forms an orthogonal basis with the respective bead position $\vec{r}_i$ as the origin. Fig. 13 shows a short segment of a polymer chain with patches where colours blue, red, and green correspond to the numeration $k = 1,2,3$.

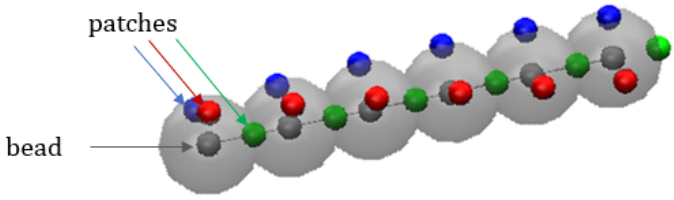

Figure 13: Depiction of six patched monomers. The grey surface indicates the extension of the monomer's rigid body with radius l_{pat}. The bead positions are the grey centers and the three patches are fixed on the surface.

The blue and red patches are used to introduce two dihedral CHARMM springs that constrain the torsional angle Ψ between consecutive beads to a fixed value Ψ_0. Ψ is defined as the angle between the planes with normal vectors $\vec{r}_{i,i+1} \times \vec{r}_{\mathrm{pat},i,b/r}$ and $\vec{r}_{i,i+1} \times \vec{r}_{\mathrm{pat},i+1,b/r}$. It is evaluated for the blue and red patches respectively, see Fig 14b. The corresponding potential is

$$\begin{aligned} U^{b/r}_{\mathrm{torsion}}(\Psi_{b/r}) &= k_{\mathrm{torsion}} \left(1 - \cos(\Psi_{b/r} - \Psi_0)\right) \\ &= k_{\mathrm{torsion}} \left(1 - \cos\Psi_0 \cos(\Psi_{b/r}) - \sin\Psi_0 \sin(\Psi_{b/r})\right), \end{aligned} \tag{27}$$

with the torsion constant $k_{\mathrm{torsion}} = 50 k_B T$. The equilibrium angle Ψ_0 determines the polymer chain's preferred supercoiling $\sigma_{\mathrm{sc}} = \Psi_0/2\pi$. To see the impact of the torsional constraint the simulations are also performed for nontorsionally constrained rings for which k_{torsion} is set to zero. These are referred to as 'relaxed' rings in the following and they are different to rings with $\sigma_{\mathrm{sc}} = 0$ and nonzero k_{torsion} which are torsionally constrained to a supercoiling of zero. The cosine and sine in (27) are computed as

$$\begin{aligned} \cos(\Psi_{b/r}) &= \frac{(\vec{r}_{i,i+1} \times \vec{r}_{\mathrm{pat},i,b/r}) \cdot (\vec{r}_{i,i+1} \times \vec{r}_{\mathrm{pat},i+1,b/r})}{|\vec{r}_{i,i+1} \times \vec{r}_{\mathrm{pat},i,b/r}||\vec{r}_{i,i+1} \times \vec{r}_{\mathrm{pat},i+1,b/r})|} \\ &= \frac{|\vec{r}_{i,i+1}|^2}{|\vec{r}_{i,i+1} \times \vec{r}_{\mathrm{pat},i,b/r}||\vec{r}_{i,i+1} \times \vec{r}_{\mathrm{pat},i+1,b/r}|} \cdot \\ &\left[(\vec{r}_{\mathrm{pat},i,b/r} \cdot \vec{r}_{\mathrm{pat},i+1,b/r}) - (\frac{\vec{r}_{i,i+1}}{|\vec{r}_{i,i+1}|} \cdot \vec{r}_{\mathrm{pat},i,b/r})(\frac{\vec{r}_{i,i+1}}{|\vec{r}_{i,i+1}|} \cdot \vec{r}_{\mathrm{pat},i+1,b/r})\right], \end{aligned} \tag{28}$$

$$\begin{aligned} \sin(\Psi_{b/r}) &= \frac{(\vec{r}_{i,i+1} \times \vec{r}_{\mathrm{pat},i,b/r}) \times (\vec{r}_{i,i+1} \times \vec{r}_{\mathrm{pat},i+1,b/r})}{|\vec{r}_{i,i+1} \times \vec{r}_{\mathrm{pat},i,b/r}||\vec{r}_{i,i+1} \times \vec{r}_{\mathrm{pat},i+1,b/r})|} \cdot \frac{\vec{r}_{i,i+1}}{|\vec{r}_{i,i+1}|} \\ &= \frac{|\vec{r}_{i,i+1}|}{|\vec{r}_{i,i+1} \times \vec{r}_{\mathrm{pat},i,b/r}||\vec{r}_{i,i+1} \times \vec{r}_{\mathrm{pat},i+1,b/r})|} \vec{r}_{i,i+1} \cdot (\vec{r}_{\mathrm{pat},i,b/r} \times \vec{r}_{\mathrm{pat},i+1,b/r}). \end{aligned} \tag{29}$$

A third potential aligns the patch reference systems so that the blue and red patches' positions relative to their bead is as perpendicular to the segments $\vec{r}_{i-1,i}$ and $\vec{r}_{i,i+1}$ as possible. The green patch $\vec{r}_{\mathrm{pat},i,g}$ is forced onto the segment line $\vec{r}_{i,i+1}$ by the alignment potential:

$$U_{\text{align}}(\theta_a) = k_{\text{align}}\left(1 - \cos(\theta_a)\right), \ \cos(\theta_a) = \frac{\vec{r}_{\text{pat},i,g}}{l_{pat}} \cdot \frac{\vec{r}_{i,i+1} - \vec{r}_{\text{pat},i,g}}{|\vec{r}_{i,i+1} - \vec{r}_{\text{pat},i,g}|}. \tag{30}$$

In this way, blue and red patches are aligned orthogonal to the polymer backbone consisting of the beads so that dihedral angles between consecutive beads can be formed properly, see Fig. 14c. The constant is picked to be $k_{\text{align}} = 200 k_B T$.

The WCA and FENE potential constants are increased to $k_{\text{FENE}} = 40 k_B T$ and $R_0 = 1.6\sigma$ so that they coincide with the ones chosen in [31]. Forces derived from all potentials presented act on the beads i whereas torsion (27) and alignment (30) also yield forces upon the respective patches k denoted by $\vec{F}_{\text{pat},i,k}$. Forces on the beads are calculated as $\vec{F}_i(t) = -\vec{\nabla}_{\vec{r}_i} U_{\text{total}}(\{\vec{r}_j(t)\}, \{\vec{r}_{\text{pat},j,k}(t)\})$. The patch forces are calculated as $\vec{F}_{\text{pat},i,k}(t) = -\vec{\nabla}_{\vec{r}_{\text{pat},i,k}} U_{\text{total}}(\{\vec{r}_j(t)\}, \{\vec{r}_{\text{pa}}$ $-\vec{\nabla}_{\vec{r}_{\text{pat},i,k}} U_{\text{pot}}(\{\vec{r}_j(t)\}, \{\vec{r}_{\text{pat},j,k}(t)\})$ with pot = torsion(blue/red), align. The total force on monomer i is computed as $\vec{F}_{\text{total},i}(t) = \vec{F}_i(t) + \sum_{k=1}^{3} \vec{F}_{\text{pat},i,k}(t)$ that is used as the force acting on the momenta in the velocity Verlet algorithm (22). The details about the computation of forces and potentials in dependence of bead and patch positions are described in Appendix B.

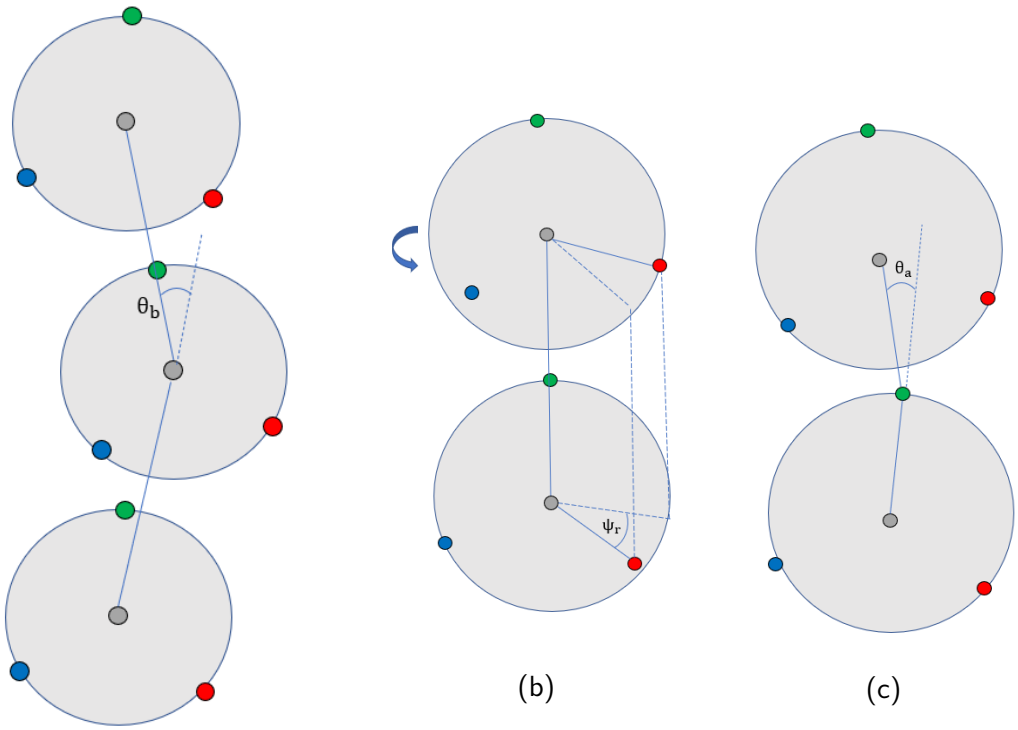

Figure 14: Sketching of potentials concerning (a) bending stiffness, (b) torsional stiffness, and (c) alignment along chain backbone. The red torsional angle is depicted as an example in (b); the blue patches form a dihedral system as well which is omitted here.

4.2 Patches with and without Mass

Adding patches to the beads effectively transforms the previous point particles i to rigid bodies with a rotational degree of freedom χ_i, angular velocity $\vec{\omega}_i$, inertia tensor $I_i^{\alpha\beta}$, and rotational energy $E_{rot,i} = \frac{1}{2}\vec{\omega}_i^{\mathrm{T}} I_i^{\alpha\beta}\vec{\omega}_i$. The explicit representation of χ_i with quaternions is discussed in section 4.4; in any case, χ_i carry information about the positions of the three patches $\vec{r}_{\mathrm{pat},i,k}$ relative to its bead $\vec{r}_i$.

The rigid body monomer can be modelled in two different ways that were presented by Brackley et al. [49]. In the following they are referred to as 'sphere' and '4m' model, respectively. The first implementation models the monomers as extended spheres with radius l_{pat} and continuous mass density $\frac{3m_m}{4\pi l_{\mathrm{pat}}^3}$, which corresponds to an inertia tensor $I_i^{\alpha\beta} = I_{\mathrm{sphere}}\delta_{\alpha,\beta}$ with the moment of inertia $I_{\mathrm{sphere}} = \frac{2}{5}m_m l_{\mathrm{pat}}^2$. The position of the bead $\vec{r}_i$ is the central point of the rigid body and coincides with center-of-mass of the monomer, whereas the patches mark positions on the sphere's surface. Therefore, only $\vec{F}_{\mathrm{pat},i,k}$ contribute to a total torque on monomer i of $\vec{T}_i = \sum_{k=1}^{3}\vec{r}_{\mathrm{pat},i,k}\times\vec{F}_{\mathrm{pat},i,k} = \frac{d}{dt}\vec{L}_i = \frac{d}{dt}\left(I_i^{\alpha\beta}\vec{\omega}_i\right) = I_{\mathrm{sphere}}\dot{\vec{\omega}}_i$. Rotations around the center-of-mass only affect the orientations χ_i but not the bead positions.

In the second approach, the total mass of a monomer m_m is distributed equally over the bead and three patches so that the rigid body consists of four point particles with mass $m_m/4$ in a fixed constellation. With this composition the center-of-mass does not coincide with the position of the bead but is rather $\vec{r}_{\mathrm{c.m.,i}} = \vec{r}_i + \frac{1}{4}\sum_{k=1}^{3}\vec{r}_{\mathrm{pat},i,k}$. A rotation around the center-of-mass therefore affects both the monomer orientation and the bead position. The point of reference when calculating $\vec{T}_i$ is no longer the bead position so that the patch positions have to be calculated relative to $\vec{r}_{\mathrm{c.m.},i} \neq \vec{r}_i$ and the force acting on the bead contributes to the torque in contrast to the sphere model: $\vec{T}_i = (\vec{r}_i - \vec{r}_{\mathrm{c.m.,i}})\times\vec{F}_i + \sum_{k=1}^{3}(\vec{r}_{\mathrm{pat},i,k} + \vec{r}_i - \vec{r}_{\mathrm{c.m.,i}})\times\vec{F}_{\mathrm{pat},i,k}$. Furthermore, because of the more complex structure the inertia tensor is not a multiple of unity and depends on χ_i which complicates the rotational dynamics $\vec{T}_i = \frac{d}{dt}\left(I_i^{\alpha\beta}\vec{\omega}_i\right) = \frac{d}{dt}\left(I_i^{\alpha\beta}\right)\vec{\omega}_i + I_i^{\alpha\beta}\frac{d}{dt}\vec{\omega}_i$. Since $I_i^{\alpha\beta}$ is symmetric it is diagonal in the reference system spanned by its eigenvectors. In this reference system the first term of $\vec{T}_i$ vanishes. The eigenvalues are $I_{4\mathrm{m}}^{11} = \frac{1}{2}m_m l_{\mathrm{pat}}^2$ and $I_{4\mathrm{m}}^{22} = I_{4\mathrm{m}}^{33} = \frac{5}{16}m_m l_{\mathrm{pat}}^2$ with corresponding normalised eigenvectors:

$$\begin{aligned}
\vec{\lambda}_{1,i}^{4\mathrm{m}} &= \frac{1}{\sqrt{3}\,l_{\mathrm{pat}}}\sum_{k=1}^{3}\vec{r}_{\mathrm{pat},i,k},\\
\vec{\lambda}_{2,i}^{4\mathrm{m}} &= \frac{1}{\sqrt{2}\,l_{\mathrm{pat}}}(\vec{r}_{\mathrm{pat},i,g} - \vec{r}_{\mathrm{pat},i,b}),\\
\vec{\lambda}_{3,i}^{4\mathrm{m}} &= \vec{\lambda}_{1,i}^{4\mathrm{m}}\times\vec{\lambda}_{2,i}^{4\mathrm{m}},
\end{aligned} \tag{31}$$

where $\vec{\lambda}_{2,i}^{4\mathrm{m}}$ and $\vec{\lambda}_{3,i}^{4\mathrm{m}}$ span a plane of eigenvectors corresponding to the degenerate $I_{4\mathrm{m}}^{11}$. For the calculation of $\dot{\vec{\omega}}_i$ by means of $\vec{T}_i = \frac{d}{dt}\left(I_i^{\alpha\beta}\vec{\omega}_i\right)$ the angular velocity $\vec{\omega}_i$ and the torque $\vec{T}_i$ have to be

represented in coordinates of the orthonormal basis of eigenvectors $\{\vec{\lambda}_i^{\alpha}\}_{\alpha}$. Then, the rotational dynamics is given by:

$$\begin{aligned}
\dot{\omega}_{i,1}^{\lambda} &= \frac{1}{I_{4\mathrm{m}}^{11}} T_{i,1}^{\lambda}, \\
\dot{\omega}_{i,2}^{\lambda} &= \frac{1}{I_{4\mathrm{m}}^{22}} \left(T_{i,2}^{\lambda} + (I_{4\mathrm{m}}^{33} - I_{4\mathrm{m}}^{11}) \omega_{i,1}^{\lambda} \omega_{i,3}^{\lambda} \right), \\
\dot{\omega}_{i,3}^{\lambda} &= \frac{1}{I_{4\mathrm{m}}^{33}} \left(T_{i,3}^{\lambda} + (I_{4\mathrm{m}}^{11} - I_{4\mathrm{m}}^{22}) \omega_{i,1}^{\lambda} \omega_{i,2}^{\lambda} \right),
\end{aligned} \tag{32}$$

where $T_{i,\alpha}^{\lambda}$ indicates the α-th component of the torque acting on the angular velocity component $\omega_{i,\alpha}^{\lambda}$ expressed in coordinates of the basis system $\{\vec{\lambda}_{\alpha,i}\}_{\alpha}$. After the evaluation of (32) $\dot{\vec{\omega}}_i$ is transformed to coordinates of the space fixed standard basis for further use. The changes of basis are performed as

$$\begin{aligned}
\vec{\omega}_i^{\,\mathrm{sf}} &\mapsto \vec{\omega}_i^{\,\lambda} = (A_i^{\alpha\beta})^{-1} \, \vec{\omega}_i^{\,\mathrm{sf}}, \\
\vec{T}_i^{\,\mathrm{sf}} &\mapsto \vec{T}_i^{\,\lambda} = (A_i^{\alpha\beta})^{-1} \, \vec{T}_i^{\,\mathrm{sf}}, \\
\dot{\vec{\omega}}_i^{\,\lambda} &\mapsto \dot{\vec{\omega}}_i^{\,\mathrm{sf}} = A_i^{\alpha\beta} \, \dot{\vec{\omega}}_i^{\,\lambda},
\end{aligned} \tag{33}$$

where $A_i^{\alpha\beta} = \left(\vec{\lambda}_{1,i}^{\,4\mathrm{m}} \vec{\lambda}_{2,i}^{\,4\mathrm{m}} \vec{\lambda}_{3,i}^{\,4\mathrm{m}} \right)_{\alpha\beta}$ and the inverse is computed as its transpose $(A_i^{\alpha\beta})^{-1} = (A_i^{\alpha\beta})^{\mathrm{T}}$, because $\det(A_i^{\alpha\beta}) = 1$ by definition. Copies of $\vec{\omega}_i^{\,\mathrm{sf}}$ and $\vec{T}_i^{\,\mathrm{sf}}$ are kept stored to avoid performing the back-transformation.

4.3 Rigid Body Dynamics

When monomers are modelled as rigid bodies their rotational degrees of freedom have to be considered within the velocity Verlet algorithm. The procedure in (22) has to be extended by the rotational dynamics which consists equivalently of four steps:

$$\begin{aligned}
\vec{\omega}_i \left(t + \frac{\delta t}{2} \right) &= \vec{\omega}_i(t) + \frac{\delta t}{2} \dot{\vec{\omega}}_i(t) \\
\chi_i(t + \delta t) &= R_{\chi} \left[\delta t \vec{\omega}_i \left(t + \frac{\delta t}{2} \right) \right] \chi_i(t) \\
\dot{\vec{\omega}}_i(t + \delta t) &\equiv \dot{\vec{\omega}}_i(\{\vec{r}_j(t + \delta t)\}, \{\chi_j(t + \delta t)\}) \\
\vec{\omega}_i(t + \delta t) &= \vec{\omega}_i \left(t + \frac{\delta t}{2} \right) + \frac{\delta t}{2} \dot{\vec{\omega}}_i(t + \delta t).
\end{aligned} \tag{34}$$

The steps are performed simultaneously to the translational counterparts of (22) where the monomer is moved as a whole according to the bead velocity $\vec{v}_i$. In the rotational part, first, the angular velocity is boosted by a half-kick of the current angular acceleration. A rotation $R_\chi\left[\vec{\omega}_i\left(t+\frac{\delta t}{2}\right)\delta t\right]$ of the monomer orientation $\chi_i(t)$ by an angle $\left|\vec{\omega}_i\left(t+\frac{\delta t}{2}\right)\right|\delta t$ around rotation axis $\vec{\omega}_i/\left|\vec{\omega}_i\right|$ follows. If the 4m model is used, the rotation of step 2 will not only alter the orientation χ_i but also the bead's position $\vec{r}_i \neq \vec{r}_{\mathrm{c.m.},i}$ itself. Therefore, in this case the rotation of the monomer orientation $\chi_i(t+\delta t) = R_\chi\left[\delta t\vec{\omega}_i\left(t+\frac{\delta t}{2}\right)\right]\chi_i(t)$ has to be accompanied by a rotation of the bead position around the monomer's center-of-mass:

$$\vec{r}_i(t) \mapsto \vec{r}_{\mathrm{c.m.},i} + \mathbf{R}\left[\vec{\omega}_i\left(t+\frac{\delta t}{2}\right)\delta t\right](\vec{r}_i(t) - \vec{r}_{\mathrm{c.m.},i}), \tag{35}$$

where $\mathbf{R}\left[\vec{\omega}_i\left(t+\frac{\delta t}{2}\right)\delta t\right]$ is a matrix corresponding to a rotation by an angle $\left|\vec{\omega}_i\left(t+\frac{\delta t}{2}\right)\right|\delta t$ and axis $\vec{\omega}_i/\left|\vec{\omega}_i\right|$. Afterwards, the translation of step 2 in (22) by $\frac{\delta t}{2}\vec{v}_i(t)$ is performed. Next, $\dot{\vec{\omega}}_i$ is updated by solving the equation $\vec{T}_i = \frac{d}{dt}\vec{L}_i = \frac{d}{dt}\left(I_i^{\alpha\beta}\vec{\omega}_i\right)$. The torque and hence also the angular acceleration depend on both the location (all potentials) and the orientation (torsion and alignment) of the monomers. For the 4m rigid body model this requires a change of basis (33) and the evaluation of (32) whereas for the sphere model $\vec{T}_i$ and $\dot{\vec{\omega}}_i$ are always related by the linear equation $\vec{T}_i = \sum_{k=1}^{3}\vec{r}_{\mathrm{pat},i,k}\times\vec{F}_{\mathrm{pat},i,k} = I_{\mathrm{sphere}}\dot{\vec{\omega}}_i$. The forces are calculated as a sum over the gradients of the potentials (20), (21), (26), (27), and (30), see Appendix B for details about the computation of the forces involving patches and angles. Finally, in step 4 a second half-kick updates the angular velocity with the new $\dot{\vec{\omega}}_i(t+\delta t)$. When applying the 4m model it is convenient to perform the subsequent rotation (35) during step 2 at time $t+\delta t$ before the translation which alters the position of the monomer's center-of-mass. $\vec{r}_{\mathrm{c.m.},i}(t+\delta t)$ is computed during the calculation of the torque in step 3 of (34) at time t and is therefore stored for the next rotation at $t+\delta t$. When the polymer is suspended in the MPCD solvent, the collisions only rotate the monomer velocities $\vec{v}_i$ but not the angular velocities $\vec{\omega}_i$ and so the solvent-solute interaction does not affect the rotational degrees directly. The coupling acts on the center-of-mass of monomers, i.e., if the patches are point masses and $\vec{r}_{\mathrm{c.m.},i} \neq \vec{r}_i$, monomer i is sorted into a collision cell according to the position of $\vec{r}_{\mathrm{c.m.},i}$.

4.4 Quaternion Formalism of 3D Rotations

For the implementation into the simulations quaternions are used to quantify the monomer orientation and the corresponding rotational dynamics. This reduces the rotational dynamics to quaternion multiplications and offers a way of regaining the patch positions relative to their beads

if they are needed for calculations. A quaternion can be written as the 4-tuple $q = (q_0, q_1, q_2, q_3) = (q_0, \vec{q})$ where $q_0 \in \mathbb{R}$ is called the scalar part and $\vec{q} = (q_1, q_2, q_3) \in \mathbb{R}^3$ the vector part. $q = (0, \vec{q})$ with zero scalar part is called a vector quaternion. $q = (q_0, \vec{0})$ is called a scalar quaternion for $\vec{q} = \vec{0}$ in which case it is equivalent to a scalar q_0. The multiplication of two quaternions q_a and q_b is defined in the following way:

$$q_a \, q_b = (q_{a0}, \vec{q}_a)(q_{b0}, \vec{q}_b) = (q_{a0}q_{b0} - \vec{q}_a \cdot \vec{q}_b, \; q_{a0}\vec{q}_b + q_{b0}\vec{q}_a + \vec{q}_a \times \vec{q}_b). \tag{36}$$

The quaternions form a non-abelian group with respect to their multiplication which is associative but not commutative in general. The conjugate of a quaternion $q = (q_0, \vec{q})$ is defined as $q^* = (q_0, -\vec{q})$ which brings about the quaternion norm $|q| = \sqrt{qq^*} = \sqrt{q_0^2 + q_1^2 + q_2^2 + q_3^2}$ and the inverse quaternion $q^{-1} = q^*/|q|^2, \; qq^{-1} = q^{-1}q = 1$. A rotation $\mathbb{R}^3 \to \mathbb{R}^3, \vec{p} \mapsto \vec{p}\,'$ by an angle α around axis $\vec{u}$ can be expressed by quaternion multiplication. The 3D vector $\vec{p}$ is projected onto the vector quaternion $p_q = (0, \vec{p})$ and the rotation is performed with a unit quaternion $q(t) = \left(\cos(\frac{\alpha}{2}), \sin(\frac{\alpha}{2})\vec{u}\right)$ ($|q| = |\vec{u}| = 1$ so that $q^* = q^{-1}$) [50]:

$$p'_q = (0, \vec{p}\,') = q \, p_q \, q^*. \tag{37}$$

The monomer orientations $\chi_i(t)$ are represented by unit quaternions $q_i(t) = (q_{i,0}, q_{i,1}, q_{i,2}, q_{i,3}) = (q_{i,0}, \vec{q}_i) = (\cos(\frac{\alpha_i}{2}), \sin(\frac{\alpha_i}{2})\vec{u}_i)$ with $|\vec{u}_i| = 1$. The $q_i(t)$ carry the information about a rotation axis $\vec{u}_i$ and an angle α_i corresponding to the orientation of monomer i at time t. The patch positions $k = 1, 2, 3 \equiv$ blue, red, green are recovered by scaling the standard basis vectors to $l_{\mathrm{pat}}\hat{e}_k$ and rotating them with $q_i(t)$:

$$(0, l_{\mathrm{pat}}\hat{e}_k) \mapsto (0, \vec{r}_{\mathrm{pat},i,k}(t)) = q_i(t)(0, l_{\mathrm{pat}}\hat{e}_k)q_i^*(t). \tag{38}$$

In this way the patch vectors are always guaranteed to both have the correct distance to the bead and be orthogonal to each other so that they span an orthogonal reference system. At the beginning of a simulation run the monomers are given a starting orientation $q_i(0)$ that sets the initial patch positions $(0, \vec{r}_{\mathrm{pat},i,k}(0)) = l_{\mathrm{pat}}q_i(0)(0, \hat{e}_k)q_i^*(0)$. The second step of the rotational velocity Verlet algorithm (34) comprises a rotation of the orientation $q_i(t)$ around axis $\vec{\omega}_i/|\vec{\omega}_i|$ and by an angle $\vec{\omega}_i\delta t$ to $q_i(t + \delta t)$. In terms of quaternions it is computed in the following way with $\vec{\omega}_i = \vec{\omega}_i(t + \frac{\delta t}{2})$:

$$q_i(t + \delta t) = q_{\vec{\omega}_i \delta t}\left(t + \frac{\delta t}{2}\right) q_i(t) = \left(\cos\left(\frac{|\vec{\omega}_i|\delta t}{2}\right), \sin\left(\frac{|\vec{\omega}_i|\delta t}{2}\right)\frac{\vec{\omega}_i}{|\vec{\omega}_i|}\right) q_i(t). \tag{39}$$

Because of associativity the updated $q_i(t+\delta t)$ imparts the same 3D rotation of a vector $\vec{p}$ to $\vec{p}\,'(t+\delta t)$ as $q_i(t)$ followed by a rotation according to $\vec{\omega}_i\delta t$:

$$\begin{aligned} p'_q(t+\delta t) = (0,\vec{p}\,') &= q_i(t+\delta t)\, p_q\, q_i^*(t+\delta t) \\ &= \left(q_{\vec{\omega}_i\delta t}\left(t+\frac{\delta t}{2}\right)\, q_i(t)\right) p_q \left(q_{\vec{\omega}_i\delta t}\left(t+\frac{\delta t}{2}\right)\, q_i(t)\right)^* \\ &= \left(q_{\vec{\omega}_i\delta t}\left(t+\frac{\delta t}{2}\right)\, q_i(t)\right) p_q \left(q_i^*(t)\, q^*_{\vec{\omega}_i\delta t}\left(t+\frac{\delta t}{2}\right)\right) \\ &= q_{\vec{\omega}_i\delta t}\left(t+\frac{\delta t}{2}\right)\, \left(q_i(t)\, p_q\, q_i^*(t)\right) q^*_{\vec{\omega}_i\delta t}\left(t+\frac{\delta t}{2}\right) \\ &= q_{\vec{\omega}_i\delta t}\left(t+\frac{\delta t}{2}\right)\, p'_q(t)\, q^*_{\vec{\omega}_i\delta t}\left(t+\frac{\delta t}{2}\right). \end{aligned} \tag{40}$$

At time t the orientation is given by the time-ordered product of all rotations to the left of $q_i(0)$:

$$q_i(t) = q_{\vec{\omega}_i\delta t}\left(t-\frac{\delta t}{2}\right)\, q_{\vec{\omega}_i\delta t}\left(t-\frac{3\delta t}{2}\right)\, ... \, q_{\vec{\omega}_i\delta t}\left(\frac{3\delta t}{2}\right)\, q_{\vec{\omega}_i\delta t}\left(\frac{\delta t}{2}\right)\, q_i(0), \tag{41}$$

and the step (39) can be repeated $t/\delta t + 1$ many times:

$$\begin{aligned} p'_q(t) &= q_i(t)\, p_q\, q_i^*(t) \\ &= q_{\vec{\omega}_i\delta t}\left(t-\frac{\delta t}{2}\right) ... \, q_{\vec{\omega}_i\delta t}\left(\frac{\delta t}{2}\right) q_i\,(0)\;\; p_q\; q_i^*\,(0)\, q^*_{\vec{\omega}_i\delta t}\left(\frac{\delta t}{2}\right)\, ... \, q^*_{\vec{\omega}_i\delta t}\left(t-\frac{\delta t}{2}\right). \end{aligned} \tag{42}$$

Inserting $p_q = (0,\vec{p}) = (0, l_{\mathrm{pat}}\hat{e}_k)$ and $p_q\,'(t) = (0,\vec{p}\,'(t)) = (0,\vec{r}_{\mathrm{pat},i,k}(t))$ into (40) and (42) makes evident that (38) and (39) reproduce the monomer orientations at all time steps. The quaternions must always have unity norm, i.e., $|q_i(t)| = 1$ so that they represent proper rotations. It holds that $\left|q_{\vec{\omega}_i\delta t}\left(t+\frac{\delta t}{2}\right)\right| = 1$, i.e., normalization to unity is guaranteed for all time steps t, if the initial $q_i(0)$ have unity norm. The quaternions are normalized $q_i(t) \mapsto q_i(t)/|q_i(t)|$ in regular time intervals to counteract numerical errors which can possibly occur along the way.

The quaternion representation is used for both rigid body models, '4m' and 'sphere'. If the former one is used, the rotation of the bead (35) relative to the monomer's center-of-mass has to be performed in addition to the quaternion multiplication (39).

4.5 Stationary State Properties of Supercoiled Rings

The conformations of the supercoiled ring polymers are influenced by an interplay of the applied bending and torsional constraints. They are expected to take on more open and stiffer geometries because of the additional potentials compared to the fully flexible ring discussed in section 3.4 The rings' geometry is further analyzed by measuring their writhe Wr. For a closed curve C in three-dimensional space the writhe is defined as follows:

$$\mathrm{Wr} = \frac{1}{4\pi} \int_C \int_C \frac{(d\vec{r}_2 \times d\vec{r}_1)\, \vec{r}_{12}}{r_{12}^3}, \tag{43}$$

where $\vec{r}_1$ and $\vec{r}_2$ are points on the curve C and $\vec{r}_{12} = \vec{r}_2 - \vec{r}_1$. The quantity writhe gives an intuitive measure of how many crossings the molecular backbone forms with itself. For its computation a discrete version of (43) is used which has been presented in [51]. It is applicable to polymers in computer simulations where they are usually composed of N_m straight line segments connected by the monomer positions. For this thesis the bead positions serve as the reference points for the evaluation of the writhe according to [51].

Additionally, the twist is computed for the torsionally constrained polymer rings by summing over all dihedral angles that are the input to the torsion potential terms:

$$\mathrm{Tw} = \frac{1}{2\pi} \sum_{i=1}^{N_m} \frac{\Psi_{b,i} + \Psi_{r,i}}{2}. \tag{44}$$

The blue and red patches each form an individual set of dihedral angles $\{\Psi_{b,i}\}$, respectively $\{\Psi_{r,i}\}$. An arithmetic mean over the two is taken in the evaluation of Tw in (44).

The alignment potential forces the green patches to be aligned nearly perfectly with the polymer backbone so that the blue and red patches are kept in a perpendicular orientation to it. A high value is picked for the constant k_{align} which minimizes fluctuations from this structure. For this reason, the vectors $\vec{r}_{\mathrm{pat},i,r/b}$ serve as (unnormalized) normal vectors to the space curve approximated by the bead positions $\vec{r}_i$. The addition of patches therefore gives the simulated ring polymer the structure of a closed ribbon which is simple because of the excluded volume. Therefore, it obeys to Călugăreanu's theorem which states that the Linking number Lk of a simple closed ribbon as the sum over its writhe and twist is a conserved quantity [52]:

$$\mathrm{Lk} = \mathrm{Wr} + \mathrm{Tw} = \mathrm{const.} \tag{45}$$

The polymer rings are initialized as flat open ribbons meaning that the green patches are aligned with the backbone and the blue and red patches are orientated perpendicularly to it. In this

conformation the Linking number is zero. Rings with nonzero supercoiling, $\sigma_{\mathrm{sc}} > 0$, cannot be used directly for further MD simulations since the torsional forces would be immense in this conformation and lead to unpredictable behaviour and simulation crashes. Supercoiled rings must be initialized in a state with minimal torsional energy. These are generated by starting from a flat open ribbon and performing MD steps while gradually ramping up the offset of the torsional potential Ψ_0 from zero to the desired angle $2\pi\sigma_{\mathrm{sc}}$ in small steps. During this procedure monomers are coupled to the random MPCD solvent for a time efficient way of momentum and energy exchange. The offset is increased in steps of $0.1\% \cdot 2\pi\sigma_{\mathrm{sc}}$ after every 2000 collisions with the solvent until the final angle is reached. The resulting conformations are supercoiled rings with twist values fluctuating around $N_m\sigma_{\mathrm{sc}}$ and writhe $\mathrm{Wr} \approx -\mathrm{Tw}$ so that $Lk = 0$ is indeed approximately conserved. The initialization process is performed for both monomer models 'sphere' and '4m' for the supercoiling values $\sigma_{\mathrm{sc}} = 0.01$ and $\sigma_{\mathrm{sc}} = 0.02$.

Supercoiled rings of both monomer types, respectively with $\sigma_{\mathrm{sc}} = 0.00, 0.01, 0.02$ and torsionally relaxed ones, are then allowed to evolve freely in time in equilibrium ($\dot{\gamma} = 0$) while the quantities of interest are being monitored to find out when the stationary state is reached. In that process they are coupled to the MPCD solvent both with and without HI in separate runs to see whether differences occur against expectations. To get more precise results, ten independent simulation runs are conducted for $\dot{\gamma} = 0$ to increase the number of curves summed up to one averaged curve. It must be mentioned that rings with the highest supercoiling chosen, $\sigma_{\mathrm{sc}} = 0.02$, crash with a certain probability. The effective reason for the crashes has not been found, though it has become clear that the higher degree of writhe makes the rings crumble to more contracted conformations. This leads to situations where the contorted macrostructure of the polymer forces some beads to be pressed together and thus, the risk of building up large repulsive forces resulting in nonphysical behaviour. This occurs for both models mainly when HI is absent (five times for the 4m model and three times for the sphere model out of ten runs respectively) since the amount of MD steps is much higher here compared to the costly particle-based solvent with HI (only one crash for the sphere model). Therefore, the chances of a crashing situation increases with the length of the simulation runs which cannot be decreased significantly. It has to be long enough to cover the long time behaviour of the rings without HI which have longer characteristic time scales. The collected data of crashed runs has to be discarded from further evaluation.

Fig. 15 shows the quantities writhe and twist as functions of time for all systems simulated whereby the curves of the single runs which have not crashed are averaged to a single curve. One can see that for each torsionally constrained ring the twist fluctuates closely around zero in case of $\sigma_{\mathrm{sc}} = 0.00$ and a value somewhat smaller than the anticipated $\mathrm{Tw} = N_m\sigma_{\mathrm{sc}}$ for $\sigma_{\mathrm{sc}} > 0$. Furthermore, Călugăreanu's theorem is indeed fulfilled for these systems since the writhe approximately equals the twist with opposite sign. The relaxed chains remain in a state

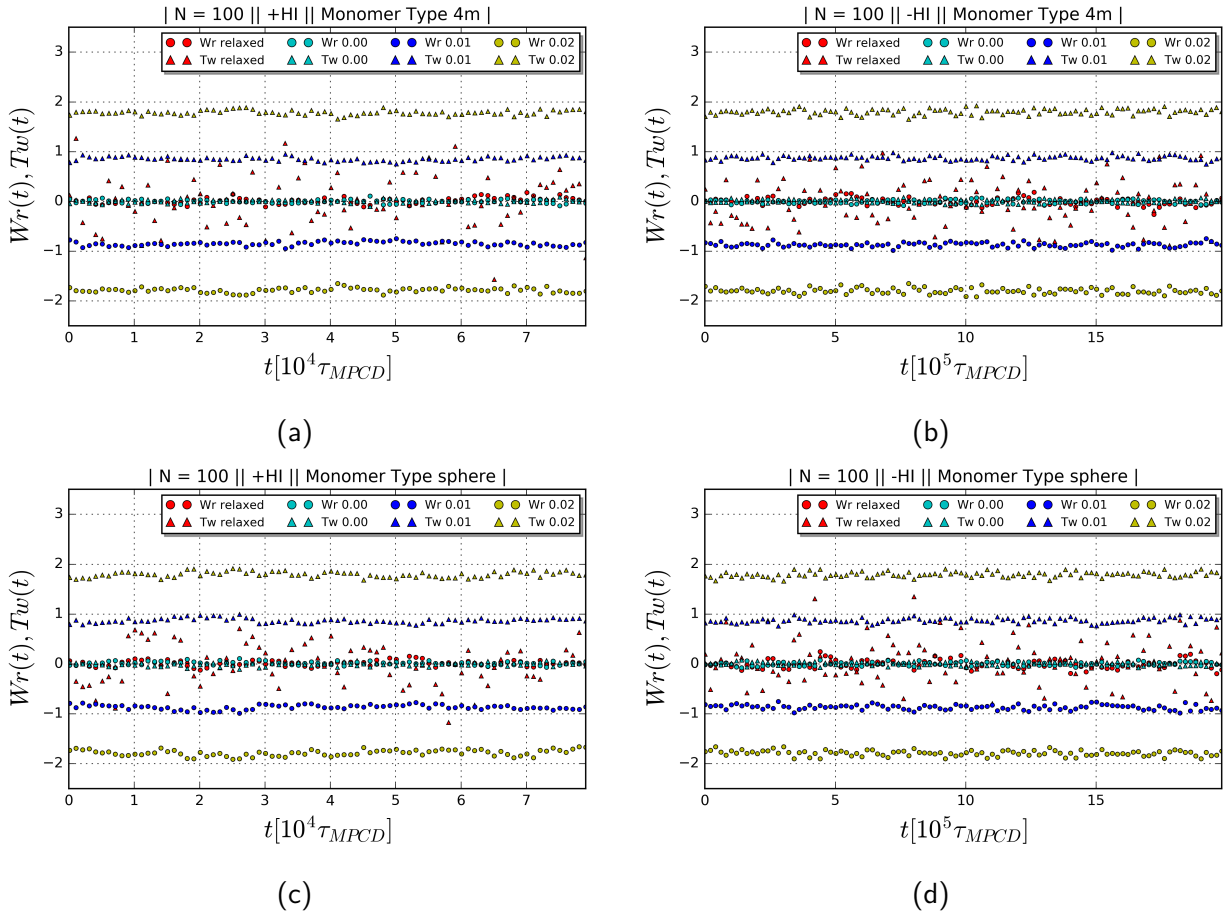

Figure 15: Writhe and twist of supercoiled rings of length $N_m = 100$ as functions of time starting from the initialization states. (a) Monomer type 4m with HI, (b) monomer type 4m without HI, (c) Monomer type sphere with HI, and (d) Monomer type sphere without HI. Curves shown are averaged over up to ten ensemble runs. Crashed runs had to be discarded.

with only few writhe because of the bending stiffness and the quantity twist fluctuates arbitrarily for relaxed chains because of the absence of torsional springs so that it is futile in this case. The behaviour does neither depend on the choice of monomer model nor the presence of HI.

In Fig. 16 the radius of gyration is plotted as a function of time for all systems simulated. Again, the values fluctuate around their respective mean and the behaviour does not depend on the choice of monomer type or the presence of HI. The torsional constraint gives the supercoiled rings an increased stiffness compared to the relaxed rings. The $\sigma_{\mathrm{sc}} = 0.00$ rings are locked in a rather open and flat conformation and R_g^2 fluctuates more weakly around a bigger mean compared to the relaxed counterparts. In contrast, nonzero supercoiling forces the polymers to take on more complex shapes, e.g., figure-eights which leads to a smaller radius of gyration $R_g^2(0)[\sigma_{\mathrm{sc}} > 0]$.

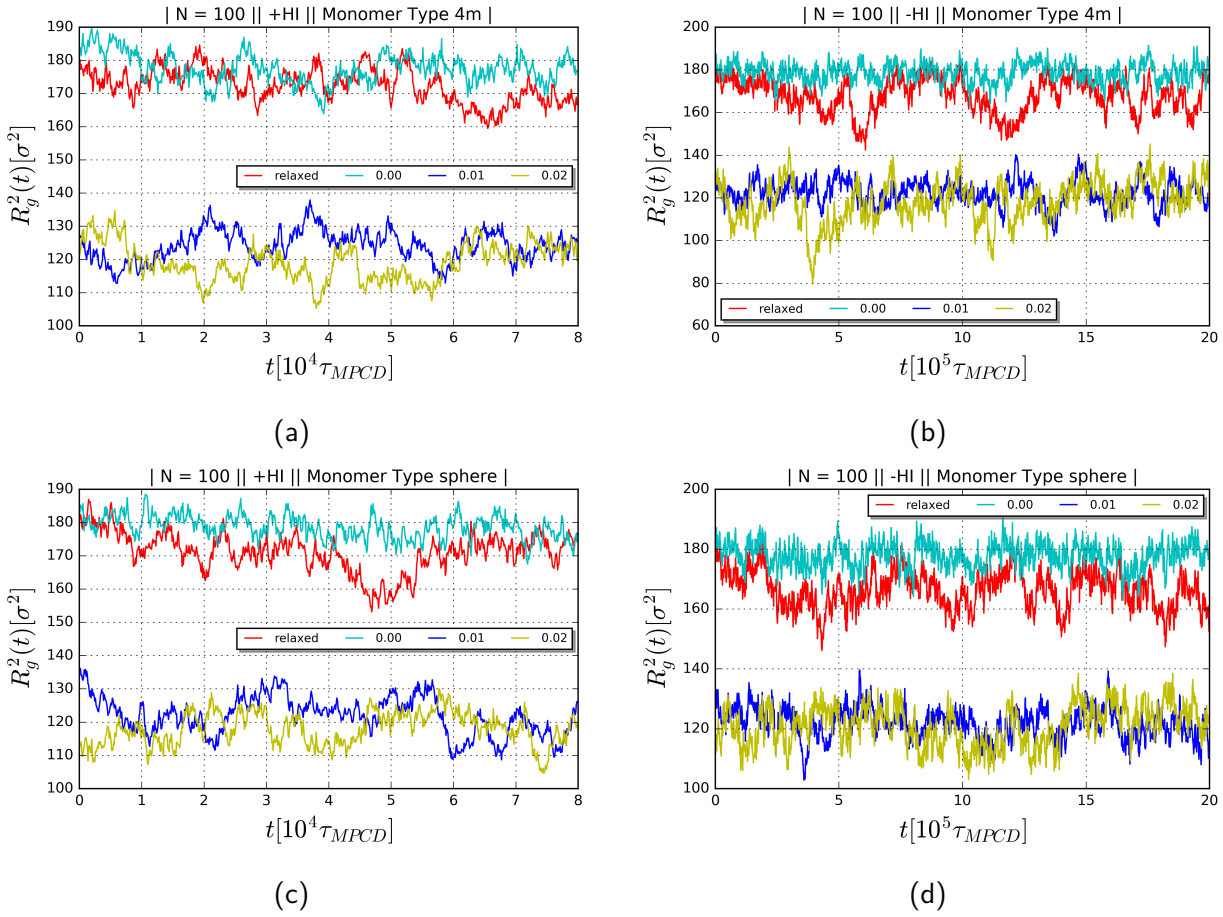

Figure 16: Radius of gyration of supercoiled rings of length $N_m = 100$ as a function of time starting from the initialization states. (a) Monomer type 4m with HI, (b) monomer type 4m without HI, (c) Monomer type sphere with HI, and (d) Monomer type sphere without HI. Curves shown are averaged over up to ten ensemble runs. Crashed runs had to be discarded.

The polymer rings are deemed to be in a stationary state towards the end of the simulation duration. Therefore, the equilibrium conformations are sampled from the last 30% of the simulation time. The corresponding distributions of the radius of gyration are presented in Fig. 17. The stationary state values for radius of gyration, writhe and twist are computed as averages over ensembles and time whereby values are taken from the stationary conformations. The results are summarized in Table 1 which includes the values of the unsupercoiled ring from the previous section for comparison. The values of $R_g^2(0)[\sigma_{\mathrm{sc}}]$ coincide within their respective statistical errors for the two different monomer models and for the solvents with and without HI. Hence, there is no noteworthy influence of the type of rigid body one selects for the modelling of monomers. Furthermore, HI do not affect the stationary properties of the supercoiled rings in the absence of shear flow.

Polymer Type	σ_{sc}	$R_g^2(0)/\sigma^2$ (+HI)	$R_g^2(0)/\sigma^2$ (-HI)	Wr	Tw
Fully Flexible Ring	/	28.95 (4.00)	/	/	/
Supercoiled Ring (4m)	r	167.58 (3.63)	168.26 (7.00)	0.07 (0.05)	/
	0.00	177.27 (3.11)	178.55 (4.67)	0.00 (0.03)	0.00 (0.03)
	0.01	123.03 (4.02)	122.21 (6.35)	-0.88 (0.05)	0.88 (0.05)
	0.02	121.85 (4.43)	124.15 (6.65)	-1.78 (0.04)	1.78 (0.04)
Supercoiled Ring (Sphere)	r	172.66 (3.05)	165.54 (6.12)	0.00 (0.05)	/
	0.00	177.77 (3.59)	177.69 (4.33)	0.00 (0.03)	0.00 (0.03)
	0.01	117.38 (5.24)	121.08 (5.20)	-0.88 (0.03)	0.88 (0.03)
	0.02	118.58 (5.36)	125.54 (4.94)	-1.76 (0.06)	1.79 (0.05)

Table 1: Time and ensemble averages of all quantities measured for rings of length $N_m = 100$ ($\dot{\gamma} = 0$) as well as characteristic relaxation times. Absolute errors are noted in parentheses. The letter 'r' indicates relaxed rings without torsional constraint. All averages of writhe and twist are calculated from the runs with HI present exclusively.

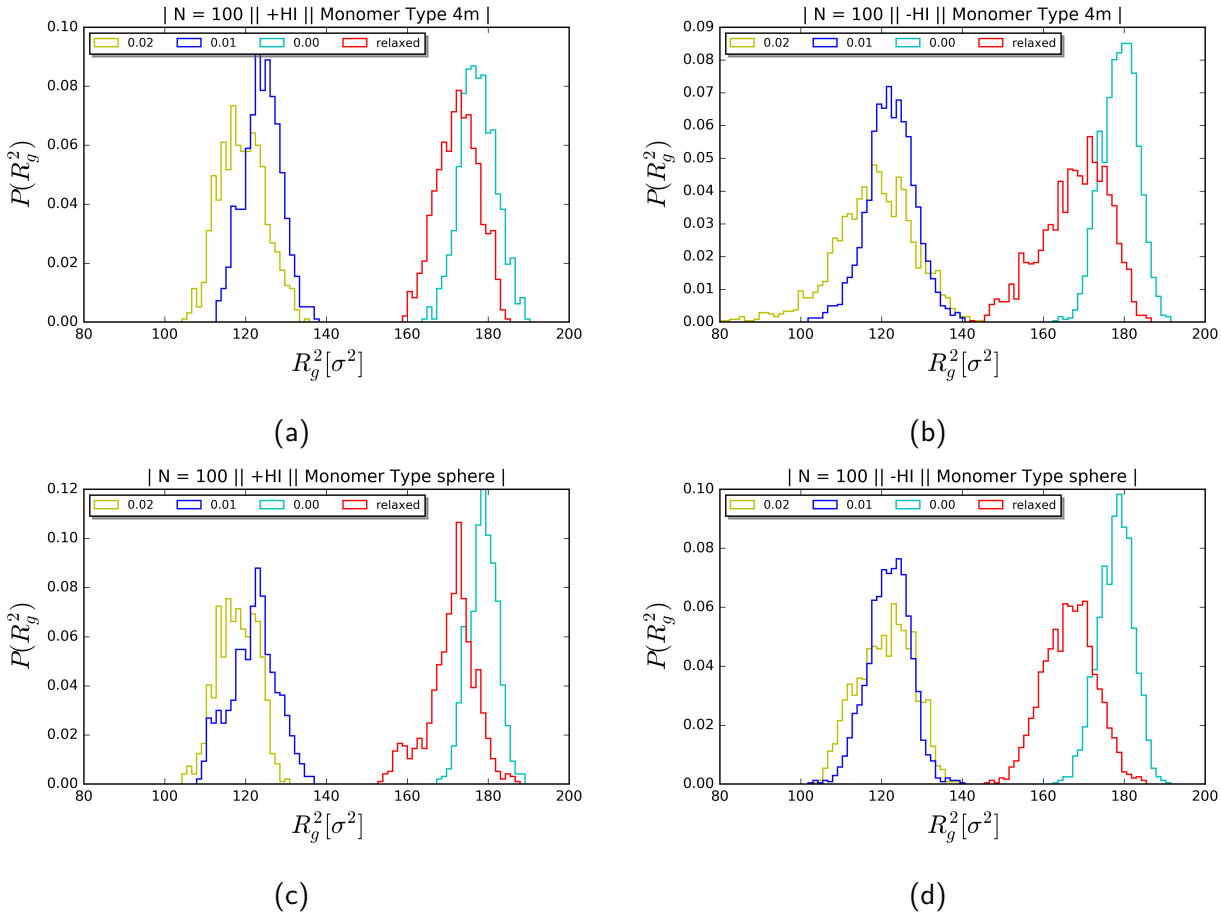

Figure 17: Stationary distribution of the radius of gyration of supercoiled rings of length $N_m = 100$ taken from the last 30% of the respective simulation time. (a) Monomer type 4m with HI, (b) monomer type 4m without HI, (c) Monomer type sphere with HI, and (d) Monomer type sphere without HI. Distributions shown are taken from up to ten ensemble runs. Crashed runs had to be discarded.

For $\sigma_{\mathrm{sc}} = 0.00$ both the bending and the torsional stiffness force the ring to remain in an open circular shape which leads to a sharp peak in the R_g^2-distributions. The absence of torsional stiffness softens the relaxed rings leading to slightly smaller sizes. In agreement with Smrek et al. [31] the radius of gyration decreases with nonzero supercoiling for a ring of this length. This can be understood as the effect of the writhing which forces the polymers into a more elongated shape and thereby shrinking its overall radius of gyration, see Fig. 18.

The relaxation times of supercoiled rings cannot be extracted by means of the end-to-end correlation function as before. There is no apparent exponential decay of the quantity for any of the systems simulated. The rings seem to be too stiff to forget about their initial conditions quickly

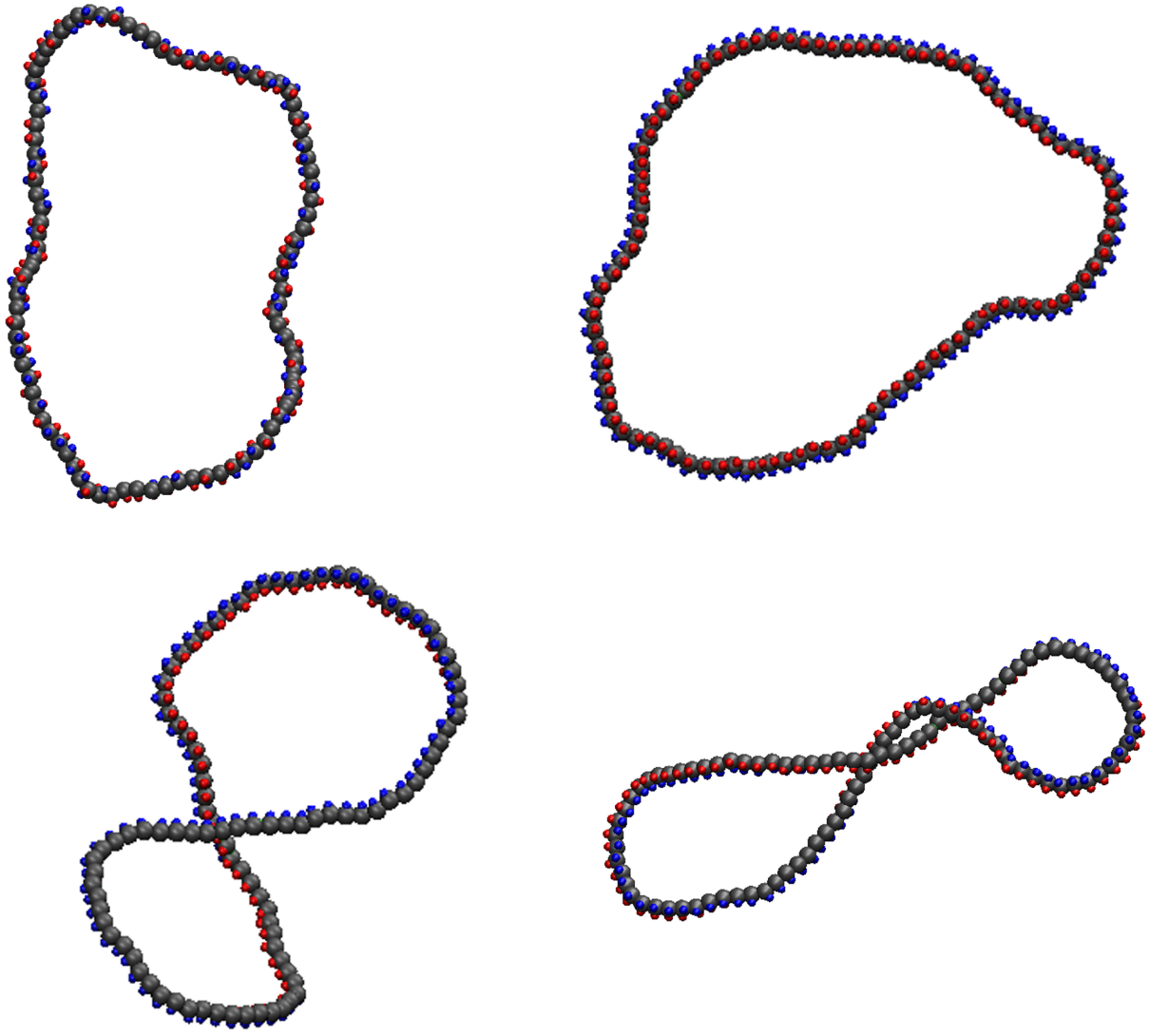

Figure 18: Snapshots of supercoiled ring polymers. Bead positions are imaged as big gray spheres with excluded volumes. Blue and red patches form the dihedral angles, whereas green patches are covered in this illustration. Top left: relaxed. Top right: $\sigma_{\mathrm{sc}} = 0.00$. Bottom left: $\sigma_{\mathrm{sc}} = 0.01$. Bottom right: $\sigma_{\mathrm{sc}} = 0.02$.

enough. Furthermore, the curves corresponding to polymers with nonzero supercoiling demonstrate oscillatory behaviour indicating that they rotate around their center-of-mass. Overall, the end-to-end correlation does not seem to be the appropriate quantity to determine a characteristic time scale. For that reason, no characteristic time scales are determined for supercoiled rings. Therefore, the intensity of flow profiles are specified by the mere shear rate and not corresponding Weissenberg numbers in the following discussion of supercoiled ring polymers under shear flow. This leads to a more qualitative than quantitative evaluation of the phenomena occurring.

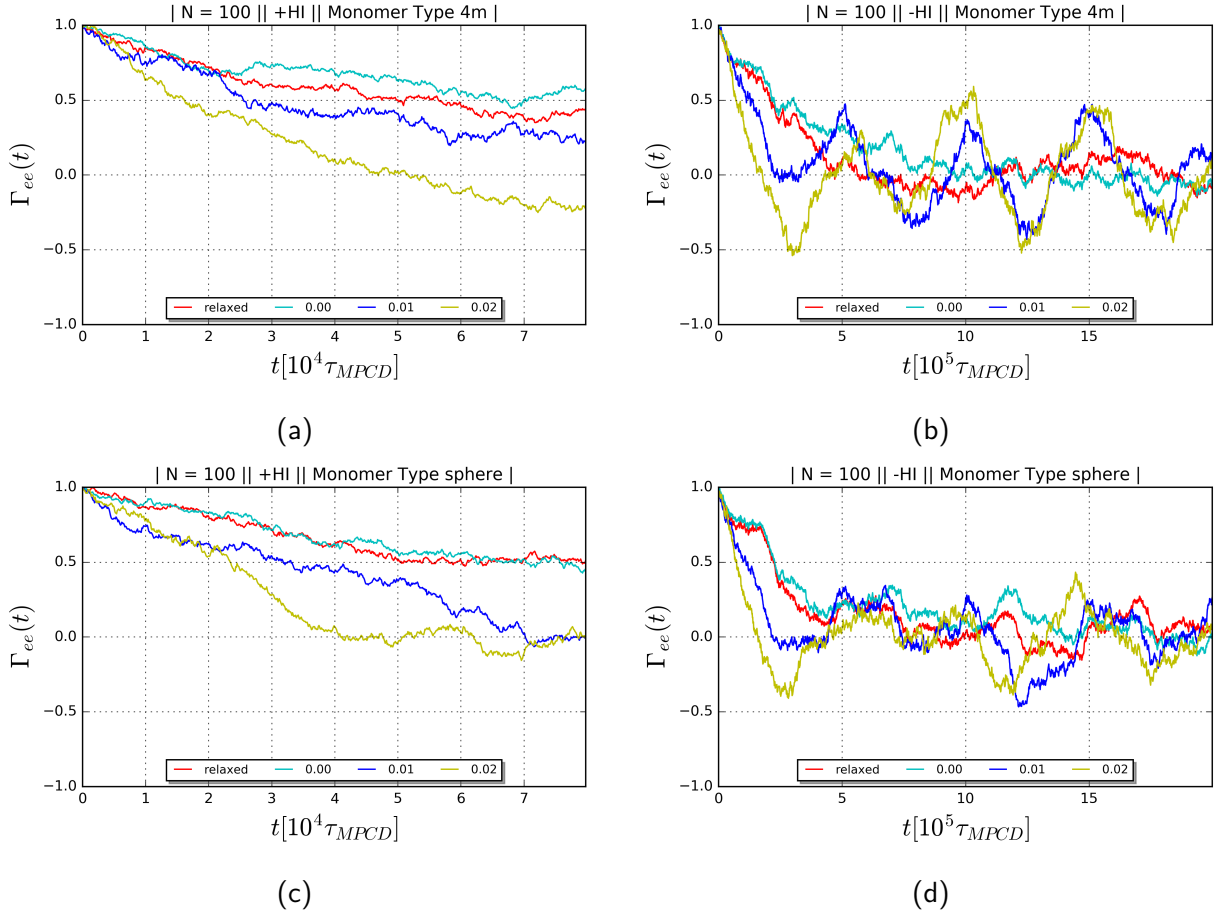

Figure 19: End-to-end correlation of supercoiled rings of length $N_m = 100$ as a function of time starting from the initialization states. (a) Monomer type 4m with HI, (b) monomer type 4m without HI, (c) Monomer type sphere with HI, and (d) Monomer type sphere without HI. Curves shown are averaged over up to ten ensemble runs. Crashed runs had to be discarded.

5 Supercoiled Ring Polymers under Shear Flow

Simulations of supercoiled ring polymers under shear flow are performed for a ring of length $N_m = 100$ for different choices of supercoiling $\sigma_{\mathrm{sc}} = 0.0, 0.01, 0.02$ and for the relaxed rings with $k_{\mathrm{torsion}} = 0$. The supercoiled ring polymers are coupled to the particle-based MPCD solvent and to the random MPCD solvent in separate runs to determine any effects of HI on the supercoiled ring conformations. The monomers are modelled with the 'sphere' rigid bodies which has proven to be more stable against crashes and numerically more efficient because the tensor of inertia breaks down to a scalar and rotations around the the monomer's center-of-mass do not affect the bead position. The behaviour under shear flow is investigated by taking time averages of the diagonal components of the gyration tensor, the writhe and the twist for shear rates from multiple orders of magnitude. One simulation run is conducted for each choice of system parameters. The systems without HI are run for longer times since the particle-based MPCD took up most of the numerical effort when HI is active. On the flip side the polymers with $\sigma_{\mathrm{sc}} > 0$ are more prone to

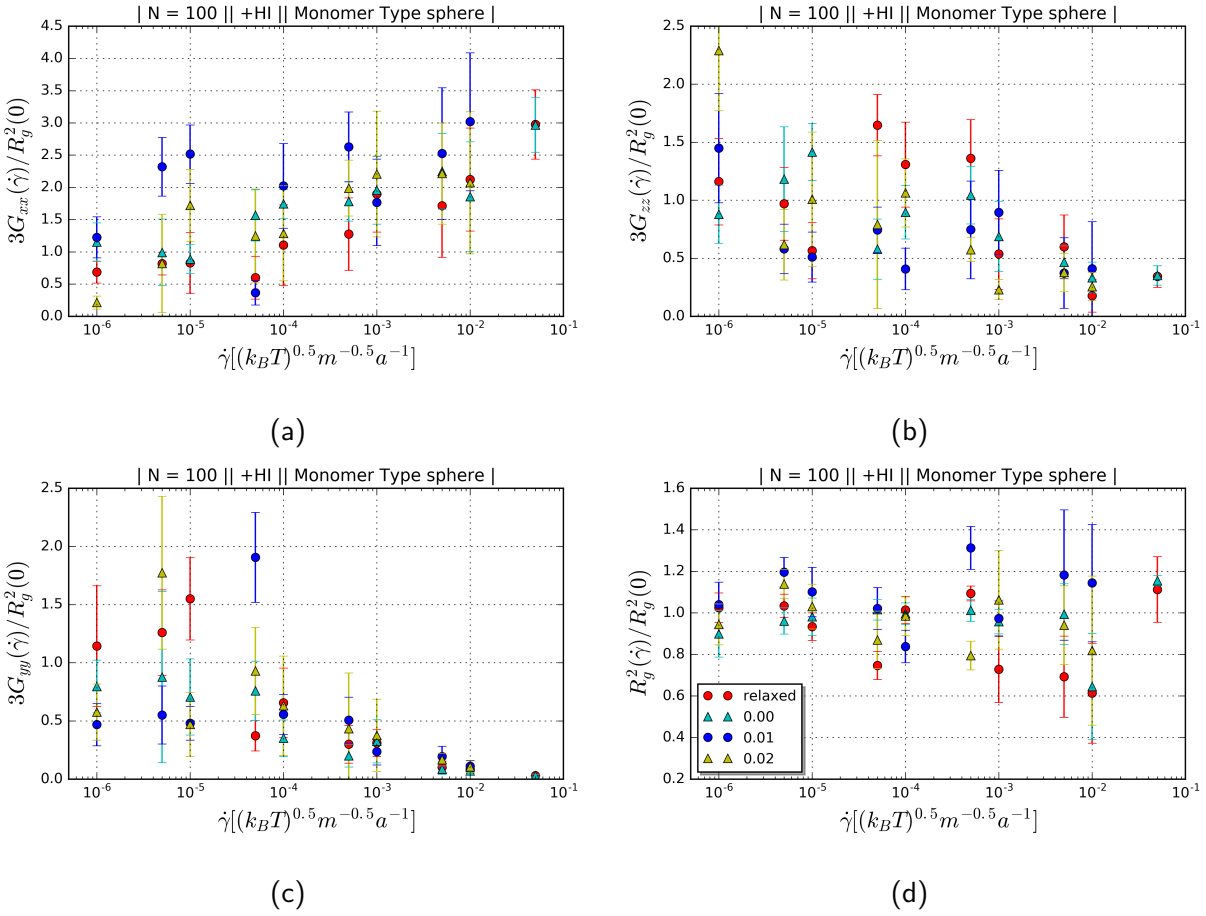

Figure 20: Components of the gyration tensor as functions of the shear rate with hydrodynamic interactions (+HI) active. In (a) flow-, (b) vorticity-, and (c) gradient-direction for a supercoiled ring of length $N_m = 100$ and $\sigma_{\mathrm{sc}} = \mathrm{relaxed}, 0.00, 0.01, 0.02$. The trace gives the squared radius of gyration (d). All plots are normalized to the equilibrium value $R_g^2(0)$.

crashes for -HI so it is not possible to measure their gyration tensor for very high shear rates.

The results for the diagonal elements of $G_{\alpha\beta}(\dot{\gamma})$ with hydrodynamic interactions active (+HI) are depicted in Fig. 20 together with $R_g^2 = \mathrm{tr}[G_{\alpha\beta}]$. Regardless of the degree of supercoiling the component in flow direction increases with higher shear rates while the components in vorticity and gradient directions both get smaller. Interestingly, the growth of G_{xx} is limited to a factor of $\approx 2-3$ for all shear rates covered which is small compared to the growth factor of the fully flexible rings which reach values up to $\approx 15-20$. Also, the decrease of G_{yy} and G_{zz} is compensated by the increase in flow direction so that R_g^2 is more or less constant over the entire range of $\dot{\gamma}$. The same behaviour occurs when HI is switched off by coupling the supercoiled polymers to the random MPCD solvent (-HI), see Fig. 21. Because the sample size covers longer time periods, the effect is even clearer in the case of no HI. One can see that growth of G_{xx} saturates at $\dot{\gamma} \approx 10^{-3} - 10^{-2}(k_BT)^{0.5}m^{-0.5}a^{-1}$ and that the contraction in gradient direction is slightly more pronounced than in vorticity direction. For -HI the radius of gyration $R_g^2(\dot{\gamma})$ deviates only very

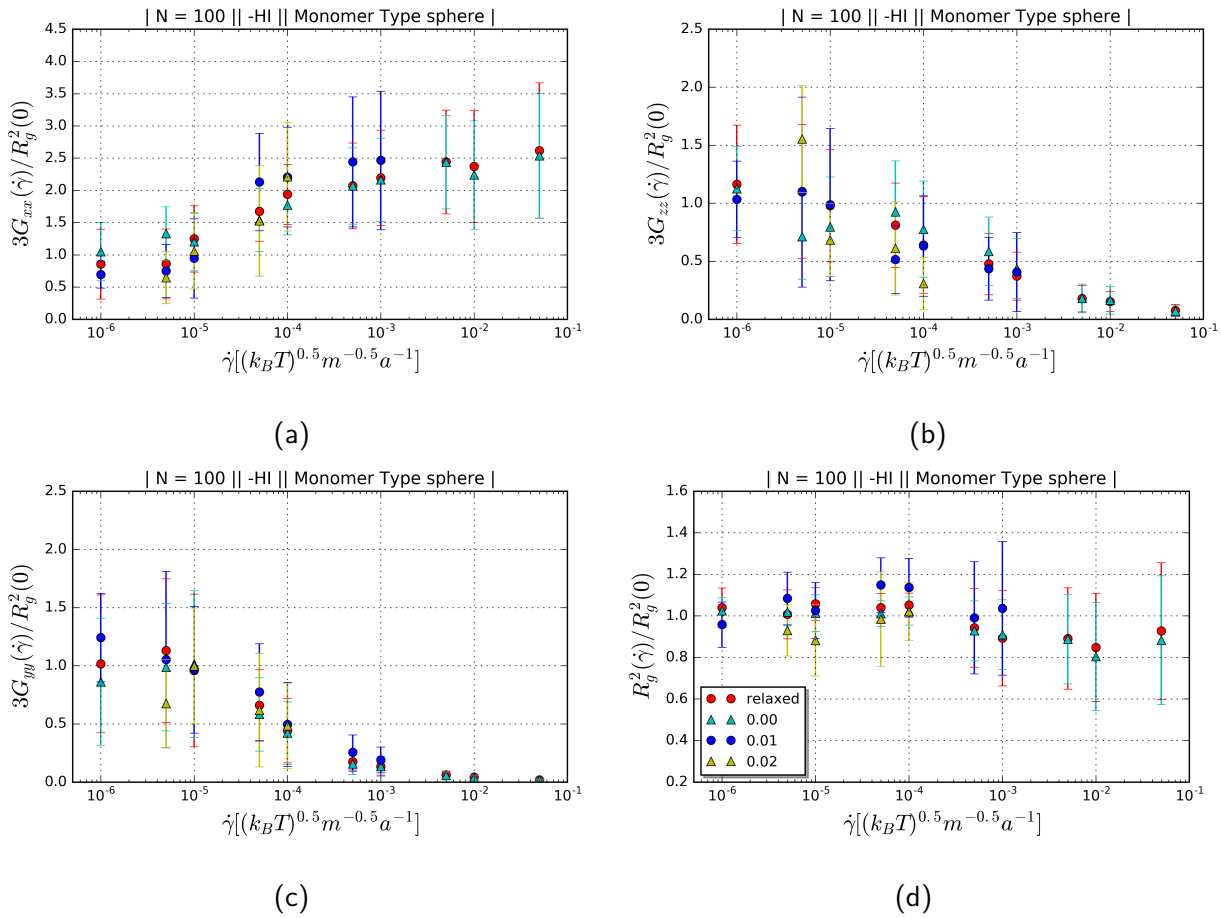

Figure 21: Components of the gyration tensor as functions of the shear rate without hydrodynamic interactions (-HI) active. In (a) flow-, (b) vorticity-, and (c) gradient-direction for a supercoiled ring of length $N_m = 100$ and $\sigma_{\mathrm{sc}} = \mathrm{relaxed}, 0.00, 0.01, 0.02$. The trace gives the squared radius of gyration (d). All plots are normalized to the equilibrium value $R_g^2(0)$.

little from the stationary value $R_g^2(0)$. To investigate the conformations of the supercoiled rings under shear, time averages of the writhe and twist are computed, see Fig. 22. In all cases and over the entire range of shear rates observed, the linking number $\mathrm{Lk} = 0$ is conserved and writhe and twist remain constant at their preferred values according to their degree of supercoiling σ_{sc}. Only the relaxed rings demonstrate some fluctuations of Wr around its mean for higher values of $\dot{\gamma}$.

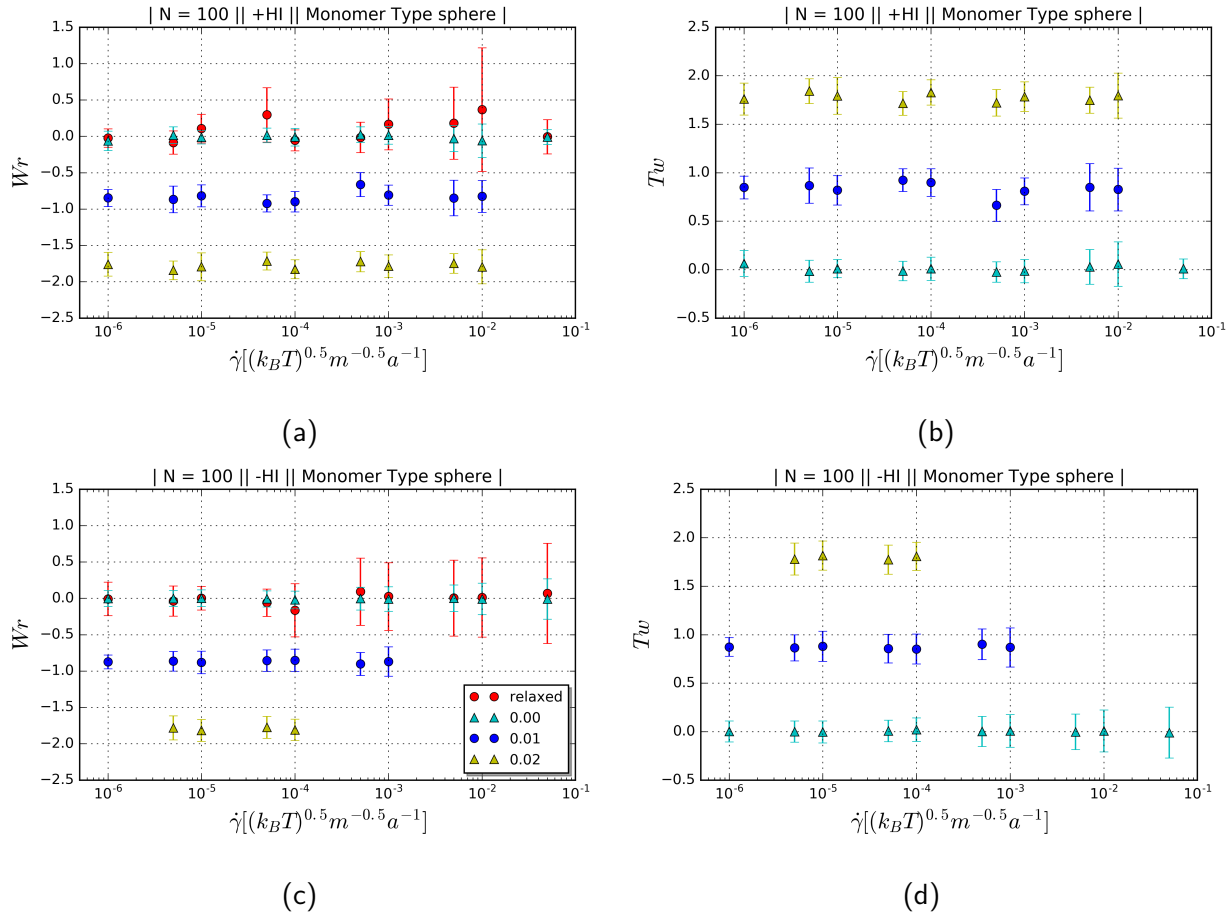

Figure 22: Writhe and twist of supercoiled polymers of length $N_m = 100$ and $\sigma_{\mathrm{sc}} = \mathrm{relaxed}, 0.00, 0.01, 0.02$ under shear flow: (a) Wr (+HI), (b) Tw (+HI), (c) Wr (-HI), and (d) Tw (-HI) as functions of the shear rate.

So far, the results for $G_{\alpha\alpha}$, Wr, and Tw suggest that the effect of shear flow on the conformations of supercoiled ring polymers is limited to strong alignment with the flow direction and weak shrinkage in vorticity and gradient directions while the overall shape alters minimally. Over all shear rates tested, the Writhe and twist remain constant and $R_g^2(\dot{\gamma})$ fluctuates only weakly around $R_g^2(0)$. Additionally, HI hardly plays a role for the properties of supercoiled polymers. To get more insight into the response to shear flow, the relative shape anisotropy δ^* is computed from the eigenvalues λ_1, λ_2, λ_3 of $G_{\alpha\beta}(t)$:

$$\delta^* = \frac{3}{2}\left\langle \frac{\lambda_1^2 + \lambda_2^2 + \lambda_3^2}{R_g^4} \right\rangle - \frac{1}{2}, \tag{46}$$

where $\langle ... \rangle$ indicates time averaging. $\delta^* = 0$ occurs only if all monomers are arranged in spherical symmetry while $\delta^* = 1$ indicates that all monomers are positioned on a line. The relative shape anisotropy is independent of the polymer's orientation in space. In Fig. 23, one can see that δ^* depends on the degree of supercoiling. For small shear rates, $\dot{\gamma} < 10^{-4}(k_BT)^{0.5}m^{-0.5}a^{-1}$, before the polymer is orientated by the flow, the supercoiling already forces the $\sigma_{\mathrm{sc}} = 0.02$-ring to a stretched structure have a constant anisotropy of > 0.6 while the open $\sigma_{\mathrm{sc}} = 0.00$-ring has values $\delta^* \approx 0.3$. At higher shear rates, $\dot{\gamma} > 10^{-4}(k_BT)^{0.5}m^{-0.5}a^{-1}$, the supercoiled rings are elongated in flow direction which increases the anisotropy for $\sigma_{\mathrm{sc}} = 0.00$, $\sigma_{\mathrm{sc}} = 0.01$ and $\sigma_{\mathrm{sc}} = \mathrm{relaxed}$ as they are stretched out by the solvent and reach values of up to $\delta^* \approx 0.8 - 0.9$. This effect occurs with and without the presence of HI. The snapshots of supercoiled rings with $\sigma_{\mathrm{sc}} = 0.01$ in Fig. 24 and $\sigma_{\mathrm{sc}} = 0.02$ in Fig. 25 give an idea of the polymers' elongation under shear flow in comparison to their shape in free flow $\dot{\gamma} = 0$. The typical conformations characterized by the amount of self-crossings of the polymer backbone are not affected by shear flow as writhe and twist are conserved. The figure-eight shape of the $\sigma_{\mathrm{sc}} = 0.01$-ring in Fig. 24 is concealed by the perspective since the crossing is not aligned with the flow-vorticity plane. At a fairly high shear rate of $\dot{\gamma} = 5 \cdot 10^{-4}(k_BT)^{0.5}m^{-0.5}a^{-1}$ the figure-eight aligns with the flow-vorticity plane. The effect is even more obvious for the $\sigma_{\mathrm{sc}} = 0.02$-ring in Fig. 25 at an even higher shear rate of $\dot{\gamma} = 10^{-2}(k_BT)^{0.5}m^{-0.5}a^{-1}$. In contrast to the unsheared counterpart, the polymer is almost completely stretched out and aligned with along flow direction.

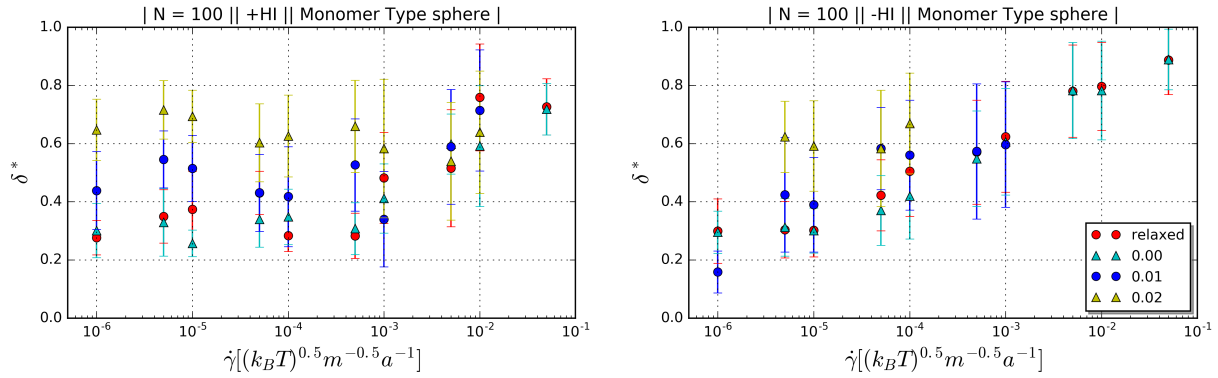

(a) (b)

Figure 23: Relative shape anisotropy δ^* for a supercoiled ring of length $N_m = 100$ and $\sigma_{\mathrm{sc}} = \mathrm{relaxed}, 0.00, 0.01, 0.02$. As a function of $\dot{\gamma}$ (a) +HI, (b) -HI.

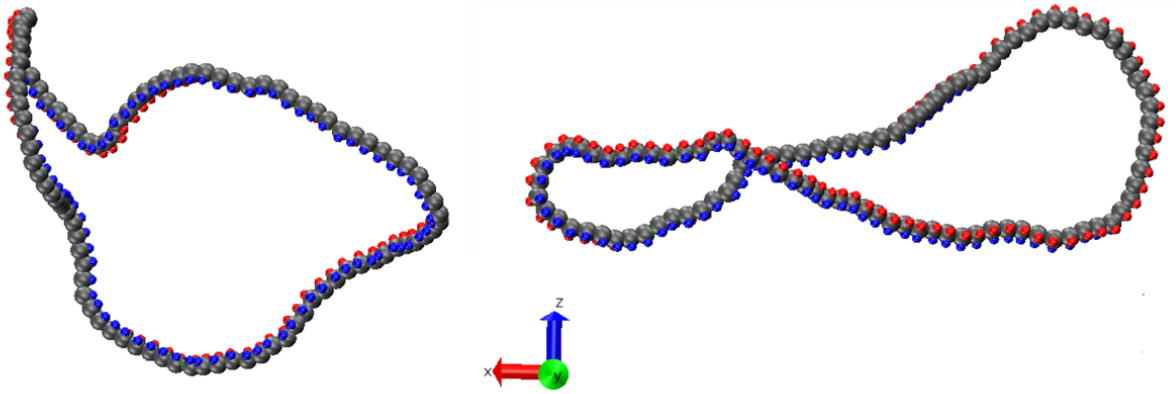

Figure 24: Snapshots of ring polymers with $N_m = 100$ and $\sigma_{\text{sc}} = 0.01$ in the flow-vorticity plane. Left: $\dot{\gamma} = 0$. Right: $\dot{\gamma} = 5 \cdot 10^{-4}(k_BT)^{0.5}m^{-0.5}a^{-1}$.

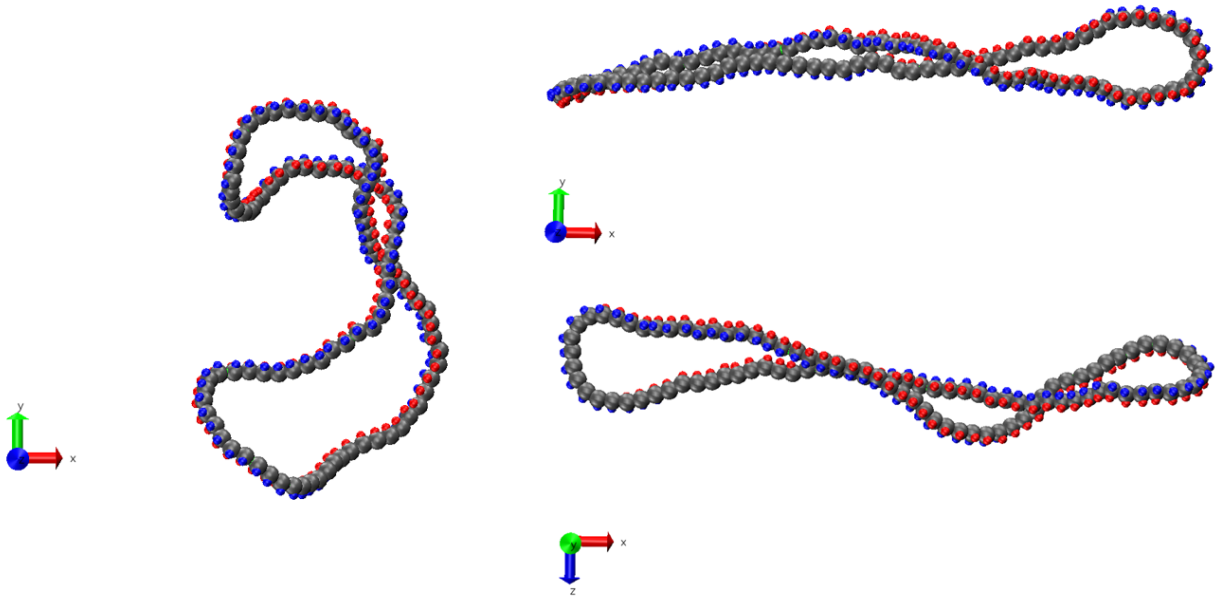

Figure 25: Snapshots of ring polymers with $N_m = 100$ and $\sigma_{\text{sc}} = 0.02$. Left: $\dot{\gamma} = 0$ in the flow-gradient plane. Top right: $\dot{\gamma} = 10^{-2}(k_BT)^{0.5}m^{-0.5}a^{-1}$ in the flow-gradient plane. Bottom right: $\dot{\gamma} = 10^{-2}(k_BT)^{0.5}m^{-0.5}a^{-1}$ in the flow-vorticity plane.

A measure of the average alignment of a polymer with the shear flow direction is the dimensionless quantity m_G which is interpreted as an orientational resistance parameter and can be calculated from the gyration tensor:

$$m_G = \tau_R\dot{\gamma}\,\frac{2\langle G_{xy}\rangle}{\langle G_{xx}\rangle - \langle G_{yy}\rangle} = \tau_R\dot{\gamma}\,\tan(2\theta). \tag{47}$$

m_G is related to the angle θ between the flow direction and the axis of largest extension, i.e.,

the eigenvector corresponding to $G_{\alpha\beta}$'s largest eigenvalue $\max(\lambda_1,\ \lambda_2,\ \lambda_3)$ [53]. To avoid the computation of any relaxation times τ_R, the orientational resistance is represented by $\tan(2\theta) = \frac{|m_G|}{\tau_R \dot{\gamma}}$ which is plotted as a function of $\dot{\gamma}$ in Fig. 26. Also, m_G can take on negative values which is why its absolute value is presented. For small shear rates θ seems to be independent of the shear rate as it fluctuates over a broad range of values without a visible trend. Certainly, these poor statistics are due to the fact that alignment has not yet occurred and the conformations differ only weakly from the ones of the stationary state so that $\langle G_{xx} \rangle \approx \langle G_{yy} \rangle \approx \langle R_g^2(0) \rangle / 3$. With and without the presence of HI, there is a change of behaviour at higher shear rates beginning at around $\dot{\gamma} \gtrsim 10^{-4} - 10^{-3} (k_B T)^{0.5} m^{-0.5} a^{-1}$. In this regime, fluctuations of θ are suppressed and the curves corresponding to the different degrees of supercoiling collapse to one monotonically decreasing line which scales as $\tan(2\theta) \sim \dot{\gamma}^{-0.33}$ with HI, respectively $\tan(2\theta) \sim \dot{\gamma}^{-0.31}$ without HI. The change in m_G's dependence of $\dot{\gamma}$ indicates that the supercoiled polymers are orientated along flow direction only for high enough shear rates. The scaling of $\tan(2\theta)$ implies that $m_G \sim \dot{\gamma}^{0.70}$ approximately for supercoiled rings as opposed to $m_G \sim \dot{\gamma}^{0.60}$ for flexible rings [29].

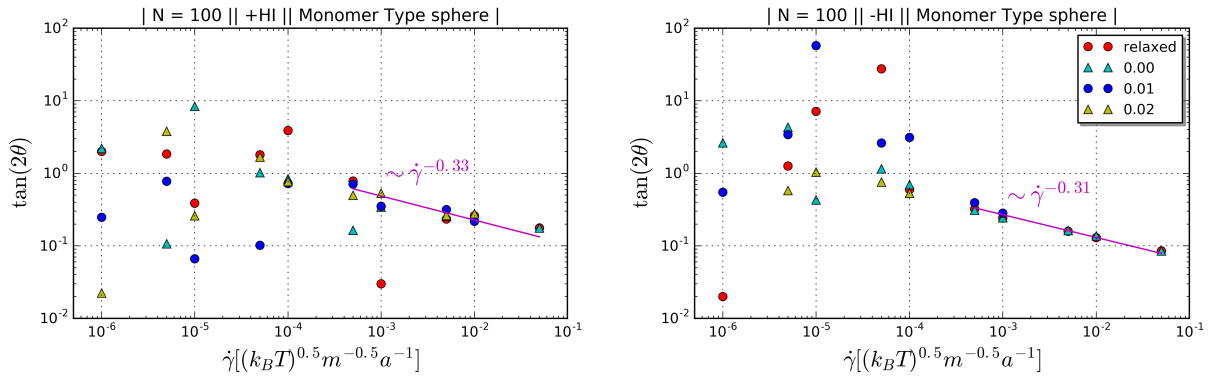

(a) (b)

Figure 26: Flow-alignment angle represented as $\tan(2\theta)$ as a function of $\dot{\gamma}$ for a supercoiled ring of length $N_m = 100$ and $\sigma_{\mathrm{sc}} = \mathrm{relaxed}, 0.00, 0.01, 0.02$ (a) with HI (+HI), (b) without HI (-HI).

6 Conclusion

In this Master Thesis ring-shaped polymers are investigated by means of MD simulations. The MPCD algorithm is used to couple the monomers to a solvent flow that enables exchange of momentum and energy with the fluid surrounding and thereby activates hydrodynamic interactions. A variation of this scheme models an alternative solvent with similar properties but without explicitly conserving momentum and therefore creates a possibility to switch off HI. By using Lees-Edwards boundary conditions a shear flow profile is generated within the MPCD fluid. First, the conformations of fully flexible ring polymers with excluded volume are investigated under shear flow. If HI is active, the ring will demonstrate the inflation behaviour under shear flow, i.e., a stiff extended circle with tumbling being suppressed, as it has been previously observed by Liebetreu and Likos [29, 30]. This behaviour results from the solvent backflow blowing up the polymer in vorticity direction which can happen exclusive to the ring topology. The occurrence of inflation also requires the presence of HI as trivial monotonic behaviour of $G_{\alpha\alpha}(\dot{\gamma})$ is measured after switching off HI. Subsequently, the polymer model is expanded by torsional and bending stiffness terms, which makes the rings take on extended and rather rigid conformations. The degree of supercoiling σ_{sc} distinguishes different supercoiled polymers by determining the characteristic amount of backbone crossings and lead to distinctive conformations. After examining the stationary state, the supercoiled ring polymers are set into a shear flow profile with shear rates varying over multiple orders of magnitude. They are observed to be much less influenced by shear than their flexible counterparts and change their shape only minimally. For higher shear rates the supercoiled polymers are elongated by the shear forces resulting in a growth factor of $\approx 2-3$ in flow direction. At the same time it shrinks in the other directions whereby the contraction is slightly more pronounced in the gradient than in the vorticity axis. The combined shrinkage is compensated by the elongation along flow so that the radius of gyration remains almost constant over all shear rates. The polymers' writhe and twist are not altered over the entire range of shear rates observed so that the overall shape, e.g., figure-eights of the $\sigma_{\mathrm{sc}} = 0.01$-ring, are maintained. In addition, HI does not play an observable role for the dynamics as all quantities measured show the exact same behaviour with and without them.

Appendix

A Software and Hardware Details

The code for the simulations is written in Fortran 90, some of the data evaluation and all plots are done in Python (NumPy and SciPy) and visualisations of polymers are created with VMD [54]. Three modules contain all subroutines, functions, and simulation parameters necessary for different parts of the program. The first module concerns the MPCD fluid, Lees-Edwards boundary conditions, coupling of embedded objects etc.; the second one contains the MD simulations of fully flexible rings described in section 3 and the corresponding data evaluation, i.e. radius of gyration etc.; the third module finally adds the dynamics of torsional and bending constraints, the calculation of writhe, and some quaternion operations necessary for the MD rotations of patchy particles. Random numbers are generated during the MPCD algorithm (axis of randomly orientated rotation matrices, placing into cells and setting starting velocities during initialisation, Poisson distributed particle numbers and effective momenta of random solvent) using the ziggurat library [55]. The computational results presented have been achieved [in part] using the Vienna Scientific Cluster (VSC).

B Calculation of Bending, Torsional, and Alignment Forces

The potentials for bending (26) and alignment (30) depend on angles formed by two segments connecting three positions, respectively, so that their gradients are the same function with different arguments. In contrast, the torsion potential (27) involves angles formed by three segments connecting four positions and has an offset in the argument of the cosine. The forces on beads and patches are derived from their gradients with respect to the position $\vec{r}_a$ where a stands for either a bead or a patch. The force on particle a resulting from the three potentials amounts to:

$$\begin{aligned}\vec{F}_a &= -\sum_c \vec{\nabla}_a k_{\text{bending}}(1-\cos(\theta^c_{\text{bending}})) - \sum_c \vec{\nabla}_a k_{\text{align}}(1-\cos(\theta^c_{\text{align}})) \\ &\quad - \sum_c \vec{\nabla}_a k_{\text{torsion}}(1-\cos(\Psi^c)\cos(\Psi_0)-\sin(\Psi^c)\sin(\Psi_0)) \\ &= k_{\text{bending}}\sum_c \vec{\nabla}_a \cos(\theta^c_{\text{bending}})) + k_{\text{align}}\sum_c \vec{\nabla}_a \cos(\theta^c_{\text{align}}) \\ &\quad + k_{\text{torsion}}\sum_c (\cos(\Psi_0)\vec{\nabla}_a\cos(\Psi^c)+\sin(\Psi_0)\vec{\nabla}_a\sin(\Psi^c)),\end{aligned} \tag{48}$$

where the index c indicates summation over all the bonds that particle a is a part of. The position of every bead particle appears in three bending terms, two torsion terms and two alignment terms, whereas the blue and red patches appear only in one torsion bond each and the green patches only in one alignment bond. The computation of $\vec{\nabla}_a \cos(\theta^c_{\text{bending}}))$, $\vec{\nabla}_a \cos(\theta^c_{\text{align}})$, and $\vec{\nabla}_a \cos(\Psi^c)$ is

performed following the calculations in [43, App. C.2, p. 491-494]. The authors omit the gradient terms of the sine appearing in (48). The missing derivations are performed in an analogue way by rewriting the sine of the torsional angle (29) formed by beads $\vec{r}_i$, $\vec{r}_{i+1}$ and patches $\vec{r}_{\mathrm{pat},i,b/r}$, $\vec{r}_{\mathrm{pat},i+1,b/r}$:

$$\sin(\Psi_{b/r}) = \frac{|\vec{r}_{i,i+1}|\vec{r}_{i,i+1} \cdot (\vec{r}_{\mathrm{pat},i,b/r} \times \vec{r}_{\mathrm{pat},i+1,b/r})}{|\vec{r}_{i,i+1} \times \vec{r}_{\mathrm{pat},i,b/r}||\vec{r}_{i,i+1} \times \vec{r}_{\mathrm{pat},i+1,b/r})|} = \frac{r_{i,i+1}}{D_1 D_2} V_{\mathrm{triple}}, \tag{49}$$

where $V_{\mathrm{triple}} = \vec{r}_{i,i+1} \cdot (\vec{r}_{\mathrm{pat},i,b/r} \times \vec{r}_{\mathrm{pat},i+1,b/r})$ and $D_1 = |\vec{r}_{i,i+1} \times \vec{r}_{\mathrm{pat},i,b/r}|$ and $D_2 = |\vec{r}_{i,i+1} \times \vec{r}_{\mathrm{pat},i+1,b/r})|$ are defined for convenience. The gradients with respect to bead position i and $i+1$ are computed by the following derivatives with $C_1 = \vec{r}_{i,i+1} \cdot \vec{r}_{\mathrm{pat},i,b/r}$ and $C_2 = \vec{r}_{i,i+1} \cdot \vec{r}_{\mathrm{pat},i+1,b/r}$:

$$\begin{aligned}\vec{\nabla}_{\vec{r}_i} \sin(\Psi_{b/r}) =& \frac{r_{i,i+1}}{D_1 D_2} \vec{r}_{\mathrm{pat},i+1,b/r} \times (\vec{r}_{\mathrm{pat},i,b/r} - \vec{r}_{i,i+1}) \\ &- \frac{V_{\mathrm{triple}}}{r_{i,i+1} D_1 D_2} \Bigg[\left(1 - \frac{r_{i,i+1}^2 (l_{\mathrm{pat}}^2 + C_1)}{D_1^2} - \frac{r_{i,i+1}^2 l_{\mathrm{pat}}^2}{D_2^2}\right) \vec{r}_{i,i+1} \\ &- \frac{r_{i,i+1}^2 (r_{i,i+1}^2 + C_1)}{D_1^2} \vec{r}_{\mathrm{pat},i,b/r} + \frac{r_{i,i+1}^2 C_2}{D_2^2} \vec{r}_{\mathrm{pat},i+1,b/r} \Bigg],\end{aligned} \tag{50}$$

$$\begin{aligned}\vec{\nabla}_{\vec{r}_{i+1}} \sin(\Psi_{b/r}) =& \frac{r_{i,i+1}}{D_1 D_2} \vec{r}_{\mathrm{pat},i,b/r} \times (\vec{r}_{\mathrm{pat},i+1,b/r} + \vec{r}_{i,i+1}) \\ &+ \frac{V_{\mathrm{triple}}}{r_{i,i+1} D_1 D_2} \Bigg[\left(1 - \frac{r_{i,i+1}^2 (l_{\mathrm{pat}}^2 + C_2)}{D_2^2} - \frac{r_{i,i+1}^2 l_{\mathrm{pat}}^2}{D_1^2}\right) \vec{r}_{i,i+1} \\ &+ \frac{r_{i,i+1}^2 (r_{i,i+1}^2 + C_2)}{D_2^2} \vec{r}_{\mathrm{pat},i+1,b/r} - \frac{r_{i,i+1}^2 C_1}{D_1^2} \vec{r}_{\mathrm{pat},i,b/r} \Bigg],\end{aligned} \tag{51}$$

while the gradients with respect to the patches $k =$ blue, red of particles i and $i+1$ are given by:

$$\vec{\nabla}_{\vec{r}_{\mathrm{pat},i,b/r}} \sin(\Psi_{b/r}) = \frac{r_{i,i+1}}{D_1 D_2} \left[\vec{r}_{\mathrm{pat},i+1,b/r} \times \vec{r}_{i,i+1} - \frac{V_{\mathrm{triple}}}{D_1^2} \left(C_1 \vec{r}_{i,i+1} + r_{i,i+1}^2 \vec{r}_{\mathrm{pat},i,b/r} \right) \right], \tag{52}$$

$$\vec{\nabla}_{\vec{r}_{\mathrm{pat},i+1,b/r}} \sin(\Psi_{b/r}) = \frac{r_{i,i+1}}{D_1 D_2} \left[- \vec{r}_{\mathrm{pat},i,b/r} \times \vec{r}_{i,i+1} + \frac{V_{\mathrm{triple}}}{D_2^2} \left(C_2 \vec{r}_{i,i+1} - r_{i,i+1}^2 \vec{r}_{\mathrm{pat},i+1,b/r} \right) \right]. \tag{53}$$

C Abstract (English)

In this Master Thesis, the dynamical and structural properties of supercoiled ring-shaped polymers under shear flow are examined with computer simulations. The behaviour of polymer models under shear have been investigated extensively [29], yet without torsion that gives the possibility of supercoiling. It was found that, while for most architectures, shearing a polymer forces it to tumble, ring-shaped polymers experience a shear-induced inflation phase for shear rates within a certain range. This phase was found to be exclusive to their shape and to require the presence of hydrodynamic interactions.

The goal of the Thesis is to extend this experiment to models with additional potential terms that consider torsional and bending stiffness of ring polymers. Such models are of interest for the simulation of supercoiled DNA and plasmids, which occur naturally in circular form [31]. It is anticipated that a similar inflation phase might exist for supercoiled ring polymers as well, but competition of supercoiling is an open question.

The polymers are simulated as ring-shaped chains and their dynamics are determined by means of molecular dynamics. A Multi-Particle Collision Dynamics (MPCD) algorithm as described in the review of Gompper et al. [14] serves as solvent background. The hydrodynamic interaction with the polymer is realized by incorporating the monomers into the collision step of the MPCD. Shear flow is imposed via Lees-Edwards boundary conditions [20] and cell-level thermostating is performed to maintain constant temperature. In order to achieve sufficiently large sample sizes, polymer sizes, and high computational speed, access to the Vienna Scientific Cluster supercomputers is provided.

The results reproduce the inflation phase for fully flexible ring polymers and demonstrate its dependency on the presence of HI by measuring the gyration tensor at varying shear rates. This behaviour is not found for supercoiled rings which appear to be more inert to the shear forces applied as a result of the torsional and bending stiffness. The simulations suggest that with increasing shear rate they are aligned along the shear flow direction while their overall shape is maintained which is observed by tracking the writhe, twist and the shape parameters of the supercoiled polymers. In addition, HI does not seem to play a role for the dynamics of supercoiled polymers.

D Abstract (German)

In dieser Masterarbeit werden mithilfe von Computersimulationen die Eigenschaften von ringförmigen Polymern mit Supercoiling hinsichtlich ihrer Dynamik und ihrer Form unter Scherung analysiert. Das Verhalten von Polymeren unter Scherung ist ausgiebig untersucht worden [29], jedoch ohne Torsion zu berücksichtigen, welche Supercoiling ermöglicht. Während die meisten Poly-

merarchitekturen unter Scherung Tumblingbewegungen durchführen, verursacht Scherung bei ringförmigen Polymeren eine Inflationsphase für gewisse Scherraten. Diese Phase tritt exklusiv für die Ringtopologie auf und benötigt hydrodynamische Wechselwirkung (HI).

Das Ziel dieser Masterarbeit besteht darin, dieses Experiment auf ein Modell zu erweitern, das zusätzlich Torsions- und Biegungssteifigkeit der Ringpolymere beachtet. Solch ein Modell ist von Interesse für die Simulation von Supercoiled DNA und Plasmiden, welche in der Natur auch ringförmig vorkommen [31]. Es wird vermutet, dass eine ähnliche Inflationsphase auch für Ringpolymere mit Supercoiling auftreten könnte. Jedoch bleibt die Frage offen, ob Supercoiling diese nicht verhindert.

Die Polymere werden als ringförmige Ketten modelliert und ihre Zeitentwicklung wird berechnet mithilfe von Molekulardynamik-Simulationen. Multi-Particle Collision Dynamics (MPCD), ein Algorithmus beschrieben von Gompper et al. [14], simuliert das Lösungsmittel. Die HI mit dem Polymer wird ermöglicht, indem die Monomere an dem MPCD-Kollisionsschritt teilnehmen. Scherfluss wird hinzugefügt durch das Verwenden von Lees-Edwards-Randbedingungen [20] und ein Thermostat auf Zelllevel hält die Temperatur konstant. Um eine ausreichend große Datenmenge, lange Polymerketten und hohes Rechnertempo zu ermöglichen, ist Zugang zum Vienna Scientific Cluster gewährt.

Die Ergebnisse bestätigen das Auftreten der Inflationsphase für flexible Ringpolymere und zeigen dessen Abhängigkeit von HI durch Messung des Gyrationtensors für variierende Scherraten. Dieses Verhalten wird nicht bei Polymeren mit Supercoiling beobachtet, die aufgrund der Torsions- und Biegungssteifigkeit träger auf die angewandten Scherkräften reagieren. Die Simulationen ergeben, dass die Ringe mit Supercoiling bei ansteigender Scherrate in Flussrichtung ausgerichtet während die allgemeine Form bewahrt wird, was durch Messung von Writhe, Twist und Formparametern der Polymere mit Supercoiling nachvollzogen wurde. Zusätzlich stellt sich heraus, dass HI keinen Einfluss auf die Dynamik von Polymeren mit Supercoiling hat.

References

[1] J. F. Marko and E. D. Siggia. Statistical mechanics of supercoiled dna. *Phys. Rev. E*, 52:2912–2938, Sep 1995.

[2] A.L.B. Pyne, A. Noy, and K.H.S. et al. Main. Base-pair resolution analysis of the effect of supercoiling on dna flexibility and major groove recognition by triplex-forming oligonucleotides. *Nat Commun*, 12(1053):5997–6001, 2021.

[3] Y. Li, K.-W. Hsiao, C. A. Brockman, D. Y. Yates, R. M. Robertson-Anderson, J. A. Kornfield, M. J. San Francisco, C. M. Schroeder, and G. B. McKenna. When ends meet: Circular dna stretches differently in elongational flows. *Macromolecules*, 48(16):5997–6001, 2015.

[4] M. Q. Tu, M. Lee, R. M. Robertson-Anderson, and C. M. Schroeder. Direct observation of ring polymer dynamics in the flow-gradient plane of shear flow. *Macromolecules*, 53:9406–9419, 2020.

[5] J. T. Padding and A. A. Louis. Hydrodynamic interactions and brownian forces in colloidal suspensions: Coarse-graining over time and length scales. *Phys. Rev. E*, 74:031402, Sep 2006.

[6] M. Liebetreu and C. N. Likos. Shear-induced stack orientation and breakup in cluster glasses of ring polymers. *ACS Applied Polymer Materials*, 2(8):3505–3517, 2020.

[7] C.-C. Huang, R. G. Winkler, G. Sutmann, and G. Gompper. Semidilute polymer solutions at equilibrium and under shear flow. *Macromolecules*, 43(23):10107–10116, 2010.

[8] L. B. Weiss, C. N. Likos, and A. Nikoubashman. Spatial demixing of ring and chain polymers in pressure-driven flow. *Macromolecules*, 52(20):7858–7869, 2019.

[9] A. Malevanets and R. Kapral. Mesoscopic model for solvent dynamics. *The Journal of Chemical Physics*, 110(17):8605–8613, 1999.

[10] M. Ripoll, K. Mussawisade, R. G. Winkler, and G. Gompper. Dynamic regimes of fluids simulated by multiparticle-collision dynamics. *Phys. Rev. E*, 72:016701, Jul 2005.

[11] A. Malevanets and J. M. Yeomans. Dynamics of short polymer chains in solution. *EPL*, 52, 2000.

[12] K Mussawisade, M. Ripoll, R. Winkler, and G. Gompper. Dynamics of polymers in a particle-based mesoscopic solvent. *The Journal of chemical physics*, 123:144905, 11 2005.

[13] M. Ripoll, R.G. Winkler, and G. Gompper. Hydrodynamic screening of star polymers in shear flow. *Eur. Phys. J. E*, 23:349–354, 2007.

[14] G. Gompper, T. Ihle, D. M. Kroll, and R. G. Winkler. *Multi-Particle Collision Dynamics: A Particle-Based Mesoscale Simulation Approach to the Hydrodynamics of Complex Fluids*, pages 1–87. Springer Berlin Heidelberg, Berlin, Heidelberg, 2009.

[15] Martin Hecht, Jens Harting, Thomas Ihle, and Hans J. Herrmann. Simulation of claylike colloids. *Phys. Rev. E*, 72:011408, Jul 2005.

[16] Hiroshi Noguchi and Gerhard Gompper. Dynamics of fluid vesicles in shear flow: Effect of membrane viscosity and thermal fluctuations. *Phys. Rev. E*, 72:011901, Jul 2005.

[17] S. Mandal and M. G. Mazza. Multiparticle collision dynamics for tensorial nematodynamics. *Phys. Rev. E*, 99:063319, Jun 2019.

[18] K.-W. Lee and M. G. Mazza. Stochastic rotation dynamics for nematic liquid crystals. *The Journal of Chemical Physics*, 142(16):164110, 2015.

[19] Andreas Zöttl. Simulation of microswimmer hydrodynamics with multiparticle collision dynamics*. *Chinese Physics B*, 29(7):074701, jun 2020.

[20] A. W. Lees and S. F. Edwards. The computer study of transport processes under extreme conditions. *Journal of Physics C: Solid State Physics*, 5(15):1921–1928, Aug 1972.

[21] M. Formanek and A. J. Moreno. Single-chain nanoparticles under homogeneous shear flow. *Macromolecules*, 52(4):1821–1831, 2019.

[22] D. Jaramillo-Cano, M. Formanek, C. N. Likos, and M. Camargo. Star block-copolymers in shear flow. *The Journal of Physical Chemistry B*, 122(14):4149–4158, 2018. PMID: 29547293.

[23] L. B. Weiss, A. Nikoubashman, and C. N. Likos. Topology-sensitive microfluidic filter for polymers of varying stiffness. *ACS Macro Letters*, 6(12):1426–1431, 2017.

[24] A. Nikoubashman and C. N. Likos. Branched polymers under shear. *Macromolecules*, 43(3):1610–1620, 2010.

[25] M. Ripoll, R. G. Winkler, and G. Gompper. Star polymers in shear flow. *Phys. Rev. Lett.*, 96:188302, May 2006.

[26] J. Ryder and J. Yeomans. Shear thinning in dilute polymer solutions. *The Journal of chemical physics*, 125:194906, 12 2006.

[27] M. Formanek and A. J. Moreno. Crowded solutions of single-chain nanoparticles under shear flow. *Soft Matter*, 17:2223–2233, 2021.

[28] D. Jaramillo-Cano, M. Camargo, C. N. Likos, and I. C. Gârlea. Dynamical properties of concentrated suspensions of block copolymer stars in shear flow. *Macromolecules*, 53(22):10015–10027, 2020. PMID: 33335338.

[29] M. Liebetreu and C. N. Likos. Hydrodynamic inflation of ring polymers under shear. *Commun Mater*, 1(4), 2020.

[30] M. Liebetreu, M. Ripoll, and C. N. Likos. Trefoil knot hydrodynamic delocalization on sheared ring polymers. *ACS Macro Letters*, 7(4):447–452, 2018.

[31] J. Smrek, J. Garamella, R. M. Robertson-Anderson, and D. Michieletto. Topological tuning of DNA mobility in entangled solutions of supercoiled plasmids. *Sci. Adv.*, 7, eabf9260, 2021.

[32] U. Frisch, B. Hasslacher, and Y. Pomeau. Lattice-gas automata for the navier-stokes equation. *Phys. Rev. Lett.*, 56:1505–1508, Apr 1986.

[33] R. G. Winkler. Flow simulations with multiparticle collision dynamics. *IAS Winter School: Hierarchical Methods for Dynamics in Complex Molecular Systems*, 2012. Forschungszentrum Juelich.

[34] C. M. Pooley and J. M. Yeomans. Kinetic theory derivation of the transport coefficients of stochastic rotation dynamics. *J Phys Chem B*, 109:6505–13, Apr 2005.

[35] I. O. Götze, H. Noguchi, and G. Gompper. Relevance of angular momentum conservation in mesoscale hydrodynamics simulations. *Phys. Rev. E*, 76:046705, Oct 2007.

[36] J. F. Ryder. *Mesoscopic Simulations of Complex Fluids*. Phd thesis, University of Oxford, 2005.

[37] E. Allahyarov and G. Gompper. Mesoscopic solvent simulations: Multiparticle-collision dynamics of three-dimensional flows. *Phys. Rev. E*, 66:036702, Sep 2002.

[38] H. Noguchi, N. Kikuchi, and G. Gompper. Particle-based mesoscale hydrodynamic techniques. *Europhysics Letters (EPL)*, 78(1):10005, mar 2007.

[39] T. Ihle and D. M. Kroll. Stochastic rotation dynamics. i. formalism, galilean invariance, and green-kubo relations. *Physical review. E, Statistical, nonlinear, and soft matter physics*, 67:066705, 07 2003.

[40] T. Ihle and D. M. Kroll. Stochastic rotation dynamics. ii. transport coefficients, numerics, and long-time tails. *Physical review. E, Statistical, nonlinear, and soft matter physics*, 67:066705, 06 2003.

[41] T. Ihle, E. Tüzel, and D. M. Kroll. Resummed green-kubo relations for a fluctuating fluid-particle model. *Physical review. E, Statistical, nonlinear, and soft matter physics*, 70(3 Pt 2):035701, 2004.

[42] N. Kikuchi, C. M. Pooley, J. F. Ryder, and J. M. Yeomans. Transport coefficients of a mesoscopic fluid dynamics model. *The Journal of Chemical Physics*, 119(12):6388–6395, 2003.

[43] M. P. Allen and D. J. Tildesley. *Computer Simulation of Liquids*, volume 2. Oxford University Press, 2017.

[44] S. Brown and G. Szamel. Structure and dynamics of ring polymers. *J. Chem. Phys.*, 108(4705), 1998.

[45] M. Doi and S.F. Edwards. *The Theory of Polymer Dynamics*. International series of monographs on physics. Clarendon Press, 1988.

[46] P. S. Lang, B. Obermayer, and E. Frey. Dynamics of a semiflexible polymer or polymer ring in shear flow. *Phys. Rev. E*, 89(022606), 2014.

[47] K.-W. Hsiao, C. M. Schroeder, and C. E. Sing. Ring polymer dynamics are governed by a coupling between architecture and hydrodynamic interactions. *Macromolecules*, 49(5):1961–1971, 2016.

[48] C. D. Young, J. R. Qian, M. Marvin, and C. E. Sing. Ring polymer dynamics and tumbling-stretch transitions in planar mixed flows. *Phys. Rev. E*, 99:062502, Jun 2019.

[49] C. A. Brackley, A. N. Morozov, and D. Marenduzzo. Models for twistable elastic polymers in Brownian dynamics, and their implementation in LAMMPS. *The Journal of Chemical Physics*, 140(13), 2014.

[50] D J. Evans and S. Murad. Singularity free algorithm for molecular dynamics simulation of rigid polyatomics. *Molecular Physics*, 34(2):327–331, 1977.

[51] K. Klenin and J. Langowski. Computation of writhe in modeling of supercoiled DNA. *Biopolymers*, 54(5), 2000.

[52] G. Călugăreanu. Sur les classes d'isotopie des noeuds tridimensionnels et leurs invariants. *Czechoslovak Mathematical Journal*, 11(4):588–625, 1961.

[53] C. Aust, M. Kröger, and S. Hess. Structure and dynamics of dilute polymer solutions under shear flow via nonequilibrium molecular dynamics. *Macromolecules*, 32(17):5660–5672, 1999.

[54] W. Humphrey, A. Dalke, and K. Schulten. VMD – Visual Molecular Dynamics. *Journal of Molecular Graphics*, 14:33–38, 1996.

[55] G. Marsaglia and W. Wan Tsang. The ziggurat method for generating random variables. *Journal of Statistical Software*, 5(8), 2000.